Design, Growth, and Characterization of Vertical Cavity Surface Emitting Lasers

Thesis by

John O'Brien

In Partial Fulfillment of the Requirements for the Degree

of Doctor of Philosophy

California Institute of Technology

Pasadena, California

1996

(Defended May 28, 1996)

Acknowledgments

I would like to thank my advisor, Professor Amnon Yariv, for his insightful guidance and for allowing me to work in the stimulating environment he has created at Caltech. It was a privilege to be a member of his research group. I also enjoyed collaborating with Professor Axel Scherer. His VCSEL knowledge and fabrication expertise and experience were invaluable.

In addition, I enjoyed working with and learning from Dr. Lars Eng and Dr. Gilad Almogy. The vertical cavity lasers wouldn't have worked without them. I also enjoyed collaborating with Yuanjian Xu, Reginald Lee, Oskar Painter, Chuan-Cheng Cheng, and Wei-Hua Xu on VCSELs and other projects. Thanks also to the graduate students with whom I shared an office for many helpful conversations: Bill Marshall, Matt McAdams, Dr. John Kitching, and especially Dr. Ali Shakouri.

I would like to thank Tom Chang and Grant Albright at EDO Corporation for generously performing the temperature measurements in Chapter 5.

Thanks also to Ali Ghaffari for his help with the MBE and other lab equipment. I also appreciated the help of Jana Mercado and Kevin Cooper.

Finally, I would like to thank Professors Gary Tuttle and Mani Mina at Iowa State University for their patience, guidance, and the opportunity to work in their labs.

Abstract

Vertical cavity surface emitting laser design, growth, and characterization is discussed. Theoretical models for gain in semiconductors as well as for the threshold gain in vertical cavity lasers is presented. The distributed Bragg mirrors used in these lasers are treated theoretically using the coupled-mode approach and with a matrix method that is generalized to include gain and loss.

The growth by molecular beam epitaxy of these structures is also discussed including steps taken to obtain precise, reproducible growth rates. Specific problems and tradeoffs encountered in the growth include greater oxygen incorporation at the lower substrate temperatures needed to ensure precise thickness control. Beryllium diffusion is also discussed and SIMS measurements are presented.

Two types of vertical cavity lasers are demonstrated. The first is a hybrid semiconductor/dielectric structure. In this design, the n-doped mirror and the optical cavity are epitaxially grown semiconductors and the top mirror is a SiO_2/Si_3N_4 distributed Bragg reflector added to the structure by reactive sputter deposition. These lasers have InGaAs quantum wells and are top-emitting near 980 nm. This design has the advantage of removing the top mirrors from the current path which reduces the series resistance. Threshold voltages of 1.8-1.9 V were obtained from 18 μm diameter lasers. In addition, the hybrid structure allows characterization before the deposition of the top mirror. Measurements of the carrier distribution and the temperature of the devices operating without the top mirrors are presented. A minimum lasers threshold current of 2.5 mA was obtained from a 6 μm diameter laser, and a maximum peak power of 1.67 mW was obtained from a 12 μm diameter laser. The lasers exhibit strongly index-guided transverse modes and are multi-moded above threshold.

Fully semiconductor vertical cavity lasers are also demonstrated. These devices are top-emitting gain-guided lasers with GaAs quantum wells. These lasers are very resistive and have high threshold voltages and currents. A peak power of 2 mW was obtained.

Contents

Chapter 1

Introduction

1.1 Introduction

The vertical cavity surface emitting laser (VCSELs) has emerged as a very important semiconductor laser structure with applications in fiber communications, optical interconnects, 2D scanning, and displays. In the last few years VCSELs have progressed from being laboratory curiosities to commercially available devices. This chapter will begin by introducing VCSELs and summarizing the early history of these lasers. Then recent advances in VCSEL technology such as the oxidation of AlAs that have led to drastically reduced threshold currents will be discussed. A section is also included describing schemes involving nonuniform doping and alloy variations that have greatly reduced the resistivity of the Bragg mirrors used in these structures leading to reduced threshold voltages. Methods and results for improving polarization and mode control will also be discussed. Finally, the chapter will conclude with a summary of the work in this thesis.

1.2 Early History of VCSELs

VCSELs have recently become available commercially. In late 1994 Motorola announced the first commercially available product containing VCSELs [1]. This is a result of major improvements in vertical cavity laser performance in the last few years. Today, VCSELs consist of an optical cavity perpendicular to the air/semiconductor interface formed between two multilayer distributed Bragg reflectors that can be designed to have reflectivities of > 99%. These lasers utilize quantum wells for gain. The first VCSELs used neither semiconductor Bragg mirrors nor quantum wells. Light emission perpendicular to the semiconductor surface was first demonstrated by Melngailis working with bulk InSb at 10 K in a magnetic field in 1965 [2]. The vertical cavity approach was suggested at the Tokyo Institute of Technology by Kenichi Iga's group in 1977. Much of the early development of these lasers was done in this group. References [3] and [4] give a summary of the efforts of this group. The first electrically pumped VCSEL was reported there in 1979 [5]. The structure was a GaInAsP/InP double heterostructure VCSEL which operated under pulsed conditions at 77 K, with a threshold current of 900 mA. The laser employed gold-zinc alloy as mirrors and as electrodes. This group achieved room temperature pulsed operation in the AlGaAs/GaAs system in 1983 [6] and began using semiconductor distributed Bragg reflectors to form the mirrors in 1985 [7]. Quantum wells were also added to surface emitting lasers in 1985, when Nomura et al. reported an optically pumped laser with a multiple quantum well active region [8]. Placing quantum wells at the peak of the standing wave optical field was suggested in 1988 by Geels et al. [9] and by Raja et al. [10]. This improved the modal gain of such structures by a factor of two. Jewell et al. reported optically pumped lasing in a single quantum well structure in 1989 [11]. This led to electrically pumped lasing with a threshold current of 1.2 mA also in 1989 [12]. This threshold current was further reduced to 0.7 mA for cw operation in 1990 by Geels and Coldren [13]. Their device was a 7 μm square index guided device with a single $In_{0.2}Ga_{0.8}As$ quantum well in the active region. By 1990, low threshold current VCSELs had been obtained, but these devices were still characterized by high threshold voltages, modest efficiencies, and low output powers.

1.3 Threshold Voltage Reduction in VCSELs

The vertical cavity lasers discussed so far which incorporated distributed Bragg reflectors were highly resistive structures. The p-doped mirror is especially resistive due to the energy barriers in the valence band between the layers in the Bragg mirror. The transport through these layers is due to thermionic emission and tunneling. The devices mentioned earlier of Geels et al. [13] had a threshold voltage of 3.5 V. These devices employed a graded alloy region between the high and low index materials of the Bragg mirrors in order to eliminate the large abrupt barriers in the valence band. This method of reducing the series resistance by placing intermediate layers in the mirror was due to an AT&T group [14] who demonstrated a reduction in the series resistance of a Bragg mirror by two orders of magnitude. Selective doping was also employed to minimize the interface barriers [15,16]. Later the interfaces were sinusoidally graded by a group at Sandia National Labs [17]. They reported a threshold voltage of 1.48 V for emission at 990 nm. Another technique was used by a group at Bellcore [18]. They made electrical contact to a p-doped region in the optical cavity and then deposited a dielectric SiO_2/Si_3N_4 top mirror. This design removes the top mirror from the current path and produced a threshold voltage of 1.7 V for a laser emitting at 850 nm. A group at Honeywell used a modification of this design which consisted of 8 pairs of semiconductor mirrors with linearly graded interfaces followed by 5 pairs of a TiO_2/SiO_2 distributed Bragg reflector [19]. This structure produced a record threshold voltage of 1.6 V (only 0.16 V above photon energy) for emission at 842 nm.

1.4 Reduction of Threshold Currents by Using Al_xO_y to Confine the Current

The structures mentioned so far used either ion implantation or an etch through the active region to define the current path. Both methods produce recombination losses at the surface of the confining regions. Recently an Al_xO_y layer formed by oxidizing AlAs has been incorporated into VCSELs to confine carriers. The oxidation procedure was developed at the University of Illinois in 1990 [20]. AlAs is oxidized at 400-425 °C with N_2 gas bubbling through water heated to 90 °C. The AlAs layer is usually sandwiched between two thin $Al_{0.3}Ga_{0.7}As$ layers which oxidize much more slowly. It has been found that the GaAs/$Al_{0.3}Ga_{0.7}As$ interface retains its low recombination velocity after the oxidation of the AlAs [21].

To fabricate VCSELs using this procedure, an AlAs layer, which can also serve as the beginning of the mirror, is placed near the active region. Large mesas are etched through the active region exposing the AlAs layer. The sample is then placed in a furnace for the wet oxidation. The oxidation proceeds inward forming an insulating layer. The current of the device is then forced through the unoxidized center. Dramatic threshold current reduction has been obtained with this technique. In 1994, a group at the University of Texas produced a laser with a room temperature cw threshold current of 225 μA [22]. This has since been improved by a group at USC to 8.7 μA for room temperature cw operation [23]. This laser was a 3 μm square device with a single InGaAs quantum well. The Al_xO_y layer also produces a small amount of index guiding that is not present in devices using ion implantation for current confinement. This reduces the optical diffraction losses that are present in small gain-guided structures and therefore means that fewer top mirror pairs are necessary in a device. A group at Sandia reported a 50% power conversion efficiency with such a laser [24]. The device had a threshold current of 350 μA and produced 1 mW of optical power with 2.04 mW of input electrical power. There is evidence, however, of a size dependent optical scattering loss due to the Al_xO_y layer [25]. This may limit the minimum laser size and therefore the minimum laser threshold current that can be obtained with this technique. Even so, these recent results are dramatic improvements over devices which use other current confinement schemes.

1.5 The Optical Mode and Polarization Characteristics of VCSELs

The transverse optical mode of a VCSEL is generally unstable and depends on the bias point and pulse conditions. There have been many studies of the optical modes of VCSELs [26-29], and several methods were employed to obtain single mode behavior. Stable single mode operation will be necessary if VCSELs are to be used in high data rate or long distance communication systems. Presently, most VCSELs operate at 850 nm or 980 nm and are used for short distance interconnect applications. For these applications, spectral purity and stability are not as important. There is even a report of the use of a multitransverse mode VCSEL being used to reduce the modal noise in a multimode fiber system [30]. The noise reduction occurs because of the decrease in the degree of coherence of the multimode laser.

The work done to obtain single transverse mode lasers has used various techniques. One technique uses a zinc diffusion and disordering to create an optical waveguide around the top mirror and part of the active region [31]. This resulted in a reported side mode suppression ratio of 36 dB. Another method uses an opening in the top metal contact that is smaller than the area being pumped to spatially filter out higher order modes [32]. This method has produced 1.5 mW in the TEM_{00} mode. A third approach uses an antiguiding cladding region around the laser to introduce larger losses for the higher order optical modes [33]. This technique produced a stable TEM_{00} mode to $12xI_{th}$ and 1.2 mW of output power in that single mode. Much work is left to be done, however, in obtaining stable single mode devices. Little is known, for example, about the reflectivity of the distributed Bragg mirrors for modes with non-planar phasefronts since standard techniques to calculate the reflectivity of these mirrors assume the optical field is a plane wave.

Another characteristic of VCSELs is an unstable optical polarization. VCSELs have two orthogonal polarizations that are spectrally degenerate or nearly degenerate, and the laser polarization alternates between these two states. The polarization state of the laser also needs to be stable for some applications. Again, several methods have been demonstrated to control the polarization state. The simplest method is to fabricate VCSELs that have anisotropic transverse cavity dimensions [34,35]. This increases the optical diffraction loss for one polarization. An orthogonal polarization suppression ratio of 14 dB has been obtained with this method [34]. Another method introduces a gain anisotropy by creating an anisotropic thermal stress [36].

1.6 Summary of This Thesis

This thesis deals with the design, growth, fabrication, and characterization of VCSELs. Chapter 2 will discuss the electronic bandstructure and gain in semiconductors. This will be used in determining the threshold conditions for VCSELs. Because optical gain occurs for only a short portion of the optical path in the cavity, the losses must be kept as small as possible. This means very highly reflective mirrors and doping limits are necessary.

Chapter 3 will discuss the distributed Bragg reflectors used to form the optical cavity. Both the coupled mode approach and a transmission matrix approach will be used to analyze these mirrors. The coupled mode theory yields many useful analytical results, but the transmission matrix approach is often necessary when more complicated structures are involved. This method can also be extended to calculate threshold gains including mirror and free carrier absorption losses.

Chapter 4 deals with the growth by molecular beam epitaxy of these structures. It will be shown that obtaining the thickness control necessary to produce these structures often results in compromising the optical quality of the material. The growth conditions necessary to reproducibly control the growth rate results in a greater incorporation of oxygen, for example, which forms a nonradiative recombination site in the AlGaAs. Wafer uniformity and Be diffusion will also be discussed.

Chapter 5 includes the results from one of the first demonstrations of the hybrid semiconductor/dielectric VCSEL structure at 980 nm. The chapter also includes measurements of the carrier distribution and the temperature of the optical cavity during electrical pumping. These measurements take advantage of the ability to characterize these devices as LEDs before the top mirror is deposited. The laser results include a threshold current of 2.5 mA for a 6 μm diameter laser, and a threshold voltage of 1.8 V for an 18 μm diameter laser.

Chapter 6 discusses the results obtained for monolithic VCSELs emitting at 850 nm. These lasers are gain guided top emitting structures. A peak output power of 2 mW was obtained from these lasers, but the threshold currents and threshold voltages obtained were high.

References

[1] J. DeTar, *Electronics News*, November 28 (1994)

[2] I. Melngailis, *Appl. Phys. Lett.*, **6**, 59 (1965)

[3] K. Iga, F. Koyama, Y. Suematsu, *IEEE J. Quant. Elect.*, **4**, 148 (1988)

[4] G. A. Evans, J. M. Hammer, eds., *Surface Emitting Semiconductor Lasers and Arrays*, Academic Press (1993)

[5] H. Soda, K. Iga, C. Kitahara, Y. Seumatsu, *Jpn. J. Appl. Phys.*, **18**, 2329 (1979)

[6] K. Iga, S. Ishikawa, S. Ohkouchi, T. Nishimura, *Appl. Phys. Lett.*, **45**, 348 (1984)

[7] A. Chailertvanitkul, K. Iga, K. Moriki, *Elect. Lett.*, **21**, 303 (1985)

[8] Y. Nomura, K. Shinozuka, K. Asakawa, M. Ishii, *Extended Abstracts of 17th Conf. on Solid State Devices and Materials*, **71**, (1985)

[9] R. Geels, R. H. Yan, J. W. Scott, S. W. Corzine, R. J. Simes, L. A. Coldren, *The Conf. on Lasers and Electro-Optics*, **WM-1**, (1988)

[10] M. Y. A. Raja, S. R. J. Brueck, M. Osinski, C. F. Schaus, J. G. McInerney, T. M. Brennan, B. E. Hammons, *Elect. Lett.*, **24**, 1140 (1988)

[11] J. L. Jewell, Y. H. Lee, R. S. Tucker, C. A. Burrus, A. Scherer, J. P. Harbison, L. T. Florez, C. J. Sandroff, *CLEO '90*, **CFF1** (1990)

[12] J. L. Jewell, A. Scherer, S. L. McCall, Y. H. Lee, S. J. Walker, J. P. Harbison, L. T. Florez, *Elect. Lett.*, **25**, 1123 (1989)

[13] R. Geels, L. A. Coldren, *12th IEEE International Semiconductor Laser Conference* (1990)

[14] K. Tai, L. Yang, Y. H. Wang, J. D. Wynn, A. Y. Cho, *Appl. Phys. Lett.*, **56**, 2496 (1990)

[15] E. F. Schubert, L. W. Tu, G.J. Zydzik, R. F. Kpof, A. Benvenuti, M. R. Pinto, *Appl. Phys. Lett.*, **60**, 466 (1992)

[16] K. Kojima, R. A. Morgan, T. Mullaly, G. D. Guth, M. W. Focht, R. E. Leibenguth, M. T. Asom, *Elect. Lett.*, **29**, 1771 (1993)

[17] K. L. Lear, S. A. Chalmers, K. P. Killeen, *Elect. Lett.*, **29**, 584 (1993)

[18] A. Scherer, J. L. Jewell, M. Walther, J. P. Harbison, L. T. Florez, *Elect. Lett.*, **28**, 1224 (1992)

[19] R. A. Morgan, M. K. Hibbs-Brenner, J. A. Lehman, E. L. Kalweit, R. A. Walterson, T. M. Marta, T. Akinwande, *Appl. Phys. Lett.*, **66**, 1157 (1995)

[20] J. M. Dallesasse, N. Holonyak Jr., A. R. Sugg, T. A. Richard, N. El-Zein, *Appl. Phys. Lett.*, **57**, 2844 (1990)

[21] J. A. Kash, B. Pezeshki, F. Agahi, N. A. Bojarczuk, *Appl. Phys. Lett.*, **67**, 2022 (1995)

[22] D. L. Huffaker, D. G. Deppe, K. Kumar, T. J. Rogers, *Appl. Phys. Lett.*, **65**, 97 (1994)

[23] G. M. Yang, M. H. MacDougal, P. D. Dapkus, *Elect. Lett.*, **31**, 886 (1995)

[24] K. L. Lear, K. D. Choquette, R. P. Schneider Jr., S. P. Kilcoyne, K. M. Geib, *Elect. Lett.*, **31**, 208 (1995)

[25] P. D. Floyd, B. J. Thibeault, L. A. Coldren, J. L. Merz, *Elect. Lett.*, **32**, 114 (1996)

[26] C. J. Chang-Hasnain, M. Orenstein, A. Von Lehmnen, L. T. Florez, J. P. Harbison, N. G. Stoffel, *Appl. Phys. Lett.*, **57**, 218 (1990)

[27] C. J. Chang-Hasnain, J. P. Harbison, G. Hasnain, A. C. VonLehmen, L. T. Florez, N. G. Stoffel, *IEEE J. Quant. Elect.*, **27**, 1402 (1991)

[28] D. L. Huffaker, D. G. Deppe, T. J. Rogers, *Appl. Phys. Lett.*, **65**, 1611 (1994)

[29] D. Vakhshoori, J. D. Wynn, G. J. Zydzik, R. E. Leibenguth, M.T. Asom, K. Kojima, R. A. Morgan, *Appl. Phys. Lett.*, **62**, 1448 (1993)

[30] K. H. Hahn, M. R. Tan, Y. M. Houng, S. Y. Wang, *Elect. Lett.*, **29**, 1482 (1993)

[31] T. G. Dziura, Y. J. Yang, R. Fernandez, S. C. Wang, *Elect. Lett.*, **29**, 1236 (1993)

[32] R. A. Morgan, G. D. Guth, M. W. Focht, M. T. Asom, K. Kojima, L. E. Rogers, S. E. Callis, *IEEE Photon. Tech. Lett.*, **4**, 374 (1993)

[33] Y. A. Wu, C. J. Chang-Hasnain, R. Nabiev, *Elect. Lett.*, **29**, 1861 (1993)

[34] K. D. Choquette, R. E. Leibenguth, *IEEE Photon. Tech. Lett.*, **6**, 40 (1994)

[35] T. Yoshikawa, H. Kosaka, K. Kurrihara, M. Kajito, Y. Sugimoto, K. Kasahara, *Appl. Phys. Lett.*, **66**, 908 (1995)

[36] T. Mukaihara, F. Koyama, K. Iga, *IEEE Photon. Tech. Lett.*, **5**, 133 (1993)

Chapter 2

Gain in Semiconductors and VCSEL Design

2.1 Introduction

This chapter will discuss gain in semiconductors and the design of vertical cavity lasers. The discussion will begin with a simple model for gain in semiconductors starting with a description of the electronic bandstructure of III-V semiconductors. This will include the effects of strain and a simple analytical model of valence band mixing in quantum wells. A general formalism will be set up, but only the k=0 case will be solved for a finite well. The valence band mixing will be illustrated with a solution for an infinite well. This will lead to a description of gain and absorption. Finally the threshold condition for a VCSEL will be discussed. VCSELs need very low loss optical cavities because the optical field only experiences gain for a short portion of the optical round trip length. This imposes strict limits on the allowable absorption and mirror losses.

2.2 Electronic Bandstructure in Quantum Wells

The semiconductors used in the work for this thesis all crystallize in the zincblende structure. In this lattice, all group III elements have four nearest neighbors that are group V atoms, in this case arsenic, and vice versa. The conduction and valence bands result from the sp^3 hybridization of the valence electrons. The valence band consists of bonding p-orbitals and the conduction band results from the antibonding s-orbitals. This section will describe the electronic bandstructure near k=0, which is the region where the optical emission takes place, based on the Luttinger-Kohn Hamiltonian and the envelope function formalism [1-3]. This method uses the Bloch theorem to write a wave function that is substituted into the one-electron Hamiltonian. For a review if the method see [4,5]. A small number of bands is selected to be included in the analysis, and the Hamiltonian is diagonalized exactly within this basis. Couplings to other bands are treated perturbatively. This method was originated by Kane in reference [6]. The Lowdin perturbation theory used in Kane's analysis will not be covered here, however. Instead, the coupling to other bands will be introduced through the Luttinger parameters. Luttinger determined the form the Hamiltonian must have from symmetry arguments including constants to be determined experimentally [7]. These constants account for the interactions that Kane treated perturbatively. To illustrate this, start with the one-electron Schrodinger equation

$$\left[\frac{p^2}{2m_o}+V(r)+\frac{\hbar}{4m_o^2c^2}(\sigma\times\nabla V)\cdot p\right]\Psi(r)=E\Psi(r) \qquad (2.1)$$

Here, the third term is the spin-orbit coupling and V(r) is the periodic crystalline potential which may also include some average potential of the electron-electron interaction. For the ternary AlGaAs, in which the Al and Ga are randomly located in the group III sites, the virtual crystal approximation is made. This approximation replaces the random potential by an average periodic potential.

Now, the wave function can be written using the Bloch theorem as

$$\Psi_{nk}(r) = N\, u_{nk}(r)\, e^{ikr} \tag{2.2}$$

where N is a normalization constant and u_{nk} is a Bloch function labelled by a band index n and a wave vector k. The Bloch functions of the semiconductor are usually not known explicitly, but it is known that at k=0 the valence band Bloch functions have the symmetry of the x,y, and z atomic p-orbitals and the conduction band Bloch function has the symmetry of an atomic s-orbital. Plugging the wave function, (2.2), into equation (2.1) gives

$$\left\{\left[\frac{p^2}{2m_o}+V(r)+\frac{\hbar}{4m_o^2c^2}(\sigma\times\nabla V)\cdot p\right]+\left[\frac{\hbar^2k^2}{2m_o}\left(p+\frac{\hbar}{4m_oc^2}\sigma\times\nabla V\right)\right]\right\}u_{nk}(r)=Eu_{nk}(r) \tag{2.3}$$

The first group of terms on the left-hand side does not depend on the wavevector k, that is

$$H(k=0)u_{n0} = E_{n0}u_{n0} \tag{2.4}$$

The u_{n0} form a complete set so the u_{nk} can be expanded in terms of them,

$$u_{nk} = \sum_m c_m(k)u_{m0} \tag{2.5}$$

Now, using equation (2.5) in equation (2.3), multiplying by u_{m0}^*, and integrating over a unit cell gives

$$\sum_{m}\left\{\left(E_{n0}-E_{nk}+\frac{\hbar^2k^2}{2m_o}\right)\delta_{mn}+\frac{\hbar k}{m_o}\langle n0|p+\frac{\hbar}{4m_oc^2}(\sigma\times\nabla V)|m0\rangle\right\}c_m(k)=0 \qquad (2.6)$$

where

$$\langle n0|p+\frac{\hbar}{4m_oc^2}(\sigma\times\nabla V)|m0\rangle=\int_{\substack{\text{unit}\\\text{cell}}}u_{n0}^{*}p+\frac{\hbar}{4m_oc^2}(\sigma\times\nabla V)u_{m0}d^3r \qquad (2.7)$$

The k=0 term in equation (2.6) is diagonal if the u_{n0} basis is chosen to be eigenfunctions of the spin-orbit interaction. This basis is

$$\begin{aligned}
\left|\frac{1}{2},\frac{1}{2}\right\rangle &= i\left|S\uparrow\right\rangle\\
\left|\frac{3}{2},\frac{3}{2}\right\rangle &= \frac{1}{\sqrt{2}}\left|(X+iY)\uparrow\right\rangle\\
\left|\frac{3}{2},\frac{1}{2}\right\rangle &= -\sqrt{\frac{2}{3}}\left|Z\uparrow\right\rangle+\frac{1}{\sqrt{6}}\left|(X+iY)\downarrow\right\rangle\\
\left|\frac{1}{2},\frac{1}{2}\right\rangle &= \frac{1}{\sqrt{3}}\left|(X+iY)\downarrow\right\rangle+\frac{1}{\sqrt{3}}\left|Z\uparrow\right\rangle\\
\left|\frac{1}{2},-\frac{1}{2}\right\rangle &= i\left|S\downarrow\right\rangle\\
\left|\frac{3}{2},-\frac{3}{2}\right\rangle &= \frac{1}{\sqrt{2}}\left|(X-iY)\downarrow\right\rangle\\
\left|\frac{3}{2},-\frac{1}{2}\right\rangle &= -\sqrt{\frac{2}{3}}\left|Z\downarrow\right\rangle-\frac{1}{\sqrt{6}}\left|(X+iY)\uparrow\right\rangle\\
\left|\frac{1}{2},-\frac{1}{2}\right\rangle &= -\frac{1}{\sqrt{3}}\left|(X-iY)\uparrow\right\rangle+\frac{1}{\sqrt{3}}\left|Z\downarrow\right\rangle
\end{aligned} \qquad (2.8)$$

In practice only a few bands are kept and diagonalized. The effects of the other bands are treated perturbatively. The band mixing is most important for the heavy hole and light hole bands. These bands are the $\left|\frac{3}{2},\pm\frac{3}{2}\right\rangle$ and the $\left|\frac{3}{2},\pm\frac{1}{2}\right\rangle$ basis functions in equation (2.8)

In a heterostructure, the function multiplying the Bloch function in the wave function is no longer a three-dimensional plane wave. In this case, the wave function in layer (A), can be written as

$$\Psi(r) = \sum_n f_n^{(A)}(r) u_{nk}^{(A)}(r) \tag{2.9}$$

where the (A) labels the material, or the layer and $f_n^{(A)}(r)$ is an envelope function. Now it is assumed that the Bloch functions in the different layers are the same. That is,

$$u_{nk}^{(Ga)}(r) = u_{nk}^{(Al)}(r) \tag{2.10}$$

so that the wave function can be written

$$\Psi(r) = \sum_n f_n^{(A)}(r) u_{nk}(r) \tag{2.11}$$

Now the envelope function $f_n^{(A)}(r)$ is

$$f_n^{(A)}(r) = \frac{1}{\sqrt{N}} e^{ik_\perp \cdot r_\perp} \chi_n^{(A)}(z) \tag{2.12}$$

which is a two-dimensional plane wave multiplied by a function which depends on the heterostructure taking z as the growth direction. Plugging this in the one-electron Hamiltonian as before gives the same result except k_z is now $-i\frac{\partial}{\partial z}$. In what follows, band mixing in the conduction band will be neglected and the interaction with the other bands will be included as an electron effective mass m^*. Also, the split-off band will not be included. The Hamiltonian for the heavy holes and the light holes is then

$$\begin{bmatrix} Hhh & b & c & 0 \\ b^* & Hlh & 0 & c \\ c^* & 0 & Hlh & -b \\ 0 & c^* & -b^* & Hhh \end{bmatrix} \tag{2.13}$$

where

$$Hhh = \frac{\hbar^2}{2m_o}\left[(\gamma_1+\gamma_2)\left(k_x^2+k_y^2\right)-(\gamma_1-2\gamma_2)\frac{\partial^2}{\partial z^2}\right]$$

$$Hlh = \frac{\hbar^2}{2m_o}\left[(\gamma_1-\gamma_2)\left(k_x^2-k_y^2\right)-(\gamma_1+2\gamma_2)\frac{\partial^2}{\partial z^2}\right]$$

$$b = \frac{\hbar^2\sqrt{3}}{m_o}\gamma_3\left(k_x-ik_y\right)\frac{\partial}{\partial z} \tag{2.14}$$

$$c = \frac{\hbar^2\sqrt{3}}{2m_o}\left[\gamma_2\left(k_x^2-k_y^2\right)-2i\gamma_3k_xk_y\right]$$

The γ's in equation (2.14) are the Luttinger parameters. From these equations it can be seen that the heavy and light holes have different effective masses in-plane than they do in the growth direction:

$$mhh_\perp = \frac{m_o}{\gamma_1+\gamma_2}$$

$$mhh_z = \frac{m_o}{\gamma_1-2\gamma_2} \tag{2.15}$$

$$mlh_\perp = \frac{m_o}{\gamma_1-\gamma_2}$$

$$mlh_z = \frac{m_o}{\gamma_1 + 2\gamma_2}$$

The k=0 eigenenergy depends on the effective mass in the z-direction and the density of states depends on the in-plane effective mass. A smaller density of states effective mass is very beneficial because it will lead to a reduced transparency carrier density. The Hamiltonian in equation (2.11) can be transformed by a unitary transformation to block diagonal form by making the axial approximation [8]. This also replaces γ_2 and γ_3 in c by their average:

$$\bar{\gamma} = \frac{1}{2}(\gamma_2 + \gamma_3) \tag{2.16}$$

This results in cylindrical symmetry about the k_z axis. The new 2x2 Hamiltonian is now

$$\begin{bmatrix} H_{hh} & R \\ R^* & H_{lh} \end{bmatrix} \tag{2.17}$$

where H_{hh} and H_{lh} are the same as in (2.12), R is given by

$$R = |c| - i|b| \tag{2.18}$$

and where c is now

$$c = \frac{\sqrt{3}\hbar^2}{2m_o}\bar{\gamma}\left(k_x - ik_y\right)^2 \tag{2.19}$$

The new basis is

$$|\mathrm{HH}\rangle=\frac{1}{\sqrt{2}}e^{i\left(\frac{3\pi}{4}-\frac{3\varphi}{2}\right)}\left|\frac{3}{2}\frac{3}{2}\right\rangle-\frac{1}{\sqrt{2}}e^{i\left(\frac{3\pi}{4}-\frac{3\varphi}{2}\right)}\left|\frac{3}{2}\frac{-3}{2}\right\rangle$$

$$|\mathrm{LH}\rangle=\frac{1}{\sqrt{2}}e^{i\left(\frac{-\pi}{4}+\frac{\varphi}{2}\right)}\left|\frac{3}{2}\frac{-1}{2}\right\rangle-\frac{1}{\sqrt{2}}e^{i\left(\frac{-\pi}{4}+\frac{\varphi}{2}\right)}\left|\frac{3}{2}\frac{1}{2}\right\rangle \tag{2.20}$$

where

$$\varphi=\tan^{-1}\left(\frac{k_y}{k_x}\right) \tag{2.21}$$

In strained layers, there is a strain Hamiltonian to consider as well [9-11]. For the 4x4 heavy hole and light hole basis this is

$$\begin{bmatrix} -\delta E_H-\frac{1}{2}\delta E_s & 0 & 0 & 0 \\ 0 & -\delta E_H+\frac{1}{2}\delta E_s & 0 & 0 \\ 0 & 0 & -\delta E_H+\frac{1}{2}\delta E_s & 0 \\ 0 & 0 & 0 & -\delta E_H-\frac{1}{2}\delta E_s \end{bmatrix} \tag{2.22}$$

where

$$\delta E_H=2a_1e_0\left(c_{11}-c_{12}\right)/c_{11}$$

$$\delta E_S=a_2e_0\left(c_{11}+2c_{12}\right)/c_{11} \tag{2.23}$$

Here, a_1 and a_2 are the hydrostastic and shear deformation potentials, and the c_{ij} are the elastic moduli. The δE_H term has the same sign for all four bands and can be interpreted as a bandgap shift. In what follows, this will be included in the external heterostructure potential where it will be divided between the conduction and the valence bands. The δE_S

terms have opposite signs for the heavy holes and the light holes and splits the bands by an amount δE_S. The 2x2 strain Hamiltonian is then

$$\begin{bmatrix} -\frac{1}{2}\delta E_S & 0 \\ 0 & \frac{1}{2}\delta E_S \end{bmatrix} \qquad (2.24).$$

Now we can calculate the energy levels in a strained quantum well. The equation is

$$\left(H_{LK} + H_{strain} + V(r)\right)\Psi = E\Psi \qquad (2.25)$$

At k=0, the heavy holes and the light holes are uncoupled and the Hamiltonian is diagonal. For an external potential due to a finite quantum well, the envelope functions satisfy

$$\begin{aligned} &\left(-\frac{\hbar^2}{2m_{hh}^*}\frac{\partial^2}{\partial z^2} + \left(V(z) - \frac{1}{2}\delta E_S - E_{hh}\right)\right)f_{hh}(z) = 0 \\ &\left(-\frac{\hbar^2}{2m_{lh}^*}\frac{\partial^2}{\partial z^2} + \left(V(z) + \frac{1}{2}\delta E_S - E_{lh}\right)\right)f_{lh}(z) = 0 \end{aligned} \qquad (2.26)$$

where the effective masses are defined in terms of the γ's as before. The boundary conditions at k=0 are that

$$f_n(z) \text{ and } \frac{1}{m^*}\frac{\partial f_n}{\partial z} \qquad (2.27)$$

be continuous across the heterostructure boundary [5]. The conduction band envelope function obeys a similar equation. The zone center subband eigenenergies are then solutions of

$$\sqrt{\left(\frac{V}{E_n}-1\right)\frac{m_w^*}{m_b^*}} = \tan\left(\frac{L_z}{2}\sqrt{\frac{2m_w^*}{\hbar^2}E_n}\right), \quad n=1,3,5,...$$

$$-\sqrt{\left(\frac{V}{E_n}-1\right)\frac{m_w^*}{m_b^*}} = \cot\left(\frac{L_z}{2}\sqrt{\frac{2m_w^*}{\hbar^2}E_n}\right), \quad n=2,4,6,... \tag{2.28}$$

where the w and b subscripts stand for well and barrier material, and L_z is the well thickness. The transition energy is then given by

$$E = E_{Gap} + E_c + E_{hh}$$

This is the sum of the bandgap of the well material modified by the strain plus the quantization energy for the conduction band and the heavy hole band. For an 80 angstrom $In_{0.2}Ga_{0.8}As$ quantum well with GaAs barriers, this energy is

$$E= 1.237 + 0.054 - 0.033$$

which corresponds to 987 nm. The data used in this calculation is in Table 2.1

	InAs	GaAs
Lattice Constant		
a_o	6.058	5.653
Luttinger Parameters		
γ_1	19.67	6.85
γ_2	8.37	2.1
γ_3	9.29	2.9
Elastic Stiffness Constants (10^{11} dyn/cm^2)		
c_{11}	8.33	11.88
c_{12}	4.53	5.38
Deformation Potentials (eV)		
a_1 (hydrostatic)	-5.9	-7.1
a_2 (shear)	-1.8	-1.7
Conduction Band Effective Mass		
m_c	0.027	0.067
Bandgap (eV)		
$In_xGa_{1-x}As$	$1.424 - 1.601x + 0.54x^2$	

Table 2.1 Values of InAs and GaAs material parameters used in the calculations. The InGaAs parameters, except for the bandgap, were obtained by a linear interpolation between the InAs and the GaAs values. Values are from references [11,12].

The heavy hole and light hole band are only uncoupled at k=0. Away from the zone center these bands mix. This affects the electronic density of states which is related to the band curvature and the matrix elements for TE and TM polarizations which depend on the valence band Bloch state. Here, valence band mixing will be treated in an infinitely deep quantum well. The infinite well approximation was made first in 1971 by Nedorezov in [13]. In this formalism the quantized subbands have to be included by hand. Here, two heavy hole bands and one light hole band will be included. It has been shown that the results from this model agree with those of more sophisticated models to within about 16% [14]. Including a second light hole subband reduces the error to about 1%. The envelope functions at k=0 are known for an infinite well. They are

$$f_n(z) = \sqrt{\frac{2}{L_z}}\sin\left(\frac{n\pi z}{L_z}\right) \tag{2.29}$$

The coupling between the first heavy hole band and the first light hole band is given by

$$\langle \mathrm{lh1}|(|c| - i|b|)|\,\mathrm{hh1}\rangle = \frac{\hbar^2\sqrt{3}}{2m_o}\bar{\gamma}k_\parallel^2 \equiv c_{12} \tag{2.30}$$

and for the second heavy hole band and the light hole band by

$$\langle \mathrm{lh1}|(|c| - i|b|)|\,\mathrm{hh2}\rangle = \frac{8\hbar^2}{\sqrt{3}m_oL_z}\gamma_3 k_\parallel \equiv c_{23} \tag{2.31}$$

There is no coupling between the first and second heavy hole bands. The subband dispersion is then given by the eigenvalues of

$$\begin{bmatrix} H_{hh1} - \frac{1}{2}\delta E_S & c_{12} & 0 \\ c_{12}^* & H_{lh1} + \frac{1}{2}\delta E_S & c_{23} \\ 0 & c_{23}^* & H_{hh2} - \frac{1}{2}\delta E_S \end{bmatrix} \tag{2.32}$$

These are the three roots of

$$(H_{hh1} - E_n)\left[(H_{lh1} - E_n)((H_{hh2} - E_n) - c_{23}^2\right] - c_{12}^2(H_{hh2} - E_n) = 0 \qquad (2.33)$$

Figure 2.1 shows a plot of these roots for an 80 angstrom $In_{0.2}Ga_{0.8}As$ infinite quantum well. The plot shows two heavy hole subbands and a light hole subband. The calculation used an effective well width to obtain the same k=0 eigenvalues as for the finite well with GaAs barriers. The smaller subband separation that occurs in the finite well will result in more strongly mixed subbands. The dispersion curves in figure 2.1 are very nonparabolic as a result of the band mixing. The data used for this calculation is in Table 2.1.

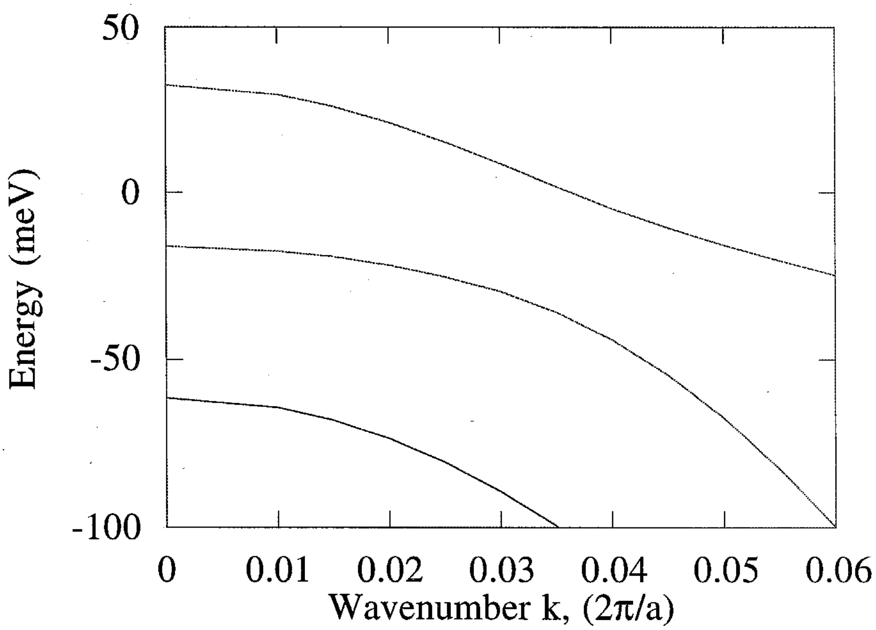

Figure 2.1. The valence band mixing for an InGaAs quantum well obtained by solving equation 2.33.

2.3 Transition Selection Rules

Having described the bandstructure and wave functions, the transition selection rules can be considered. The term in the Hamiltonian responsible for optical transitions is

$$\frac{e}{m}\mathbf{A}(r)\cdot\mathbf{p} \tag{2.34}$$

where A(r) is the vector potential. The matrix element for a transition from the conduction band to the valence band is then

$$\left\langle \Psi_v \middle| \frac{e}{m}\mathbf{A}(r)\cdot\mathbf{p} \middle| \Psi_{\mathbf{c}} \right\rangle \tag{2.35}$$

Writing the wave functions as

$$\Psi_{c,v} = f_{c,v}(r)u_{c,v}(r) \tag{2.36}$$

this becomes

$$\frac{e}{m}\int_V f_v^*(r)u_v^*(r)[\mathbf{A}(r)\cdot\mathbf{p}]f_c(r)u_c(r)d^3r \tag{2.37}$$

Letting p operate to the right, this becomes

$$\frac{e}{m}\left[\int_V u_v^*(r)u_c(r)\left(f_v^*(r)[\mathbf{A}(r)\cdot\mathbf{p}]f_c(r)\right)d^3r + \int_V \left[f_v^*(r)\mathbf{A}(r)f_c\right]\cdot u_v^*(r)\mathbf{p}u_c(r)d^3r\right] \tag{2.38}$$

For band to band transitions the first integral is zero because the term involving the envelope functions and the A·p operator is nearly constant and the Bloch functions u_v and u_c are orthogonal over a unit cell of the crystal. This integral is not zero for intersubband transitions, however, because in this case the Bloch functions are the same for the initial and final state. Now the second integral in (2.38) can be explicitly written as a sum of integrals over unit cells

$$\frac{e}{m}\sum_j\left(\left[f_v^*(r)A(r)f_c(r)\right]_{r=r_j}\int_{\substack{\text{unit}\\\text{cell}}} u_v^*(r)\hat{e}\cdot\mathbf{p}u_c(r)d^3r\right) \tag{2.39}$$

where r_j is the position of the jth unit cell, $\hat{e}$ is a unit vector in the direction of the vector potential, and as before $f_v{}^*(r)A(r)f_c(r)$ is taken as a constant in a unit cell. The integral involving the Bloch functions over the unit cell is the same in each unit cell so it can be pulled outside the sum. Since the volume of a unit cell is very small, the sum can be converted back into an integral and (2.39) becomes

$$\frac{e}{m}\langle u_v|\hat{e}\cdot\mathbf{p}|u_c\rangle\int_V f_v^*(r)A(r)f_c(r)d^3r \tag{2.40}$$

In equation (2.40) the matrix element involving the Bloch functions produces the selection rules for the optical polarization. This matrix element will be referred to as μ from now on. The gain in strained InGaAs quantum wells on GaAs substrates takes place at reasonable carrier densities from transitions between the first conduction subband and the first heavy hole subband. Near the Brillouin zone center, the heavy hole is made of $|X\rangle$ and $|Y\rangle$ Bloch states as in equation (2.8) and so couples to $\hat{x}$ or $\hat{y}$ polarizations. This is TE gain. At high carrier densities which result in transitions farther from the zone center, TM gain increases because of the heavy hole band mixing with the light hole band which contains a $|Z\rangle$ Bloch function. This band mixing can clearly be seen in figure 2.1.

The integral containing the envelope functions and the vector potential in equation (2.40) also leads to selection rules for allowed transitions between quantized subbands and k-selection. To see this, consider a field A(r) polarized in the x-y plane and use the form of the envelope functions given by equation (2.12)

$$\frac{A_o}{2}\int dz\chi_v^*(z)\chi_c(z)\int d^2re^{-ik_v\cdot r_\perp}\left(e^{ik_{opt.}\cdot r_\perp}-e^{-ik_{opt}\cdot r_\perp}\right)e^{ik_c\cdot r_\perp} \qquad (2.41)$$

The second integral is nonzero only if the k's sum to 0. That is

$$k_c - k_v = k_{opt} \qquad (2.42)$$

This is often called k-selection and results in transitions that are nearly vertical in an E-K diagram because k_{opt} is very small on a scale from 0 to the Brillouin zone edge at $2\pi/a$. There is also a selection rule from the the first integral in equation (2.41). For an infinite well this integral is nonzero only for transitions between bands with the same subband quantum number because the other subband envelope functions are orthogonal to the first. This rule allows transitions between the first subband in the conduction band and the first heavy hole and light hole valence subbands, and between the set of second subbands, and so on. In a real finite well this condition is slightly relaxed because the effective masses are different in the conduction and valence bands and because the well depth is not the same in the conduction and valence band. This destroys the orthogonality between the conduction and valence band envelope functions, but transitions that are forbidden in the infinite well model are still very weak in a finite well.

2.4 Population Inversion and Gain

Having discussed the matrix elements and the selection rules, the population inversion condition will be considered. For gain to exist in a semiconductor, the following must be true:

$$f_c(E_c)f_v(E_v) + (1 - f_v(E_v))(1 - f_c(E_c)) - 1 > 0$$

or

$$f_c(E_c) + f_v(E_v) - 1 > 0 \tag{2.43}$$

Here, $f_c(E_c)$ is the Fermi function for electrons in the conduction band evaluated at an energy E_c and $f_v(E_v)$ is the Fermi function for holes in the valence band evaluated at an energy E_v. This condition can be written in a more familiar form as

$$E_{fc} - E_{fv} > \hbar\omega \tag{2.44}$$

the separation between the two quasi-fermi levels, E_{fc} and E_{fv}, is greater than the transition energy. This condition is known as the Bernard-Duraffourg condition and was first derived in reference [15].

The gain, γ, in a semiconductor is related to the imaginary part of the susceptibility, χ_i, by

$$\gamma(\omega) = \frac{k\chi_i(\omega)}{n^2} \tag{2.45}$$

Using the expression for the complex susceptibility of a semiconductor from reference [16], this becomes

$$\gamma(\omega) = \frac{2\pi^2\mu^2}{\varepsilon_o n\hbar\lambda}\int d\omega_o\left(\frac{m_r^*}{L_z\hbar\pi}\right)\left(f_c(\omega_o)+f_v(\omega_o)=1\right)\cdot \text{lineshape function}. \qquad (2.46)$$

The arguments of the Fermi functions are only shown here schematically. These functions are to be evaluated at energies separated by the transition energy $\hbar\omega_o$. Here μ^2 is the matrix element discussed previously. The quantity

$$\left(\frac{m_r^*}{L_z\hbar\pi}\right) \qquad (2.47)$$

is the density of transition pairs per $d\omega_o$. m_r* is the reduced mass defined as

$$m_r^* = \frac{m_c^* m_v^*}{m_c^* + m_v^*}. \qquad (2.48)$$

The explicit form of the lineshape function has been left out of equation (2.46). To illustrate the gain, a lorentzian will be used here. The lineshape reduces the peak gain, and a good model for this function is necessary to produce an accurate gain value. The lorentzian used for illustration here does not fit well on the low energy side [17]. There are several models for improving the lineshape function [18-20], but they will not be used here. Figure 2.2 shows the gain calculated for an 80 angstrom $In_{0.2}Ga_{0.8}As$ quantum well for various carrier densities. The gain was calculated assuming parabolic uncoupled bands. The transition energy was obtained from the k=0 eigenenergies presented earlier, and the two different effective masses for in-plane and growth directions were accounted for.

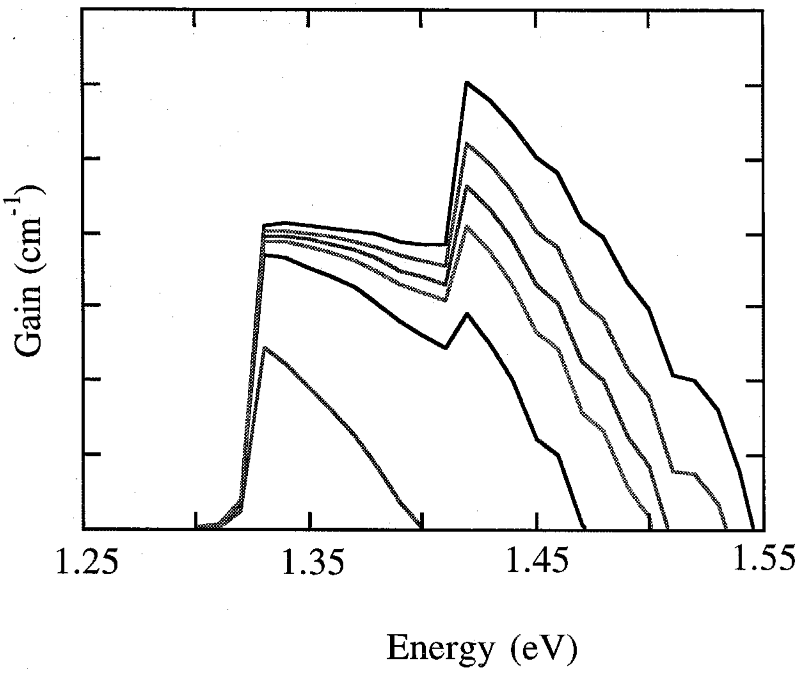

Figure 2.2. The gain calculated for an 80 angstrom $\mathrm{In}_{0.2}\mathrm{Ga}_{0.8}\mathrm{As}$ quantum well. The curves are for carrier densities of 1, 3, 4, 5, 6,and 8 x10^{12} cm^{-2} in the quantum well.

2.5 VCSEL Threshold Gain

As can be seen from figure 2.2, the peak gain increases with increasing carrier density. This increase has been found to be well described by a three parameter expression [17]

$$g = g_o \ln\left[\frac{N + N_s}{N_{tr} + N_s}\right] \tag{2.49}$$

where g_o is a constant, N_{tr} is the transparency carrier density. N_s is included so that carrier densities less than the transparency carrier density can be described. The threshold condition is that for a round trip in the optical cavity, the net gain is equal to the losses. The losses consist of the mirror losses, and scattering and free carrier absorption losses. The free carrier absorption loss depends on carrier density and any spectral dependence is neglected. To estimate the size of this term the model from reference [21] is used

$$\alpha = 3\times10^{-18}n + 7\times10^{-18}p \quad \mathrm{cm}^{-1} \tag{2.50}$$

where n and p are the electron and hole concentrations. The equation for the threshold gain is then

$$\Gamma g_{th} n L_a = \alpha L_c - \ln R \tag{2.51}$$

where Γ is the optical confinement factor, R is the mirror reflectivity, n is the number of quantum wells, L_a is the length of the active region, and L_c is the length of the cavity. The scattering and free carrier absorption losses are included in α which is assumed to be dominated by free carrier absorption. Rearranging, this equation can be written as

$$\Gamma g_{th} n \frac{L_a}{L_c} = \alpha - \frac{1}{L_c}\ln R \tag{2.52}$$

The L_a/L_c term is effectively a confinement factor in the growth direction. If the active region is made up of quantum wells, this factor can be doubled by placing the wells at the peak of the optical field standing wave. This is because the stimulated emission rate is doubled at the field peak compared to the rate for the average optical field. Equation (2.52) can be used to estimate the necessary mirror reflectivity in a VCSEL. In an edge-emittiing semiconductor laser, the L_a/L_c term is unity since the field experiences gain for the entire cavity length. The confinement factor, Γ, for a VCSEL can be close to unity, however, while it is on the order of 2% for a quantum well graded index separate confinement heterostructure (GRINSCH) laser. The left-hand sides of equation (2.52) are approximately equal for a VCSEL and a GRINSCH laser then. The VCSEL has a larger Γ which is approximately compensated for by its small value for L_a/L_c. Assuming that free carrier absorption losses dominate scattering losses, the α term is equal in a VCSEL and a GRINSCH laser with the same doping levels. To get similar threshold gains and therefore similar threshold carrier densities for a VCSEL and a GRINSCH laser, the condition is

$$\frac{1}{L_{c_{VCSEL}}} \ln R_{VCSEL} = \frac{1}{L_{c_{GRINSCH}}} \ln R_{GRINSCH} \qquad (2.53)$$

The edge emitting mirror reflectivity is approximately 0.3. For a 500 μm long GRINSCH laser and a 1 μm long VCSEL cavity, equation (2.53) gives 99.8% for the required VCSEL mirror reflectivity. This estimate is rather crude, but it is intended to illustrate that mirror reflectivities of 99% or greater are needed for low threshold currents to be obtained.

To conclude this section, the threshold current will be estimated for the structure discussed in chapter 5. Another method for calculating threshold gain will be discussed in chapter 3. The mirrors for this structure consist of 28 1/2 period AlAs/GaAs and 10 period SiO_2/Si_3N_4 distributed Bragg reflectors. Using the model to calculate mirror reflectivity discussed in the next chapter, these mirrors have a calculated reflectivity of 99.92%. The optical cavity is 1126 nm long, neglecting mirror penetration. Near the junction it is Si doped 1×10^{18} cm^{-3} on the n-side and Be doped 1×10^{18} cm^{-3} on the p-side. The three wavelength long spacer layer is Be-doped 3×10^{18} cm^{-3}. Using equation (2.50) this gives an average loss of 17 cm^{-1}. For three 80 angstrom quantum wells assuming a confinement factor of 0.8, equation (2.52) gives a threshold gain of 471.3 cm^{-1} per well. Using the values of 1800 cm^{-1} for g_o, 1.8x10^{18} cm^{-3} for N_{tr}, and -0.4x10^{18} cm^{-3} for N_s from reference [17] gives a threshold carrier density of 2.2x10^{18} cm^{-3}.

The threshold carrier density is related to the threshold current by

$$I_{th} = \frac{qN_{th}V}{\tau_{sp}} \tag{2.54}$$

where V is the active volume, q is the electronic charge, and τ_{sp} is the spontaneous lifetime. For a 6 μm diameter VCSEL, assuming a spontaneous lifetime of 1 nsec, the calculated threshold current is 0.6 mA. The lowest threshold current measured for this size laser was 2.5 mA. As mentioned in Chapter 5, however, it is estimated that about 1.8 mA of this 2.5 mA is due to surface recombination losses which were not accounted for in this model.

2.6 Conclusions

This chapter discusses gain in semiconductors and the threshold gain needed for VCSELs. The chapter started by describing the electronic bandstructure, including strain, in zincblende semiconductors through the Luttinger-Kohn Hamiltonian in the envelope function formalism. This led to a calculation of the optical transition energy and a simple infinite well model illustrating valence band mixing which is important in determining optical polarization selection rules and the transparency carrier density through the effective mass. Then a model for optical gain was presented, followed by a model to estimate the threshold gain in a VCSEL and the corresponding threshold current.

References

[1] G. Bastard, *Phys. Rev.*, **B24**, 5693 (1981)

[2] S. White, L. J. Sham, *Phys. Rev. Lett.*, **47**, 879 (1981)

[3] M. Altarelli, *Phys. Rev.*, **B28**, 842 (1983)

[4] G. Bastard, J. A. Brum, R. Ferreira, Electronic States in Semiconductor Heterostructures in *Solid State Physics*, H. Ehrenreich, D. Turnbull eds., Academic Press, San Diego (1991)

[5] G. Bastard, *Wave Mechanics Applied to Semiconductor Heterostructures,* Halsted Press, New York (1988)

[6] E. O. Kane*, J. Phys. Chem. Solids*, **1**, 249 (1957)

[7] J. M. Luttinger, *Phys. Rev.*, **102**,1030 (1956)

[8] D. A. Broido, L. J. Sham, *Phys. Rev.*, **B31**, 888 (1985)

[9] G. E. Pikus, G. L. Bir, *Sov. Phys.-Solid State*, **1**, 1502, (1960)

[10] G. L. Bir, G. E. Pikus, *Symmetry and Strain Induced Effects in Semiconductors,* Wiley, New York (1974)

[11] W. W. Chow, S. W. Koch, M. Sargent III, *Semiconductor-Laser Physics*, Springer-Verlag, New York (1994)

[12] Landolt-Bornstein, *Numerical Data and Function Relationships in Science and Technology*, 17a-b, Springer, New York (1982)

[13] S. S. Nedorezov, *Sov. Phys.-Solid State*, **12**, 1814 (1971)

[14] E. P. O'Reilly, *Semicond. Sci. Technol.*, **4**, 121 (1989)

[15] M. G. Bernard, G. Duraffourg, *Phys. Status. Solidi*, **1**, 699 (1961)

[16] A. Yariv, *Quantum Electronics*, Wiley, New York (1989)

[17] L. A. Coldren, S. W. Corzine, *Diode Lasers and Photonic Integrated Circuits*, Wiley, New York (1995)

[18] M. Yamanishi, Y. Lee, *IEEE J. Quant. Electron.*, **23**, 367 (1987)

[19] M. Asada, Intraband Relaxation Effect on Optical Spectra in *Quantum Well Lasers*, P. S. Zory Jr. ed., Academic Press, San Diego (1993)

[20] S. R. Chinn, P. Zory, A. R. Reisinger, *IEEE J. Quant. Electron.*, **24**, 2191 (1988)

[21] H. C. Casey Jr., M. B. Panish, *Heterostructure Lasers Part A: Fundamental Principles*, Academic Press, San Diego (1978)

Chapter 3

Distributed Bragg Reflectors

3.1 Introduction

This chapter will discuss distributed Bragg reflectors (DBRs). Bragg reflectors are a common way to obtain very highly reflective mirrors that have little or no absorption. These highly reflective mirrors are a necessary part of vertical cavity surface emitting lasers (VCSELs) and are also used in optical modulators and spectral filters. The optical field in a VCSEL propagates perpendicular the semiconductor surface. The mirrors of the resonator are no longer formed by cleaved crystal facets but are distributed Bragg reflectors which consist of a number of periods of alternating materials with different indices of refraction. These mirrors must have a very high reflectivity, ≥99%, as shown in Chapter 2, because the optical field no longer experiences gain for the entire pass through the cavity. If quantum wells are used in the active region, the field only experiences gain for a distance equal to the thickness of the quantum wells.

This chapter discusses two different treatments of these periodic mirrors. The first part of the chapter will discuss the coupled mode formalism. This method is important because it produces many analytical results for quantities such as reflectivity as a function of wavelength. The last half of the chapter will cover a matrix formalism for calculating the optical properties of Bragg reflectors. The matrix formalism can be used to treat more complicated structures than simple periodic mirrors. This approach is also easily generalized to include gain and loss and to calculate threshold gain for VCSEL structures.

3.2 Coupled Mode Formalism

We begin by introducing the coupled mode formalism which treats the periodic index variation as a perturbation that couples the eigenmodes of an unperturbed structure. The mathematical procedure is known as the method of variation of constants. A more general and complete treatment can be found in [1-3]. In practice, Bragg reflectors are often made from alternating layers of $Al_xGa_{1-x}As$ alloys with two different values for x. The index of refraction for various values of x is plotted versus wavelength in figure 3.1.

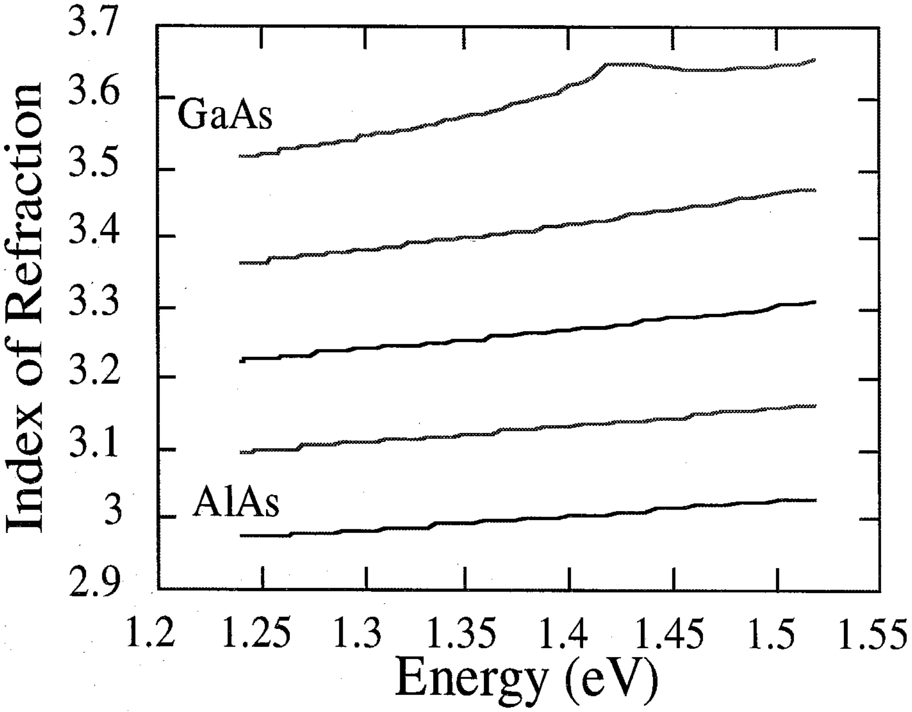

Fig. 3.1. Calculated index of refraction vs. energy for $Al_xGa_{1-x}As$ alloys. The lines are in increments of x=.25 (calculated using the model from reference [4])

For a Bragg reflector, the permitivity can be written as

$$\varepsilon(x,y,z) = \varepsilon_o(x,y) + \Delta\varepsilon(x,y,z) = \frac{1}{2}\varepsilon_o(n_1^2 + n_2^2) + \frac{1}{2}\varepsilon_o(n_2^2 - n_1^2)f(z) \qquad (3.1)$$

where n_1 and n_2 are the indices of refraction in each layer of the period and f(z) is a step function.

The normal modes for a structure that is uniform in the z-direction, $\varepsilon(x,y,z) = \varepsilon_o(x,y)$, are

$$\mathbf{E}_m(x,y)e^{i(\omega t - \beta_m z)} \qquad (3.2)$$

where the index m can be continuous or discrete. The propagation constant is given by

$$\beta^2 = \left(\frac{\omega}{c}\right)^2\left(\frac{n_1^2 + n_2^2}{2}\right) \qquad (3.3)$$

The normal modes of (3.2) satisfy

$$\left[\frac{\partial^2}{\partial x^2} + \frac{\partial^2}{\partial y^2} + \omega^2\mu\varepsilon_o(x,y) - \beta_m^2\right]\mathbf{E}_m(x,y) = 0 \qquad (3.4)$$

and also the normalization condition

$$\int \mathbf{E}_k^* \cdot \mathbf{E}_l dxdy = \frac{2\omega\mu}{|\beta_k|}\delta_{kl} \qquad (3.5)$$

which gives a power flow of 1 W in the z direction. Here, δ_{kl} is the Kronecker delta for confined modes and the Dirac delta for unbound modes. Because the normal modes form a complete set, an arbitrary field can be written as

$$\mathbf{E} = \sum_m A_m \mathbf{E}_m(x,y) e^{i(\omega t - \beta_m z)} \tag{3.6}$$

When $\varepsilon = \varepsilon_o + \Delta\varepsilon$, the modes of (3.2) are no longer eigenmodes and we write the field as

$$\mathbf{E} = \sum_m A_m(z) \mathbf{E}_m(x,y) e^{i(\omega t - \beta_m z)} \tag{3.7}$$

where we have let the coefficient A_m become z-dependent. Substituting this into the wave equation

$$\left[\frac{\partial^2}{\partial x^2} + \frac{\partial^2}{\partial y^2} + \frac{\partial^2}{\partial z^2} + \omega^2 \mu\left(\varepsilon_o(x,y) - \Delta\varepsilon(x,y,z)\right)\right]\mathbf{E} = 0 \tag{3.8}$$

and using (3.4) yields

$$-2i\sum_m \beta_m \frac{\partial A_m}{\partial z} \mathbf{E}_m(x,y) e^{-i\beta_m z} = -\omega^2 \mu \sum_l \Delta\varepsilon A_l \mathbf{E}_l(x,y) e^{-i\beta_l z} \tag{3.9}$$

In arriving at (3.9) we have also assumed

$$\left|\frac{\partial^2 A_m}{\partial z^2}\right| << \left|\beta_m \frac{\partial A_m}{\partial z}\right| \tag{3.10}$$

This is known as the parabolic approximation and is used when the perturbation is small. This means that we are assuming that the index steps in the mirror are small, or equivalently, that the reflectivity at each interface is small. To simplify equation (3.9), we multiply by $E_m^*(x,y)$, integrate over x and y, and use the orthogonality property of equation (3.5) to get

$$\frac{dA_m}{dz} = \frac{\omega|\beta_m|}{4i\beta_m}\sum_l A_l e^{i(\beta_l-\beta_m)z}\int dxdy\mathbf{E}_m^* \cdot \Delta\varepsilon(x,y,z)\mathbf{E}_l(x,y) \qquad (3.11)$$

Now we can expand $\Delta\varepsilon$ as

$$\Delta\varepsilon(x,y,z) = \sum_{j\neq 0}\varepsilon_j(x,y)e^{-i\left(\frac{2\pi j}{\Lambda}z\right)} \qquad (3.12)$$

where Λ is the Bragg reflector period. Introducing this into (3.11) gives

$$\frac{dA_m}{dz} = \frac{-i|\beta_m|}{\beta_m}\sum_l\sum_j C_{ml}^{(j)}A_l e^{-i\left(\beta_l-\beta_m-\frac{2\pi j}{\Lambda}\right)z} \qquad (3.13)$$

where

$$C_{ml}^{(j)} = \frac{\omega}{4}\int dxdy\mathbf{E}_m^*(x,y)\cdot\varepsilon_j(x,y)\mathbf{E}_l(x,y) \qquad (3.14)$$

From (3.13) we see that the modes are strongly coupled when

$$C_{ml}^{(j)} \neq 0$$

and

$$\beta_l - \beta_m - \frac{2\pi j}{\Lambda} = 0 \qquad (3.15)$$

for some integer j. This last condition is known as longtitudinal phase matching. In practice only two modes are strongly coupled. In a Bragg reflector the index grating serves to couple the forward and backward propagating modes so that the longitudinal phase matching condition becomes

$$\Delta\beta = \beta_l - \beta_m - \frac{2\pi j}{\Lambda} = 2\beta - \frac{2\pi j}{\Lambda} = 2\bar{n}\frac{\omega}{c} - \frac{2\pi j}{\Lambda} = 0 \tag{3.16}$$

or

$$\Lambda = \frac{\lambda}{2\bar{n}} \tag{3.17}$$

That is the forward and backward propagating waves are strongly coupled when the period of the grating is one-half the wavelength of the field in the material. Far away from the Bragg wavelength, other modes start to become important.

Now, to write the coupled mode equations for a Bragg reflector we use equation (3.13) for two modes with

$$\frac{|\beta_1|}{\beta_1} = 1 \qquad \frac{|\beta_2|}{\beta_2} = -1$$

and obtain

$$\frac{dA_1}{dz} = -i\kappa A_2 e^{i\Delta\beta z} \tag{3.18}$$

$$\frac{dA_2}{dz} = i\kappa^* A_1 e^{-i\Delta\beta z} \tag{3.19}$$

In (3.18) and (3.19) we have changed notation, following convention, from $C_{lm}^{(j)}$ to κ for the coupling constant. If the permitivity is a scalar function, the TE and TM modes do not couple, and equation (3.14) can be rewritten as

$$\kappa = \frac{\omega^2\mu}{2\sqrt{|\beta_1\beta_2|}}\mathbf{p}_1^* \cdot \varepsilon_m \mathbf{p}_2 \tag{3.20}$$

where p_1, and p_2 are unit polarization vectors. Using the Fourier expansion for the f(z) in equation (3.1),

$$f(z) = \sum_{m\neq 0} \frac{i(1-\cos[m\pi])}{m\pi} e^{-i\frac{2\pi m}{\Lambda}z} \tag{3.21}$$

we find

$$\kappa_{TE} = \frac{i(1-\cos[m\pi])\sqrt{2}\left(n_1^2 - n_2^2\right)}{2m\lambda\sqrt{n_1^2+n_2^2}} \tag{3.22}$$

and κ_{TM} can be found similarly. Once κ in known, the coupled-mode equations can be solved. The boundary conditions we will use are

$$\begin{aligned} A_1(0) &= 1 \\ A_2(L) &= 0 \end{aligned} \tag{3.23}$$

That is, we have a wave incident from the left on a distributed Bragg reflector of length L, and there is no incident wave from the right. The solutions then are

$$A_1(z) = \left(e^{i\frac{\Delta\beta}{2}z}\right)\frac{s\ \cosh[s(L-z)] + i\left(\frac{\Delta\beta}{2}\right)\sinh[s(L-z)]}{s\ \cosh[sL] + i\left(\frac{\Delta\beta}{2}\right)\sinh[sL]} \tag{3.24a}$$

$$A_2(z) = \left(e^{-i\frac{\Delta\beta}{2}z}\right)\frac{-i\kappa^*\sinh[s(L-z)]}{s\ \cosh[sL] + i\left(\frac{\Delta\beta}{2}\right)\sinh[sL]} \tag{3.24b}$$

Here we have defined s as

$$s^2 = \kappa^*\kappa - \left(\frac{\Delta\beta}{2}\right)^2 \tag{3.25}$$

The power in the forward and backward propagating modes in the Bragg reflector is plotted in figure 3.2. This shows that the Bragg grating serves to couple power from the foward propagating wave to the backward propagating wave.

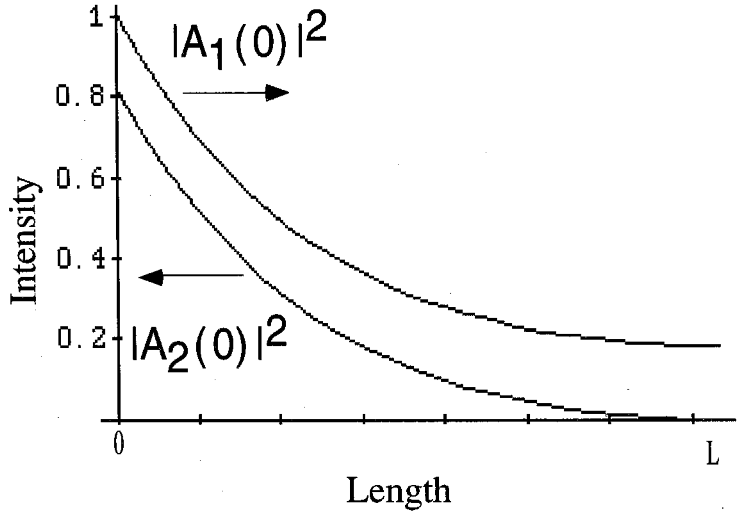

Fig. 3.2. $|A_1(z)|^2$ incident from the right and $|A_2(z)|^2$ for a distributed Bragg reflector of length L.

Having derived the coupled mode equations and solved them, we are ready to calculate the reflectivity of the distributed Bragg reflector. The reflectivity is given by

$$R = \left|\frac{A_2(0)}{A_1(0)}\right|^2 = \frac{\kappa^*\kappa\sinh^2[sL]}{s^2\cosh^2[sL] + \left(\frac{\Delta\beta}{2}\right)^2\sinh^2[sL]} \tag{3.26}$$

Figure 3.3 shows the reflectivity of a 25 period GaAs/AlAs distributed Bragg reflector calculated using equation (3.26).

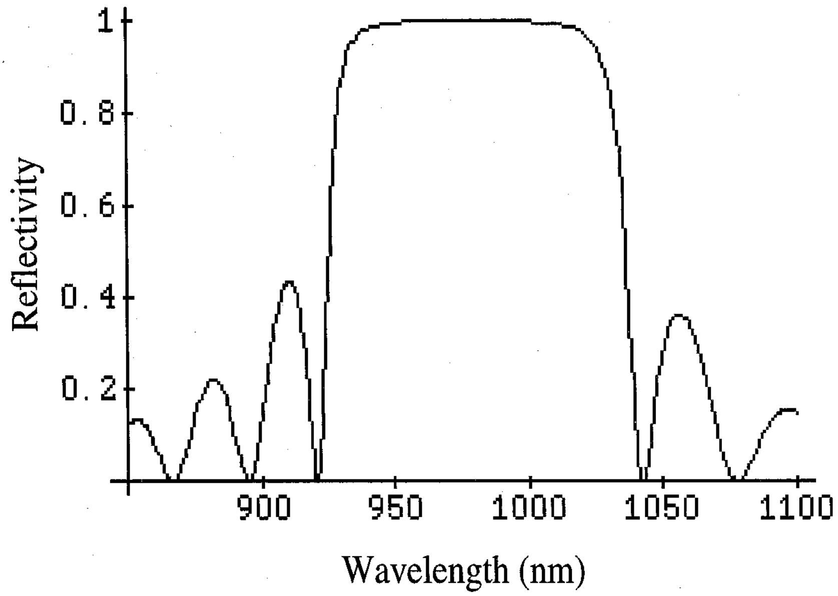

Fig.3.3. Calculated reflectivity of a 25 period GaAs/AlAs distributed Bragg reflector.

This calculation does not include the index dispersion of GaAs and AlAs over the range of 850 nm to 1100 nm. One of the biggest advantages of the coupled mode formalism is that it produces analytical results, and adding index dispersion to the model would remove that advantage. The reflectivity is maximum when $\Delta\beta = 0$, and $s^2 = \kappa^*\kappa$

$$R_{max} = \tanh^2|\kappa|L \tag{3.27}$$

The spectral width of the high reflectivity region is

$$\Delta\beta = 4|\kappa| \tag{3.28}$$

This can be understood from (3.24a,b). The propagation constant has an added term (±is), where s is given by

$$s = \sqrt{\kappa^* \kappa - \left(\frac{\Delta\beta}{2}\right)^2} \tag{3.29}$$

From (3.28) we see that the fields are evanescent for $|\Delta\beta| < 2|\kappa|$.

Next we calculate the resonance frequencies of a cavity containing distributed Bragg reflectors. The phase of the reflection coefficient is a function of frequency and is plotted in figure 3.4 for the mirror reflectivity shown in figure 3.3.

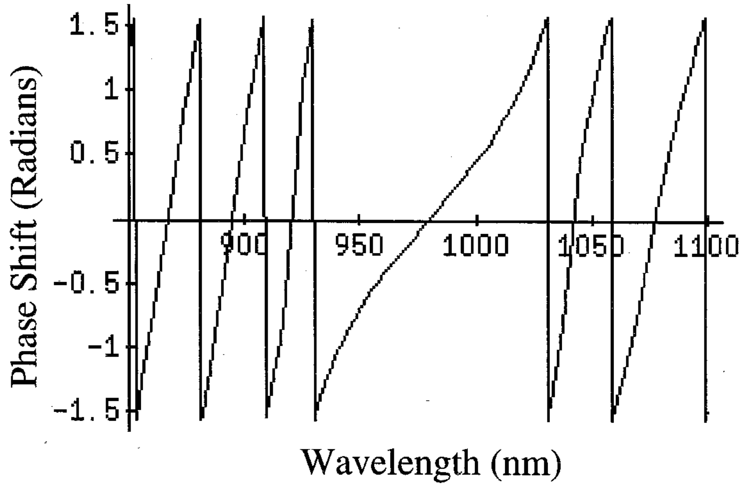

Fig. 3.4. Phase of the reflection coefficient evaluated at z=0 for the mirror of figure 3.3.

The phase shift is 0 at the Bragg frequency and changes from $-\pi/2$ to $+\pi/2$ over the high reflectivity range. The condition for a resonance frequency can be written as

$$2kl + 2\phi = 2m\pi \tag{3.30}$$

That is, the round trip phase change from propagation plus the phase changes from the two mirrors must add up to be an integral multiple of 2π. Most VCSELs have a short cavity which is on the order of an optical wavelength in length, so that only one mode overlaps with the gain spectrum of the semiconductor active region. Then approximating the phase shift of the DBR for the high reflectivity region shown in figure 3.4 by a straight line, the resonance condition can be written as

$$\frac{2\pi n l \nu_m}{c} + \frac{d\phi}{d\nu}(\nu_m - \nu_o) = m\pi \tag{3.31}$$

where ν_o is the Bragg frequency. Or, for m=1

$$\nu = \frac{\pi + \nu_o \frac{d\phi}{d\nu}}{\frac{2\pi n l}{c} + \frac{d\phi}{d\nu}} \tag{3.32}$$

This is just the resonant frequency for a Fabry-Perot cavity with linearly dispersive phase shift from the mirrors.

An approximate expression for the phase shift of the reflection coefficient, which can be used near the Bragg wavelength, in terms of the wavelength is

$$\frac{d\phi}{d\lambda} = -\frac{\pi}{\Delta\lambda_{gap}}(\lambda - \lambda_o) \tag{3.33}$$

This form is often useful in estimating the resonance wavelength of a Fabry-Perot cavity formed between two Bragg reflectors.

Because of the interest in forming very small optical cavities to modify spontaneous emission, there is another question to consider. What is the largest angle of incidence for which the Bragg reflector is still a reflector? Consider the situation shown in figure 3.5.

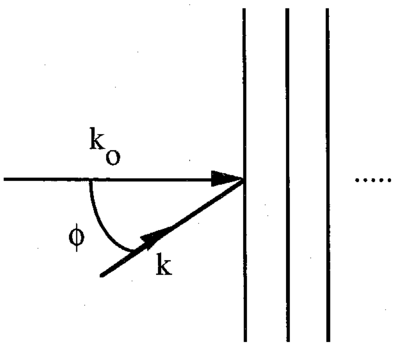

Fig. 3.5. Situation where optical is incident at an angle ϕ with respect to the normal of the Bragg reflector.

Here the incident optical field is along **k**. Then

$$k \cos \phi = k_o \tag{3.34}$$

or, solving for cosϕ and rewriting,

$$\cos \phi = \frac{\omega_o}{\omega} = \frac{\omega_o}{\omega_{\text{incident}}} \tag{3.35}$$

Now, for the incident frequency equal to the center Bragg frequency, and ω_o equal to the low frequency edge of the Bragg reflector,

$$\cos \phi = \frac{\omega_{\text{Bragg}} - \frac{\Delta\omega}{2}}{\omega_{\text{Bragg}}} = 1 - \frac{\Delta\omega}{2\omega_{\text{Bragg}}} \tag{3.36}$$

Now, using the results from above for the frequency bandgap, (3.28), we can express the largest angle from the surface normal at which the Bragg reflector appreciably reflects as

$$\varphi = \cos^{-1}\left(1 - \frac{2c|\kappa|}{\bar{n}\omega_{\mathrm{Bragg}}}\right) \tag{3.37}$$

or rewriting κ, the angle ϕ is the solution of

$$\cos\varphi = 1 - \frac{2\omega}{\pi\cos\varphi}\left(\frac{\left|n_1^2 - n_2^2\right|}{n_1^2 + n_2^2}\right) \tag{3.38}$$

3.3 Matrix Method for Calculating Reflectivity

Another method for calculating the optical properties of Bragg reflectors is the transmission matrix method. This method is more flexible and is used for large index steps between the layers, for more complicated index profiles, or for nonperiodic structures. The method also easily generalizes to include gain and loss in the layers. Later, this method will be used to calculate the threshold gain of VCSEL structures. To illustrate this method, we will consider a simple Bragg reflector with a wave propagating in the plus and minus z directions. The index of refraction is periodic and is given by

$$\begin{array}{ll} n = n_1 & x < 0 \\ n = n_2 & 0 < x < d_1 \\ n = n_1 & d_1 < x < d_2 \ \ldots\ldots \end{array} \tag{3.39}$$

If the medium is homogeneous in the x-y plane, the electric field can be written as the sum of a forward and a backward propagating wave. For a TE wave, this is

$$\mathbf{E}(x,y,z) = \left(Re^{-ik_z z} + Le^{+ik_z z}\right)e^{i(\omega t - \beta x)}\hat{\mathbf{y}}$$

$$\mathbf{E}(x,y,z) = (A(z) + B(z))e^{i(\omega t - \beta x)}\hat{\mathbf{y}} \tag{3.40}$$

From now on we will drop the vector notation and the x and t dependence. Now, for the structure illustrated in figure 3.6, we define:

$$\begin{aligned} A_1 &= A(0^-) \\ B_1 &= B(0^-) \\ A'_2 &= A(0^+) \\ B'_2 &= B(0^+) \\ A_2 &= A(d^-) \\ B_2 &= B(d^-) \end{aligned} \tag{3.41}$$

and so on.

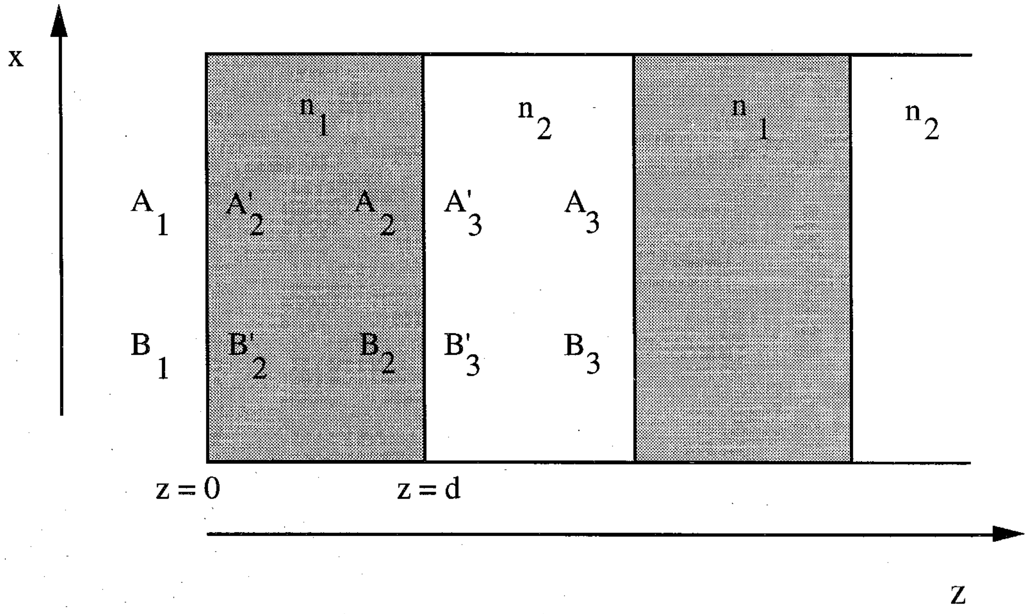

Fig. 3.6. A section of the dielectric layers in a Bragg reflector.

The coefficients on each side of an interface are related to each other by the continuity of E_y and H_x. The continuity of H_x can be written as

$$\frac{i}{\omega\mu}\frac{\partial E_y}{\partial z} \text{ is continuous} \tag{3.42}$$

This is just Maxwell's curl equation for **E**. So we have for the equations at the interface at z=0,

$$\begin{aligned} A(0^-) + B(0^-) &= A(0^+) + B(0^+) \\ -ik_{z1}A(0^-) + ik_{z1}B(0^-) &= -ik_{z2}A(0^+) + ik_{z2}B(0^+) \end{aligned} \tag{3.43}$$

or in matrix form

$$\begin{pmatrix} 1 & 1 \\ -n_1 & n_1 \end{pmatrix}\begin{pmatrix} A(0^-) \\ B(0^-) \end{pmatrix} = \begin{pmatrix} 1 & 1 \\ -n_2 & n_2 \end{pmatrix}\begin{pmatrix} A(0^+) \\ B(0^+) \end{pmatrix} \tag{3.44}$$

This equation can be solved for the components on the right-hand side of the interface.

$$\begin{pmatrix} A(0^-) \\ B(0^-) \end{pmatrix} = \begin{pmatrix} \frac{1}{2}\left(1 + \frac{n_2}{n_1}\right) & \frac{1}{2}\left(1 - \frac{n_2}{n_1}\right) \\ \frac{1}{2}\left(1 - \frac{n_2}{n_1}\right) & \frac{1}{2}\left(1 + \frac{n_2}{n_1}\right) \end{pmatrix}\begin{pmatrix} A(0^+) \\ B(0^+) \end{pmatrix} \tag{3.45}$$

This matrix that relates the coefficients on both sides of the interface is called the transmission matrix. Next, we need to connect the coefficients at one side of the layer with the coefficients at the other side of the same layer. This is just a propagation. The relation between the coefficients at z=0, and z=d is

$$\begin{pmatrix} A(0^+) \\ B(0^+ \end{pmatrix} = \begin{pmatrix} e^{ik_{z2}d} & 0 \\ 0 & e^{-ik_{z2}d} \end{pmatrix} \begin{pmatrix} A(d^-) \\ B(d^- \end{pmatrix} \tag{3.46}$$

So now we have a propagation matrix

$$P_2 = \begin{pmatrix} e^{ik_{z2}d} & 0 \\ 0 & e^{-ik_{z2}d} \end{pmatrix} \tag{3.47}$$

The other interfaces and propagations can be handled in the same way. The coefficients on the right-hand side can be related to the coefficients on the left-hand side by multiplying these matrices together,

$$\begin{pmatrix} A(0^-) \\ B(0^-) \end{pmatrix} = D_{12}P_2D_{23}P_3 \ldots D_{n-1\ n} \begin{pmatrix} A(L) \\ B(L) \end{pmatrix} \tag{3.48}$$

where the D_{ij}'s are the transmission matrices. Writing this more simply,

$$\begin{pmatrix} A(0^-) \\ B(0^-) \end{pmatrix} = \begin{pmatrix} M_{11} & M_{12} \\ M_{21} & M_{22} \end{pmatrix} \begin{pmatrix} A(L) \\ B(L) \end{pmatrix} \tag{3.49}$$

where we have just renamed the product of the transmission and propagation matrices. Now, the reflection coefficient, for reflection from the left interface of the Bragg reflector is

$$R = |r|^2 = \left|\frac{M_{21}}{M_{11}}\right|^2 \tag{3.50}$$

Figure 3.7 shows the reflectivity vs. wavelength for the same structure that was used in figure 3.3 but now using the matrix method. Also included in this calculation is the index dispersion of the GaAs and the AlGaAs shown in figure 2.1, which was taken into account by the model of reference [4]. The plot was obtained by calculating the needed indices of refraction at a given wavelength, and then calculating the reflection coefficient at that wavelength. This was repeated at each wavelength as the wavelength was increased in small increments to span the region of the plot. The phase of the reflection coefficient can also be obtained.

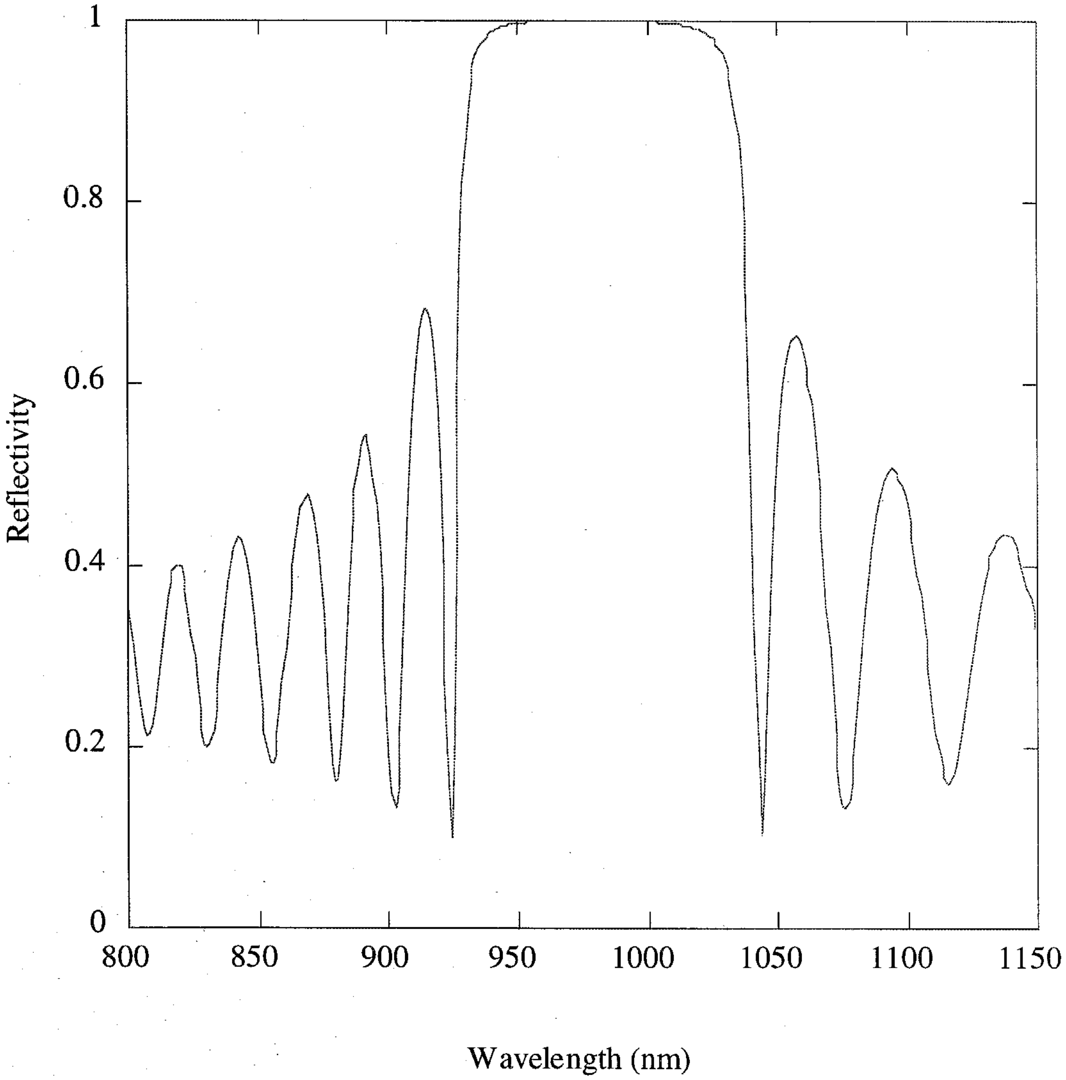

Fig. 3.7. Reflectivity vs. wavelength for a 25 period GaAs/AlAs Bragg reflector.

Bragg reflectors can also be used to form a resonant cavity. Figure 3.8 shows the reflectivity for a one-wavelength long optical cavity between two 15 period AlAs/GaAs Bragg reflectors calculated using the matrix method.

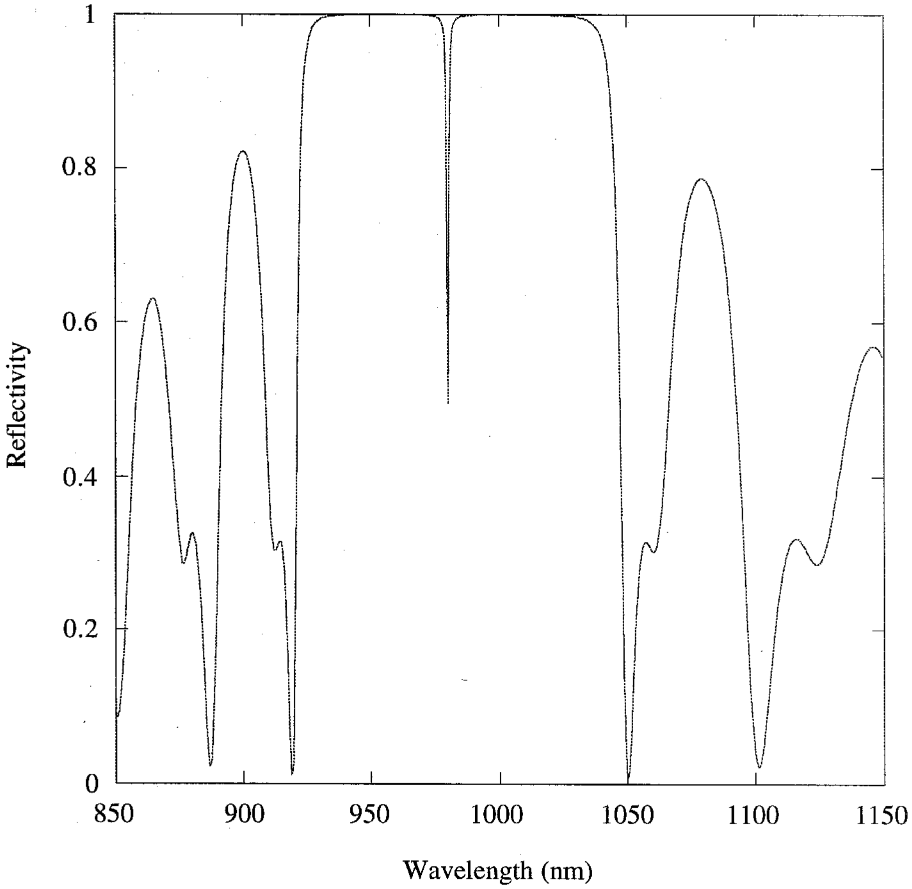

Fig. 3.8. Reflectivity of a Fabry-Perot resonant cavity formed between two Bragg reflectors.

Figure 3.8 contains a dip in the reflectivity in the middle of the gap of the Bragg reflectors. This is the resonant mode of the Fabry-Perot cavity. It can be thought of as a mode allowed by the defect, the space between the mirrors, in the overall periodicity. The plot does not show the mode as having a zero of the reflectivity because the step size in the calculation was not small enough. The matrix method also can be used to calculate the optical field profile in the structure. Figure 3.9 illustrates the profile of the optical field for the resonator with 25 periods of AlAs/GaAs on each side of the cavity.

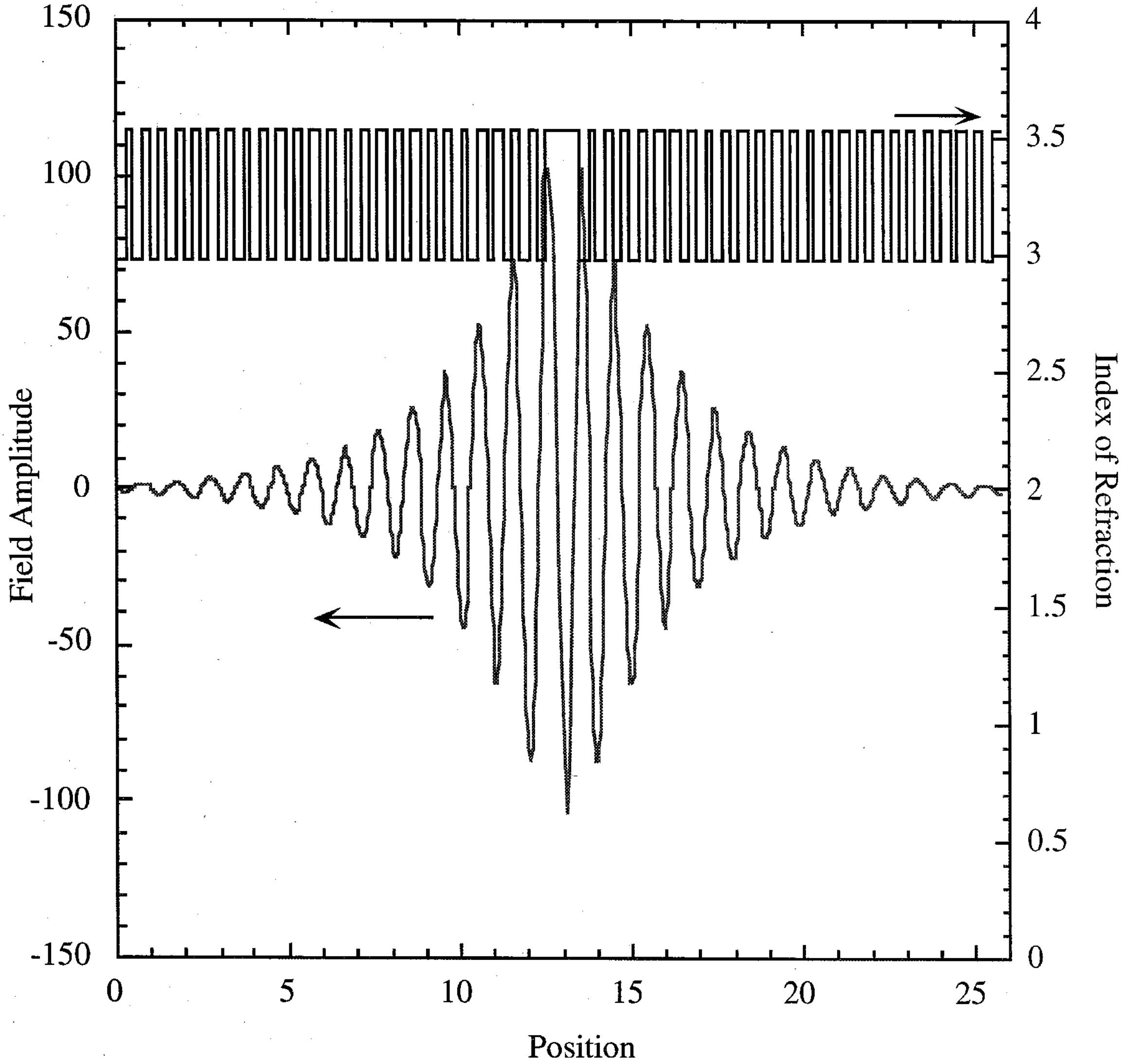

Fig. 3.9. The optical field in a VCSEL resonator.

The matrix method can be applied to an arbitrary set of layers. This is useful in VCSEL modeling because often there are layers with intermediate bandgaps and indices of refraction placed between the two primary layers in each period. These layers are included to reduce the series resistance of the stack, as discussed in Chapter 1.

The method is also easy to generalize to include gain and loss [5]. That is, the propagation constant that appears in the transmission and propagation matrices can be complex. We will illustrate this with a treatment of a simple Fabry-Perot laser. The structure is shown below in figure 3.10.

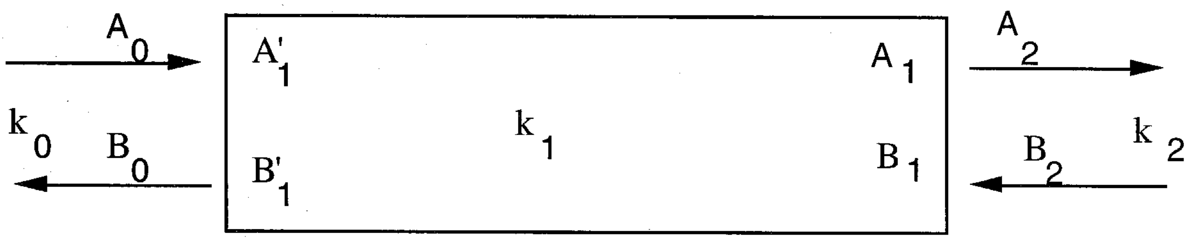

Fig. 3.10. A simple Fabry-Perot laser.

Now let each k be complex,

$$k_i = \frac{\omega}{c}n_i = \frac{\omega}{c}(\eta_i + i\kappa_i) \tag{3.51}$$

κ is positive for lossy material and negative if there is gain. The threshold gain condition is obtained by setting the waves incident on the laser structure to 0. That is A_0 and B_2 are zero. Setting up the matrix equations we obtain,

$$\begin{pmatrix} 0 \\ B_0 \end{pmatrix} = \begin{pmatrix} \frac{1}{2}\left(1 + \frac{k_1}{k_0}\right) & \frac{1}{2}\left(1 - \frac{k_1}{k_0}\right) \\ \frac{1}{2}\left(1 - \frac{k_1}{k_0}\right) & \frac{1}{2}\left(1 + \frac{k_1}{k_0}\right) \end{pmatrix} \begin{pmatrix} e^{-ik_1L} & 0 \\ 0 & e^{ik_1L} \end{pmatrix} \begin{pmatrix} \frac{1}{2}\left(1 + \frac{k_2}{k_1}\right) & \frac{1}{2}\left(1 - \frac{k_2}{k_1}\right) \\ \frac{1}{2}\left(1 - \frac{k_2}{k_1}\right) & \frac{1}{2}\left(1 + \frac{k_2}{k_1}\right) \end{pmatrix} \begin{pmatrix} A_2 \\ 0 \end{pmatrix} \tag{3.52}$$

Next, we multiply the matrices and set the (11) term in the matrix equal to zero:

$$(k_0 + k_1)(k_1 + k_2)e^{-ik_1L} + (k_0 - k_1)(k_1 - k_2)e^{ik_1L} = 0 \qquad (3.53)$$

To continue, we use $\eta_0 = \eta_2 = 1$, $\kappa_0 = \kappa_2 = 0$, $\eta_1 = 3.6$, and $|\kappa_1| << \eta_1$. After some algebra we obtain

$$\omega = \frac{m\pi c}{nL} \qquad (3.54)$$

$$\kappa = \frac{c \ln R}{\omega 2L} \qquad (3.55)$$

or, written in a more familiar form for the resonant frequency, ν_m, and the threshold gain, γ, of a Fabry-Perot laser

$$\nu_m = \frac{mc}{2nL} \qquad (3.56)$$

$$\gamma = \frac{1}{L} \ln R \qquad (3.57)$$

If a model for free carrier absorption is included in the calculation, the threshold gain will account for absorption losses also. Using the free carrier absorption model from Chapter 2, equation (2.50), this method gives a threshold gain of 1004 cm^{-1} for the structure considered in section 2.5. This gain is a modal gain in the sense that it includes the L_a/L_c factor of equation (2.52). This value corresponds to a gain of 418 cm^{-1} per well assuming the transverse confinement factor is 0.8. This value agrees pretty well with the value of 471.3 cm^{-1} obtained in Chapter 2 from a much more simplistic model.

3.4 Conclusions

Two methods for calculating properties of distributed Bragg reflectors have been described. The coupled mode formalism is a useful tool in making calculations for Bragg reflectors because it gives many analytical results. For more complicated structures like a Bragg reflector with more than two layers in a period or for materials where the index dispersion is important, a matrix method is used to calculate the reflectivity numerically. The matrix method can also be used to calculate the threshold gain of a VCSEL including free carrier absorption and mirror losses.

References

[1] P. Yeh, *Optical Waves in Layered Media*, Wiley, New York (1988)

[2]] A. Yariv, P. Yeh, *Optical Waves in Crystals*, Wiley, New York (1984)

[3] L. A. Coldren, S. W. Corzine, *Diode Lasers and Photonic Integrated Circuits*, Wiley, New York (1995)

[4] M. A. Afromowitz, *Solid State Communications*, **15**, 59, 1974

[5] K. J. Ebeling, L. A. Coldren, *J. Appl. Phys.*, **54**, 2962 (1983)

Chapter 4 Molecular Beam Epitaxy and Its Use in the Growth of Vertical Cavity Surface Emitting Lasers

4.1 Introduction

All the semiconductor structures discussed in this thesis were grown by molecular beam epitaxy (MBE) which allows the deposition of material with atomic layer precision. This chapter will discuss the system used in the lab. Then the fundamentals of the growth of GaAs, $Al_xGa_{1-x}As$, and $In_xGa_{1-x}As$ semiconductors by MBE will be described. Following this is a section describing growth rate calibrations and steps taken to ensure growth rate reproducibility. This is followed by a short discussion of wafer uniformity. These issues are particularly important for the growth of vertical cavity lasers. The chapter will conclude with a discussion of specific problems encountered in the growth such as oxygen contamination and dopant diffusion. The secondary ion mass spectroscopy (SIMS) measurements shown in this chapter were made by Charles Evans and Associates, and the SEM and TEM photographs were taken by Professor Axel Scherer. A much more complete treatment of MBE growth can be found in the reviews [1,2].

4.2 The MBE System

The MBE system used was a Riber 2300 three chamber system with 2" wafer capability. Two of the chambers are used as load locks for sample introduction. A cross section of the growth chamber is shown in figure 4.1. The vacuum in the growth chamber is maintained for months at a time. The chamber is only exposed to the atmosphere when source material needs to be refilled or a repair is necessary. The system was pumped by ion pumps for the growth of the material discussed in this thesis. Recently, a cryo-pump was added to the growth chamber. During growth, cryopanels in the chamber are filled with liquid nitrogen to increase the pumping speeds. Pressures can reach 10^{-10} Torr when the cryopanels are cold. The growth chamber contains two aluminum cells, a gallium cell, an indium cell, a silicon cell, a beryllium cell, and an arsenic cell. The arsenic cell is a 200 cc Perkin-Elmer arsenic cracking cell which can produce As_4 or As_2. As_2 was used in the work for this thesis. The gallium cell was recently changed to an EPI dual filament effusion cell. The change was made in an effort to reduce the density of oval defects in the material. Oval defects have been attributed to "gallium spitting" or flux noise of the gallium source which may be caused by gallium condensing on the tip of the PBN crucible [3]. The density of oval defects has been shown to be reduced with the use of a dual filament cell which keeps the tip of the crucible hot to prevent gallium condensation [3]. The growth chamber has two rows of ports for effusion cells. In the MBE in our lab, silicon, arsenic, and an aluminum cell are in the top row while the bottom row contains gallium, indium, beryllium, and the other aluminum cell. It was found that growth rate reproducibility improved when the group III elements were all located in the bottom row of sources. In addition, a 1" spacer is located between the cell and the growth chamber for the gallium and the two aluminum cells. This spacer reduces the flux transients which will be discussed in section 4.4.

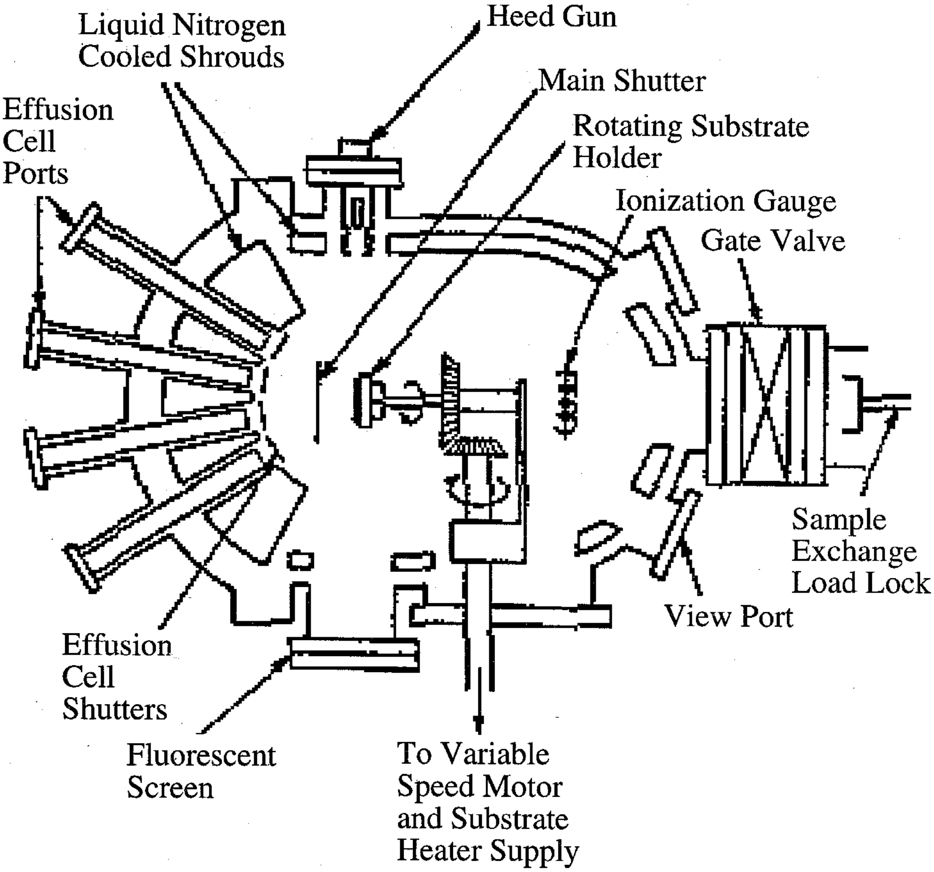

Figure 4.1. A schematic cross section of the MBE growth chamber.

The wafers used were (100) n+ wafers which were cleaned before introduction into the MBE. The cleaning consisted of a 5 minute rinse in hot, ~ 60 °C, sulfuric acid to remove organic contaminants, followed by a 1 minute rinse in sulfuric acid at room temperature. The sample was then etched for 5 minutes in a 4:1:1 mixture of sulfuric acid, water, and hydrogen peroxide. This step etches approximately 50 microns off the wafer. This is followed by another 1 minute rinse in sulfuric acid, a 2 minute rinse in DI water, and a 1 minute rinse in HCl. The HCl removes oxide and organic materials. The last step in the cleaning procedure is a 2 minute rinse in DI water. The sample was then dried and In-soldered to a Mo block at about 220 °C before being loaded into the MBE.

4.3 Growth of GaAs, InGaAs, and AlGaAs

Epitaxy is from the Greek words επι and ταξι meaning on and arrangement [4]. Growth occurs through the evaporation of group III elements and the sublimation of As_4 and its subsequent cracking into As_2 in an ultra-high vacuum environment. These species hit a GaAs substrate that is heated to about 600 °C. The sticking coefficient of gallium and aluminum is approximately unity at this substrate temperature. The sticking coefficient of indium is less than one above about 530 °C. The arsenic sticking coefficient depends on the amount of the group III element present. If the surface is covered by the group III element, then the arsenic sticking coefficient is also approximately unity. Stochiometric GaAs crystal growth occurs if there is an overpressure of arsenic vapor. This is required to prevent the formation of gallium droplets [5]. The use of as little extra arsenic as possible has been shown to improve the radiative efficiency of samples, however [6]. The growth rate is determined by the group III arrival rate. The excess arsenic then desorbs from the surface as As_2 or As_4. The growth takes place in a layer by layer mode. Typically the growth occurs at a rate of about one monolayer per second, which corresponds to the formation of about 1 μm per hour.

The compound semiconductors discussed here all crystallize in the zincblende structure. GaAs and AlAs have very similar lattice constants, 5.65 Å and 5.66 Å, respectively. This makes all alloy concentrations easily attainable for any desired thickness. InAs, however, has a larger lattice constant of 6.06 Å. The InGaAs quantum wells in the VCSELs are 80 Å thick layers of $In_{0.2}Ga_{0.8}As$. The $In_{0.2}Ga_{0.8}As$ layer is strained and assumes the in-plane lattice constant of the GaAs substrate. The strain, $\varepsilon_{//}$ is defined as

$$\varepsilon_{//} = \frac{a_{oInGaAs} - a_{oGaAs}}{a_{oGaAs}}. \tag{4.1}$$

For an indium concentration of 20%, this gives a value of 0.015 for $\varepsilon_{//}$, assuming a linear variation with x for the $In_xGa_{1-x}As$ lattice constant between InAs and GaAs. There is a critical thickness below which the material is coherently strained. Above the critical thickness, which is the thickness at which the strain energy in the film is equal to the energy required to form a dislocation, the strain is relaxed through the formation of dislocations. There are several models to calculate the critical thickness [7-9]. For $In_{0.2}Ga_{0.8}As$, the critical thickness is 100-200 Å. Figure 4.2 shows a TEM of three $In_{0.2}Ga_{0.8}As$ quantum wells in the active region of a VCSEL. Figure 4.3 shows a similar structure, but the indium content was miscalibrated and the resulting film has dislocations due to the mismatch in the lattice constants between the quantum wells and the GaAs substrate.

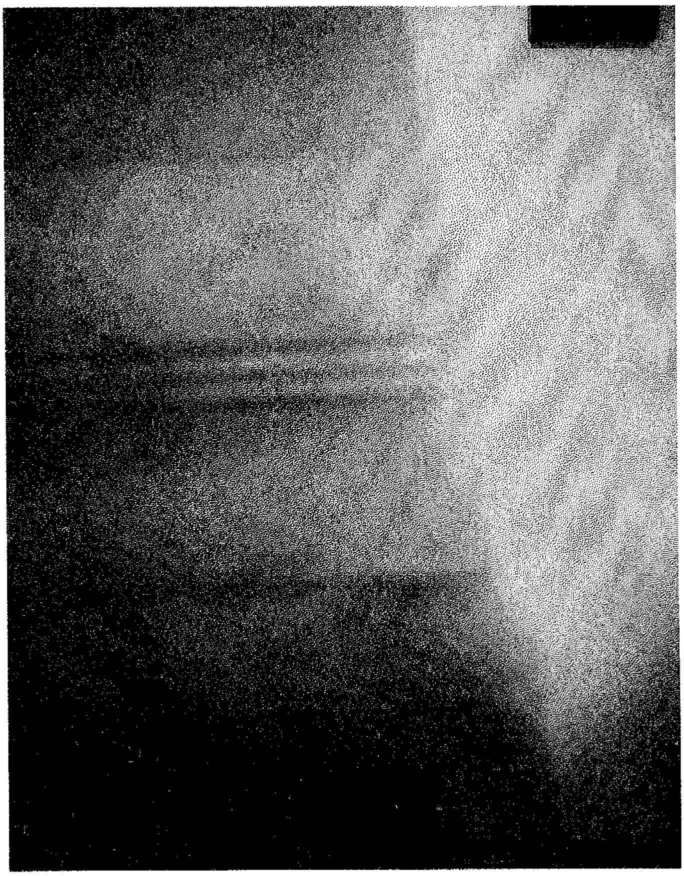

Figure 4.2. TEM cross section of the lower part of the active region of a VCSEL showing the three InGaAs quantum wells and the carrier confinement layers.

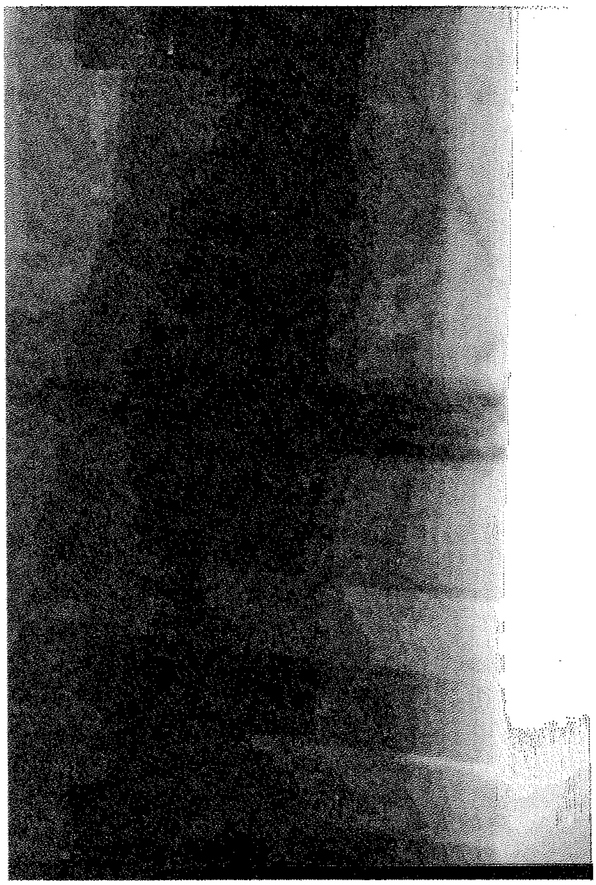

Figure 4.3. A TEM cross section of a VCSEL active region with miscalibrated quantum wells. Dislocations can be seen above the quantum wells.

Section 4.4 Growth Rate Calibration

To obtain the designed thicknesses to within 1%, very accurate determination and control of the growth rate is required. The growth rate is measured by a reflection high-energy electron diffraction (RHEED) apparatus which is located in the main chamber. RHEED can be used to determine an absolute growth rate [10]. The electron beam is incident on the sample at a very small angle (~ 1°) and reflected onto a phosphorous screen. The intensity is detected by a Si photodiode which is connected to a plotter through a current amplifier. The intensity of the reflected beam is periodic with a period that corresponds to the deposition of a layer of the group III element and an arsenic layer, or in other words, $a_0/2$. The intensity of the RHEED pattern is largest for a smooth surface and it becomes smaller as the growth begins and the surface roughens. When a monolayer is completed the intensity is again at its peak. The amplitude of the oscillations is damped as growth begins occurring on several layers at once. Figure 4.4 shows the intensity of the reflected beam versus time for the deposition of AlAs. The deposition rate is not constant in time. It is slightly faster immediately after the shutter is opened than it is in its steady state. This is attributed to the shutter reflecting heat at the cell so that the cell cools slightly after the shutter is opened. This is the reason that the 1" spacers were placed between the cell and the chamber for the two aluminum cells and the gallium cell. Without the spacers, the growth rate can be as much as 15% higher for the first few monolayers. With the spacers, the transient is reduced to 3.5-4%.

The growth rate calibration is then checked with the growth of a Bragg reflector. The reflectivity of the Bragg reflector is measured and compared with the reflectivity that is calculated using the model described in chapter 3. The thickness can be inferred by comparing the width of the high reflectivity region and the spectral locations of the reflectivity minima to the model. In practice RHEED was done before a series of VCSELs were grown and the reflectivity was checked after every wafer.

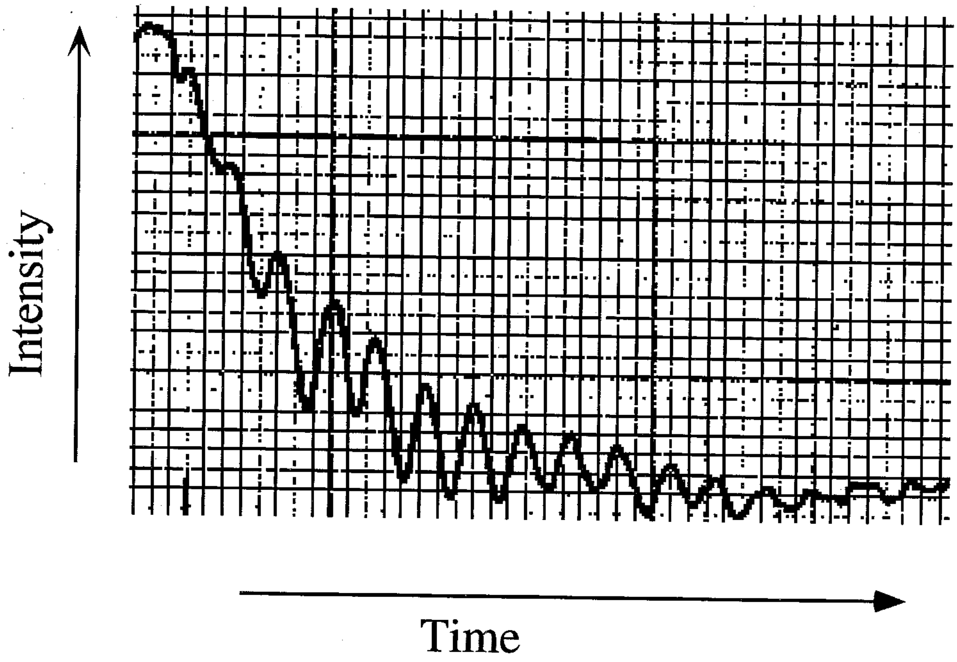

Figure 4.4. RHEED oscillations during the growth of AlAs.

In addition to an accurate determination of the growth rates, the rates must be very reproducible. The cell temperatures are controlled and are constant to within 0.1 °C. Also, the substrate temperature was chosen to be between 580-600 °C so that the sticking coefficient of gallium is unity. This compromises optical quality, which is better at 700 °C because of oxygen incorporation as described in section 4.6, but results in reproducible growth rates. The gallium sticking coefficient is unity up to about 640 °C [11-12]. Above this temperature, the sticking coefficient and hence, the growth rate decreases with increasing substrate temperature. Precise control of the substrate temperature is very difficult, so growth was done at a temperature where the rate was not sensitive to variations in the substrate temperature. The indium sticking coefficient is less than unity above about 530 °C so the substrate was lowered below this temperature for the growth of the quantum wells [13].

Section 4.5 Wafer Uniformity

It is usually important for the thickness to be uniform over as large a region of the wafer as possible. The uniformity depends on the effusion cell geometry and on the substrate temperature uniformity. The nonuniformity caused by the cell geometry can be reduced by rotating the wafer during growth [14]. The wafers grown for this work were rotated at a speed of about 14 revolutions/minute. The substrate temperature uniformity is important for high substrate temperatures, > 640 °C for GaAs and > 530 °C for InGaAs. An effort was made to keep the substrate temperature below these values for their respective growth. The substrate temperature was lowered about 10 nm, or 30 seconds, before the quantum wells were grown but the growth was not interrupted. The exact substrate temperature for the quantum well growth is not known, but the emission of the three quantum wells is a single peak indicating that the three wells have very nearly the same thickness and indium concentration. Even with the low substrate temperature and the rotating substrate, the InGaAs peak luminescence wavelength and the wavelength of the Fabry-Perot wavelength resonance changed by 30 nm or more from the center to the edge of a 2" wafer. Figure 4.5(a) shows the Fabry-Perot resonance wavelength as a function of position across the wafer and figure 4.5(b) shows the peak luminescence wavelength for InGaAs quantum wells across the wafer. The wafer nonuniformity can also be useful, however. During the growth of the fully semiconductor VCSELs emitting at 850 nm, the wafer was not rotated during the top half of the optical cavity for the first few wafers. This was done to ensure the overlap of the gain peak and the Fabry-Perot mode wavelength for some region of the wafer.

Section 4.6 Incorporation of Oxygen

An important problem in the growth of semiconductor lasers, particularly VCSELs, is oxygen incorporation in AlGaAs. Oxygen is a deep non-radiative acceptor-like trap in $Al_xGa_{1-x}As$ [15-17]. In addition, oxygen incorporation leads to rough interfaces, especially the inverted interface of GaAs on AlGaAs. The interface roughness is attributed to oxygen segregating in the AlGaAs and being gettered at the GaAs/AlGaAs inverted interface [18-20]. Beryllium doped films show a greater oxygen incorporation than silicon doped films, possibly due to the formation of Be-O compounds which are stable at the growth temperature [21]. An additional problem with oxygen incorporation is that ternary AlGaAs layers tend to roughen with oxygen incorporation. This has been attributed to the formation of AlAs clusters [18]. The AlAs clusters, which will be favored if the oxygen level is large, will serve as nucleation sites where the growth rate is faster.

Substrates misoriented a few degrees towards <111>A have been shown to reduce the oxygen incorporation and reduce or eliminate interface roughness. This was attributed to the <111>A misoriented surfaces having a smaller number of dangling bonds than the (100) on-orientation surfaces [22]. Also, it has been reported that for miscut substrates,

(a)

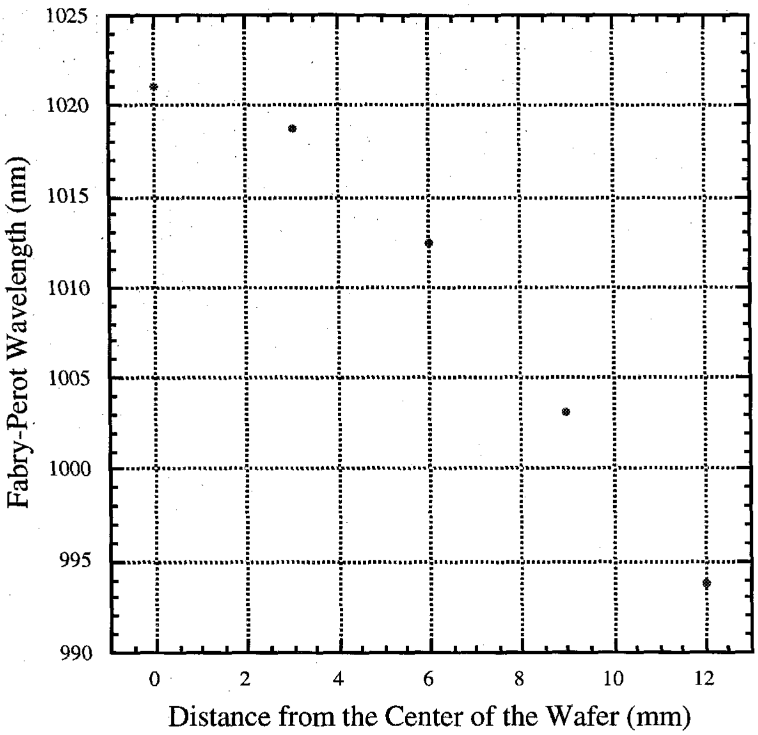

(b)

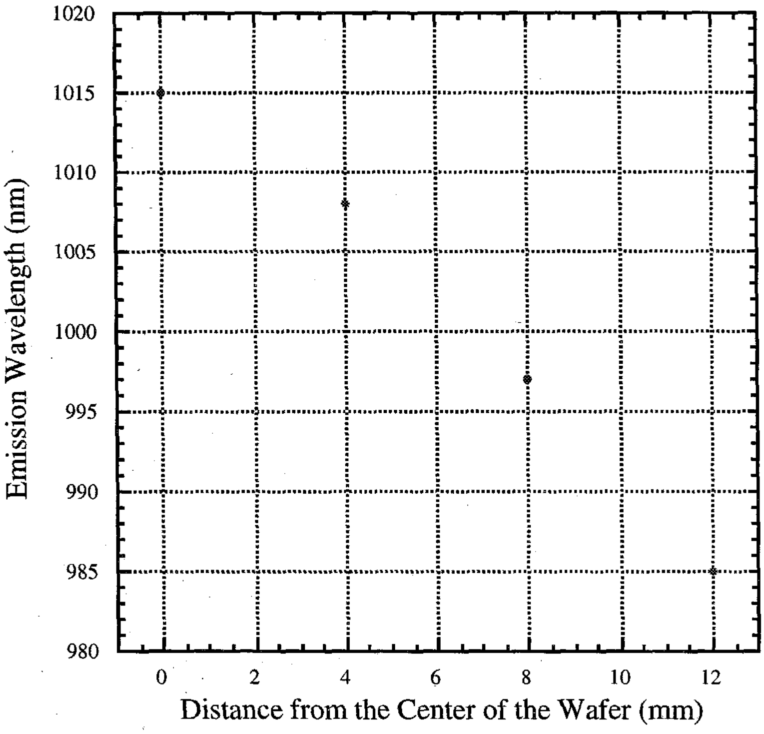

Figure 4.5. (a) The Fabry-Perot wavelength variation across the wafer.
(b) The InGaAs quantum well emission peak variation acrosso the wafer.

there is no forbidden region between 640 and 680°C where the film is not smooth and the surface is hazy [23]. Traditionally the highest quality AlGaAs is grown above this forbidden region at 700 °C. SIMS measurements made on two GaAs double heterostructure edge-emitting lasers, one grown at 600 °C and one grown at 700 °C, do show greater oxygen incorporation in the sample grown at 600 °C, figure 4.6, than the sample grown at 700 °C, figure 4.7. The sample grown at 600 °C has a large oxygen peak in the cladding and failed to lase. There is one report that J_{th} is independent of substrate temperature if As_2 is used instead of As_4, but this has not been observed in our system. In any case, 700 °C is not suitable to the growth of VCSELs because the gallium incorporation is temperature dependent at these temperatures and exact control of the substrate temperature is very difficult.

The VCSELs grown for this thesis were grown at a substrate temperature between 580 and 600 ° C to obtain precise reproducible growth rates. The optical cavity of two of the 850 nm GaAs lasers were grown at a substrate temperature of 700 °C in an effort to improve the radiative efficiency of the material, but the cavity resonance was badly misalligned in both cases. One sample produced lasers, but the emission wavelength was around 815 nm instead of the designed 850nm. All the samples were grown on on-axis (100) n+ substrates using As_2. It was found that the AlGaAs/AlAs Bragg reflectors were more likely to roughen than the binary AlAs/GaAs mirrors. Figure 4.8 shows an SEM of a binary AlAs/GaAs Bragg reflector and figure 4.9 is an SEM of a AlAs/AlGaAs Bragg reflector which displays the roughness that was sometimes seen in mirrors containing a ternary layer. Both types of mirrors could be grown with sufficient smoothness to produce VCSELs, however. The InGaAs VCSELs were designed with as little AlGaAs in the structure as possible. Two thin AlGaAs layers were included around the quantum wells for carrier confinement. The rest of the optical cavity was GaAs, and the mirrors were binary AlAs/GaAs. This was not possible for the 850 nm GaAs VCSELs because GaAs is absorbing at this wavelength. The VCSELs containing InGaAs quantum wells were grown

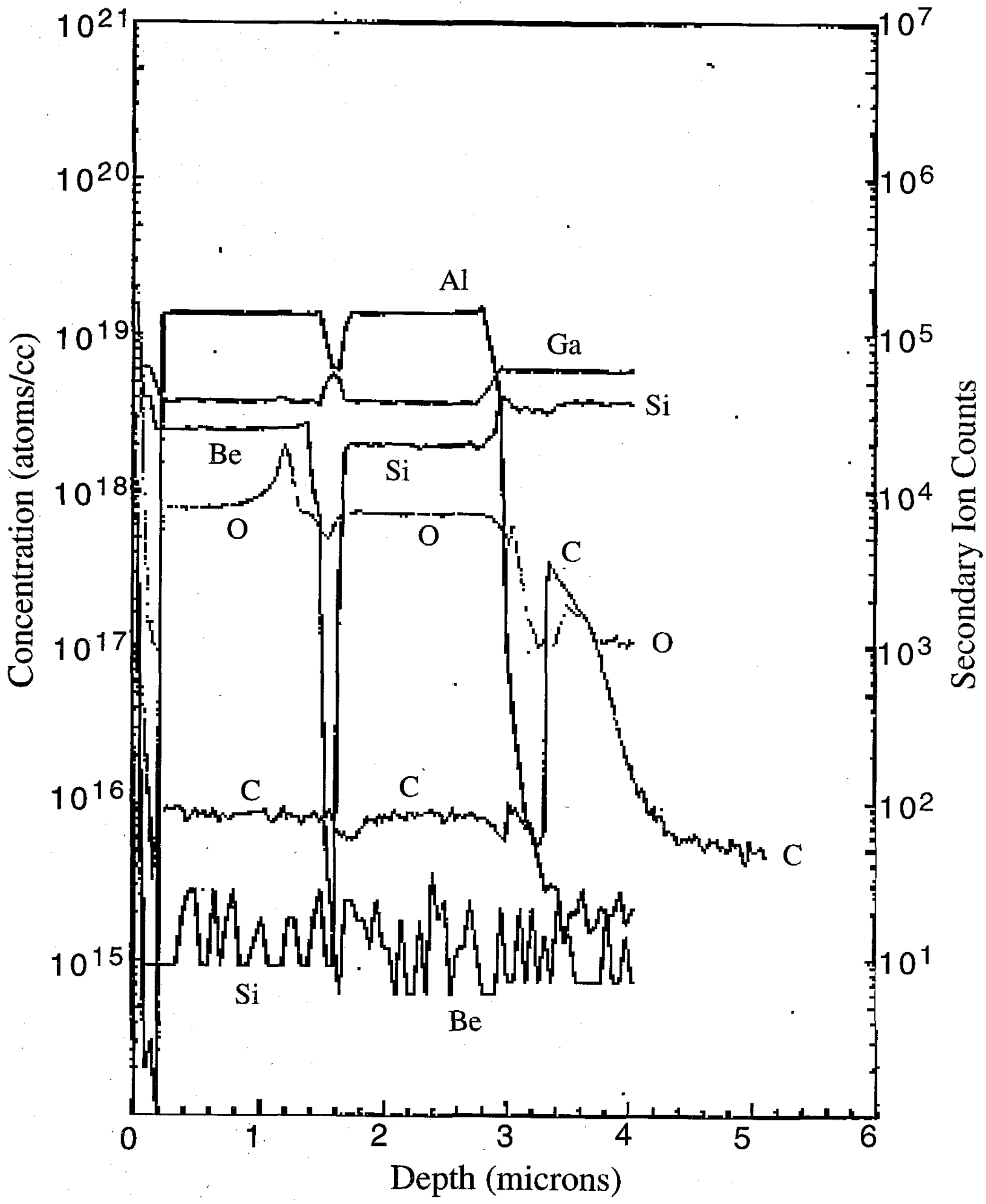

Figure 4.6. A SIMS measurement of a GRINSCH laser grown at 600 degrees C. There is a large oxygen peak in the top AlGaAs cladding layer.

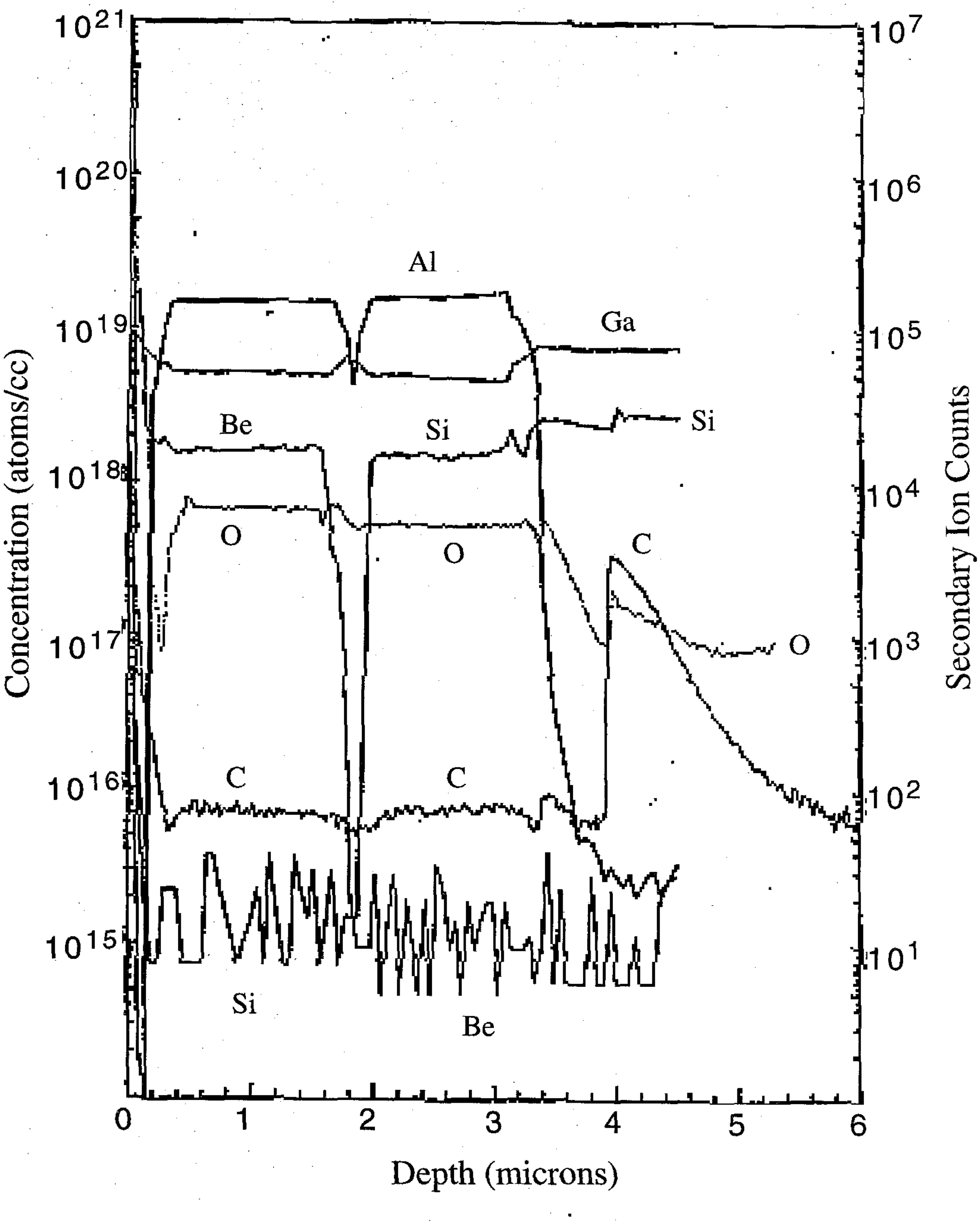

Figure 4.7. A SIMS measurement of a GRINSCH laser grown at a substrate temperature of 700 degrees celsius. Note the oxygen level for this sample is lower than for the sample shown in figure 4.6.

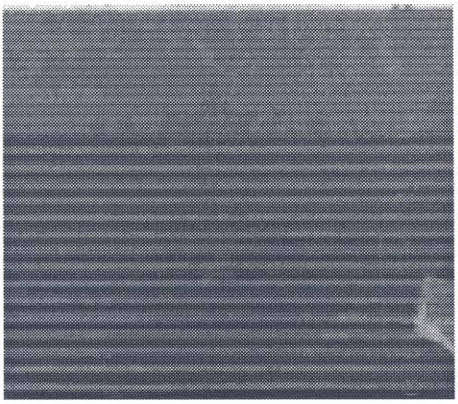

Figure 4.8. SEM micrograph of a distributed Bragg reflector containing GaAs and AlAs layers.

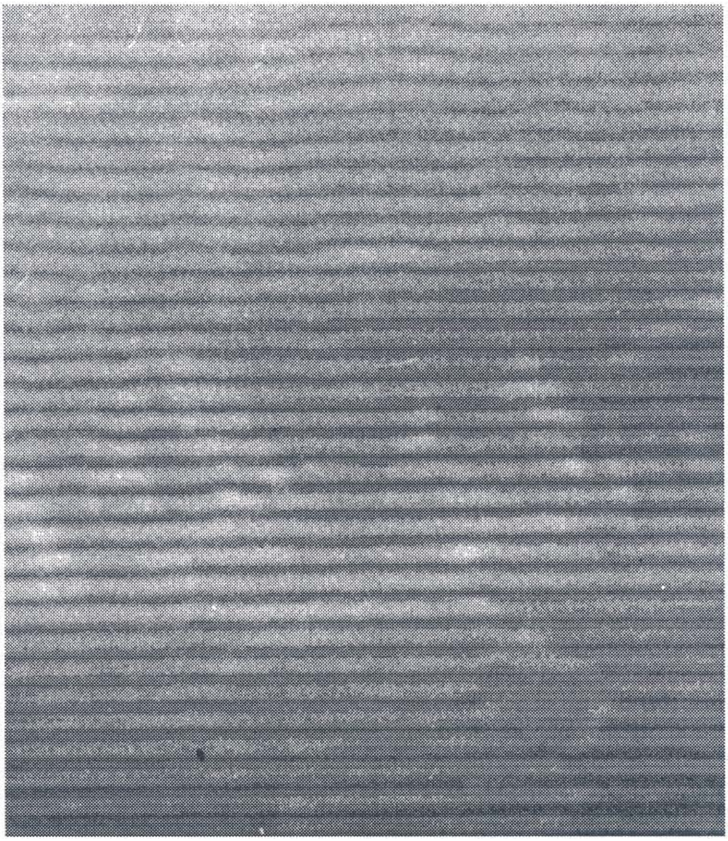

Figure 4.9. SEM micrograph showing a distributed Bragg reflector containing ternary AlGaAs layers. The roughness often seen in AlGaAs layers at low growth temperatures is visible.

about 100 wafers after the previous MBE opening. This amount of material growth was expected to clean up the most likely source of oxygen contamination in the MBE chamber, the aluminum and arsenic source material. Edge-emitting lasers were grown at 600 °C first, before VCSELs were attempted. These lasers were of very poor quality with pulsed threshold currents of 3 A or higher, suggesting that the system was not clean enough to grow thick high quality AlGaAs layers at this substrate temperature. Figure 4.10 shows a SIMS measurement of a good VCSEL wafer, with only two thin AlGaAs layers, showing low levels of oxygen are present.

4.7 Doping

Silicon and beryllium were used as dopants for these structures. Silicon can be used to produce electron concentrations as high as $6x10^{18}$ cm^{-3} [24]. Above ~ 10^{18} cm^{-3}, however, silicon starts to occupy arsenic sites as well as gallium sites [2], so silicon levels were kept to $3x10^{18}$ cm^{-3} and below. Beryllium can be doped to $5x10^{19}$ cm^{-3} in GaAs [25], but it has been shown to diffuse at dopant levels above 10^{18} cm^{-3} [26]. This can displace the p-n junction. Beryllium diffusion has been seen in lasers grown at substrate temperatures of 700 ° C [27]. Figure 4.11 shows a SIMS measurement of a GaAs single quantum well GRINSCH laser structure where beryllium diffusion can clearly be seen. This sample was grown at a substrate temperature of approximately 700 °C. At a substrate temperature of 600 °C, beryllium diffusion seems to be less of a problem. One group reported negligible beryllium diffusion at this temperature [28], and another group obtained ≤ 350 Å halfwidth beryllium pulses [25]. This is important because in a VCSEL the doping levels are varied to heavily dope regions where the optical field is small and lightly dope regions where the optical field is largest. This is done to reduce optical absorption losses. Figure 4.12 shows a SIMS measurement of the optical cavity of a VCSEL grown at a substrate temperature between 580 and 600 °C. The intended doping was $1x10^{19}$ cm^{-3}

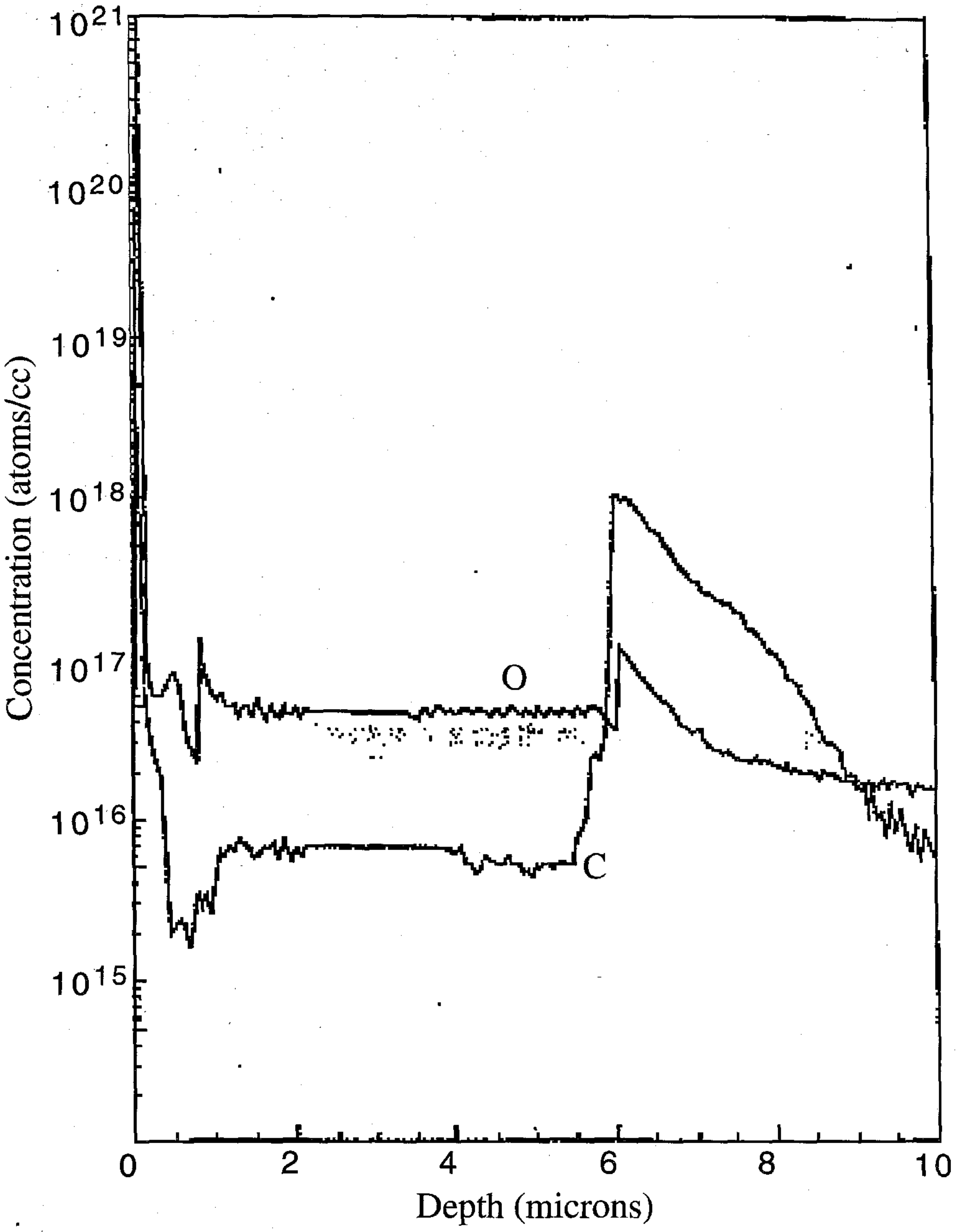

Figure 4.10. A SIMS measurement of a VCSEL structure. Note there are no large oxygen peaks in the active region.

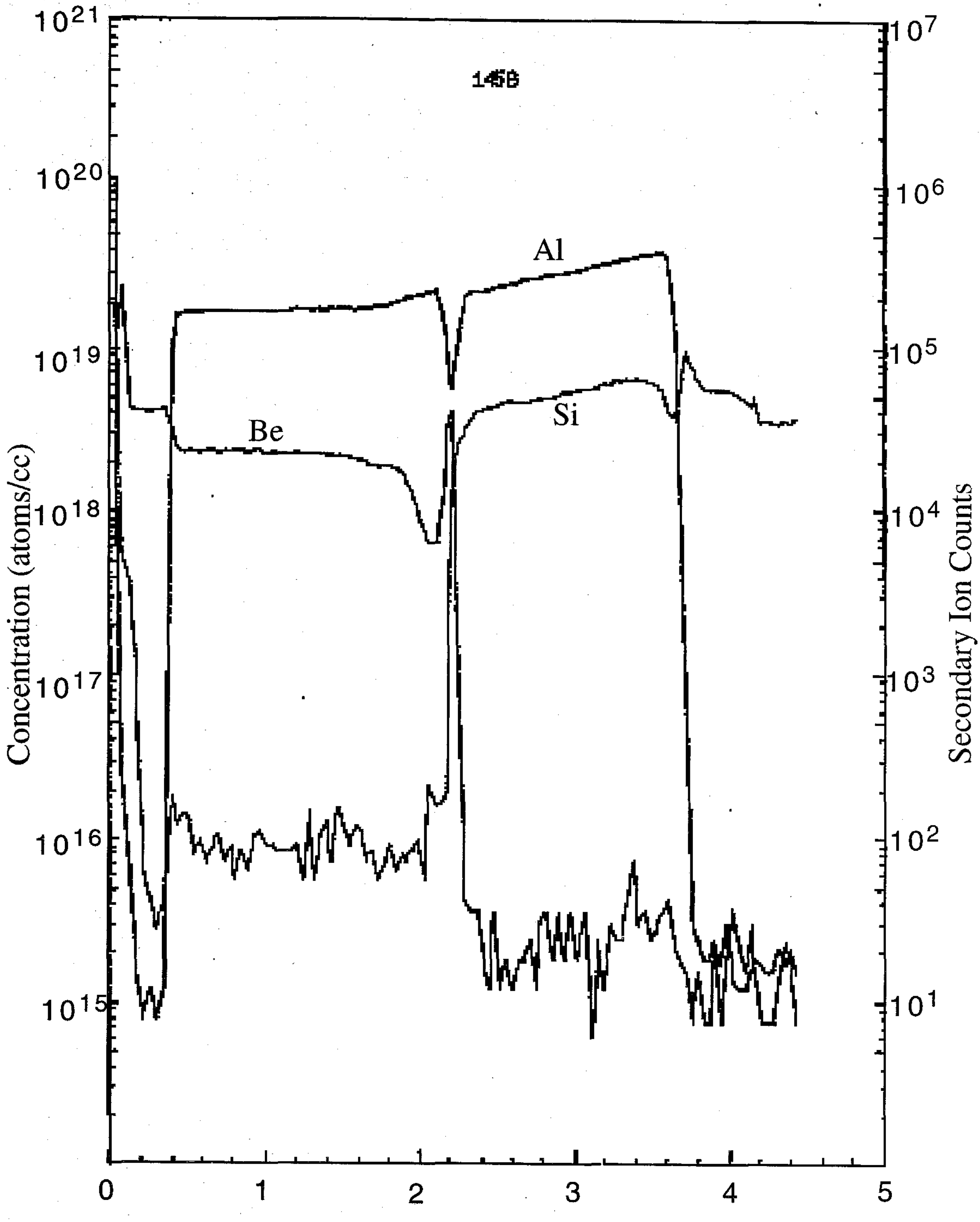

Figure 4.11. A SIMS measurement of a GRINSCH laser grown at 700 degrees celsius. The Be diffusion can clearly be seen in the GRINSCH region.

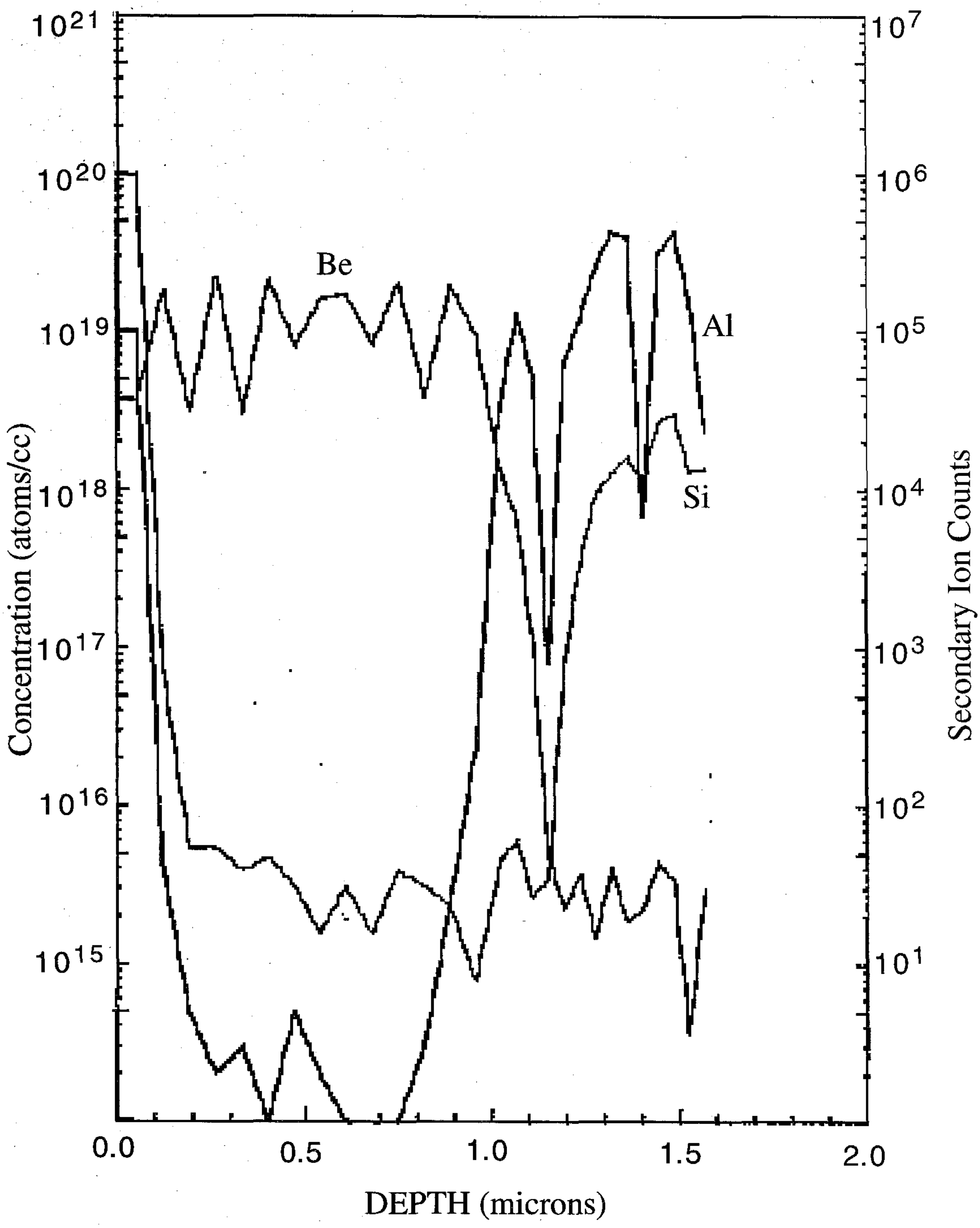

Figure 4.12. A SIMS measurement of the top contact region of a VCSEL structure with layered doping. The sample was grown at 600 degrees celsius and the Be peaks are well seperated.

for the quarter wavelength around the optical field node and $1\text{x}10^{18}$ cm^{-3} for the quarter wavelength around the optical field peak. The beryllium peaks in the SIMS can be seen clearly and are separated.

In addition, oxygen incorporation in beryllium-doped films has been reported to be higher than in silicon-doped films [20]. The SIMS measurements made on samples for this thesis also show this behavior. To deal with beryllium diffusion and oxygen incorporation, the n-side of the p-n junction is doped up to the quantum well, while the p-side of the GRINSCH is undoped. Beryllium doping begins in the cladding about 100 nm away from the quantum well active region.

4.8 Conclusions

Reproducible and accurate growth rates were demonstrated by the growth of VCSELs. To obtain these results careful attention must be paid to the shutter transients and the substrate temperature. This accuracy also compromises the optical quality of the material by increasing the incorporation of oxygen in the AlGaAs, and an effort was made to limit the amount of AlGaAs in structures that required growth at low substrate temperature. Beryllium diffusion has also been seen at a substrate temperature of 700 °C and care must be taken in the placement of the beryllium near the quantum wells or the p-n junction can shift away from the quantum wells.

References

[1] A.Y. Cho, *Thin Solid Films*, **100**, 291 (1983)

[2] B.A. Joyce, *Rep. Prog. Phys.*, **48**, 1637 (1985)

[3] J. N. Miller, *J. Vac. Sci. Technol.*, **B 10**, 803 (1992)

[4] A. Zangwill, *Physics at Surfaces*, Cambridge University Press, Cambridge (1992)

[5] J. Y. Tsao, *Materials Fundamentals of Molecular Beam Epitaxy*, Academic Press, San Diego (1993)

[6] L. E. Eng, Ph. D. Thesis, California Institute of Technology (1993)

[7] J. W. Mathews, A. E. Blakeslee, *J. Cryst. Growth* , **27**, 118 (1974)

[8] R. People, J. C. Bean, *Appl. Phys. Lett.*, **47**, ? (1985)

[9] L. H. van der Merwe, *J. Appl. Phys.*, **34**, ? (1963)

[10] J. H. Neave, B. A. Joyce, *App. Phys. A*, **31**, 1 (1983)

[11] E. M. Gibson, C. T. Foxon, J. Zhang, B. A. Joyce, *Appl. Phys. Lett.*, **57**, 1203 (1990)

[12] R. Fischer, J. Klem, T. J. Drummond, R. E. Thorne, W. Kopp, H. Morkoc, A. Y. Cho, *J. Appl. Phys.*, **54**, 2508 (1983)

[13] J. L. Jewell, J. P. Harbison, A. Scherer, Y. H. Lee, L. T. Florez, *IEEE J. Quant. Elect.*, **27**, 1332 (1991)

[14] A. Y. Cho, K. Y. Cheng, *Appl. Phys. Lett.*, **38**, 360 (1981)

[15] C. T. Foxon, T. S. Cheng, P. Dawson, D. E. Lacklison, J. W. Orton, W. Van der Vleuten, O. H. Hughes, M. Henini, *J. Vac. Sci. Tech.*, **B12**,1026,(1994)

[16] J. Orton, P. Dawson, D. E. Lacklison, T. S. Cheng, C. T. Foxon, *Semicond. Sci. Technol.*, **9**, 1616 (1994)

[17] W. T. Tsang, *Appl. Phys. Lett.*, **33**, 245 (1978)

[18] M. T. Asom, M. Geva, R. E. Leibenguth, S. N. G. Chu, *Appl. Phys. Lett.*, **59**, 976 (1991)

[19] T. Achtnich, G. Burri, M. A. Py, M. Ilegems, *Appl. Phys. Lett.*, **50**, 1730 (1987)

[20] N. Chand, S. N. G. Chu, A. S. Jordan, M. Geva, V. Swaminathan, *J. Vac. Sci. Technol.*, **B10**, 807 (1992)

[21] N. Chand, A. S. Jordan, S. N. G. Chu, M. Geva, *Appl. Phys. Lett.*, **59**, 3270 (1991)

[22] Y. H. Wang, K. Tai, Y. R. Hsieh, S. N. G. Chu, J. D. Wynn, M. Hong. R. J. Fischer, A. Y. Cho, *J. Crystal Growth*, **111**, 1057 (1991)

[23] N. Chand, S. N. G. Chu, M. Geva, *Appl. Phys. Lett.*, **59**, 2874 (1991)

[24] Y. G. Chai , R. Chow, C. E. C. Wood, *Appl. Phys. Lett.*, **39**, 800 (1981)

[25] M. Ilegems, *J Appl. Phys.*, **48**, 1278 (1978)

[26] G. E. Kohnke, M. W. Koch, C. E. C. Wood, G. W. Wicks, *Appl. Phys. Lett.*, **66**, 2786 (1995)

[27] V. Swaminathan, N. Chand, M. Geva, P. J. Anthiny, A. S. Jordan, *J. Appl. Phys.* **72**, 4648 (1992)

[28] J. N. Miller, D. M. Collins, N. J. Moll, *Appl. Phys. Lett.*, **46**, 960 (1985)

Chapter 5

Vertical Cavity Lasers Emitting Near 980 nm with SiO_2/Si_3N_4 Top Mirrors

5.1 Introduction

This chapter will discuss the results for the VCSELs that were grown and fabricated with InGaAs quantum wells in the active region. These lasers are a hybrid semiconductor/dielectric structure. This kind of device was demonstrated previously with GaAs quantum wells emitting at 850 nm [1]. The chapter will begin with a description of the structure and of the fabrication steps involved. The fabrication was done in Professor Axel Scherer's lab and will be described here for completeness. The chapter will also describe the measurements that were made both on the lasers and on the same material before the top mirrors were in place. An advantage of this design is that it allows some characterization at the light emitting diode stage that is not possible in fully semiconductor VCSELs, including a measurement of the temperature distribution in the cavity while the diodes were being pumped and the spatial resolution of the spontaneous emission. The temperature measurements included in this chapter were made by the Barnes Engineering Division of EDO Corporation.

5.2 The Hybrid Structure

The VCSELs discussed in this chapter are a hybrid semiconductor/dielectric structure. Figure 5.1 shows a schematic cross section of this structure. The n-doped bottom mirror and the active region are grown by MBE. The bottom mirror is a 28 1/2 period AlAs/GaAs distributed Bragg reflector. No intermediate AlGaAs concentrations are included in this mirror because the resistance of the n-doped mirror is relatively small, ~ 50 Ω. The Si doping concentration is $3\text{x}10^{18}$ cm^{-3} in the mirror and $1\text{x}10^{18}$ cm^{-3} in the optical cavity. The optical cavity contains a Si-doped quarter wavelength of $Al_{0.5}Ga_{0.5}As$ which serves as a barrier for carrier confinement and as a spacer layer to place the quantum wells at the peak of the standing wave of the optical field. This is followed by a 50 nm layer that is linearly graded from $Al_{0.5}Ga_{0.5}As$ to GaAs. Then there are three 80 Å $In_{0.2}Ga_{0.8}As$ quantum wells with a 100 Å GaAs spacer between each. These are followed by an undoped linearly graded region and an $Al_{0.5}Ga_{0.5}As$ spacer layer, Be doped to $1\text{x}10^{18}$ cm^{-3}. These layers are symmetric with the layers below the quantum wells. Then a 834 nm, three optical wavelengths long, GaAs layer Be doped to $3\text{x}10^{18}$ cm^{-3} was grown. This is the layer to which the top contact was made. The doping profile was later modified to enhance current uniformity as will be discussed later. The top mirror was a SiO_2/Si_3N_4 Bragg reflector that was sputtered on. Other dielectric materials such as CaF_2 and ZnSe have also been reported in top mirrors [2]. In this design, the current does not pass through a p-doped mirror. This simplifies the epitaxial growth because reducing the resistance of a p-doped Bragg reflector would require a number of intermediate bandgap steps between AlAs and GaAs as well as varying doping levels to reduce the barriers to hole transport. Very

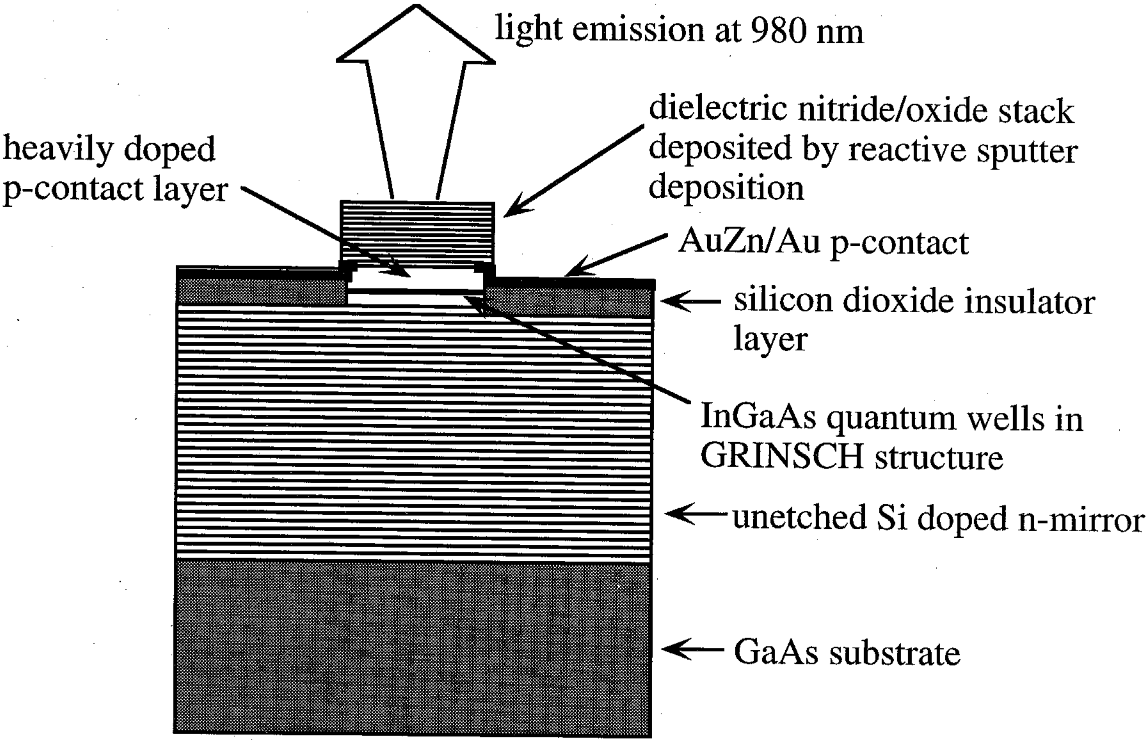

Figure 5.1 A schematic cross section of the hybrid semiconductor/dielectric VCSEL.

low resistance p-mirrors have been reported as discussed in Chapter 1 but it complicates the MBE growth. The optical cavity is surrounded by SiO_2, which is a planarization layer for the top contact and also serves to index guide the optical mode. The top contact was made to the outside rim of the etched pillars. The lasers are top emitting and the n-contact is made to the back of the wafer.

5.3 Fabrication

Individual laser elements were defined by ion etching mesas 0.9 μm deep through the p-n junction in a 1 keV Ar^+ ion beam assisted by a flux of chlorine reactive gas and using a photoresist mask. The same mask was used to lift-off the 300 nm sputter-deposited SiO_2 planarization layer. After another photolithography step, AuZn/Au p-contacts were deposited on top of the diodes. A AuGe/Au contact was evaporated on the back of the wafer. The contacts were not alloyed. At this point the diode emission wavelength was measured and the top mirror adjusted to tune the resonance wavelength if necessary. A final lithography step was performed to define the lift-off mask for the dielectric mirror deposition. The top SiO_2/Si_3N_4 mirror was then deposited by reactive sputter deposition. Figure 5.2 shows the fabrication sequence. Lasers ranging in size from 6 to 30 μm in diameter were fabricated. Figure 5.3 shows a photograph of some of the devices fabricated with this mask set including five rows of individual laser elements as well as 4x4 arrays and an 8x8 array. Figure 5.4 shows a magnified view of an 8x8 array with one laser operating, and figure 5.5 shows an SEM photograph of the cross-section of the diode.

5.4 Diode Characterization

One of the most important advantages of the hybrid/dielectric structure is the ability to measure the emission of the diode before the top mirror is deposited. This section will

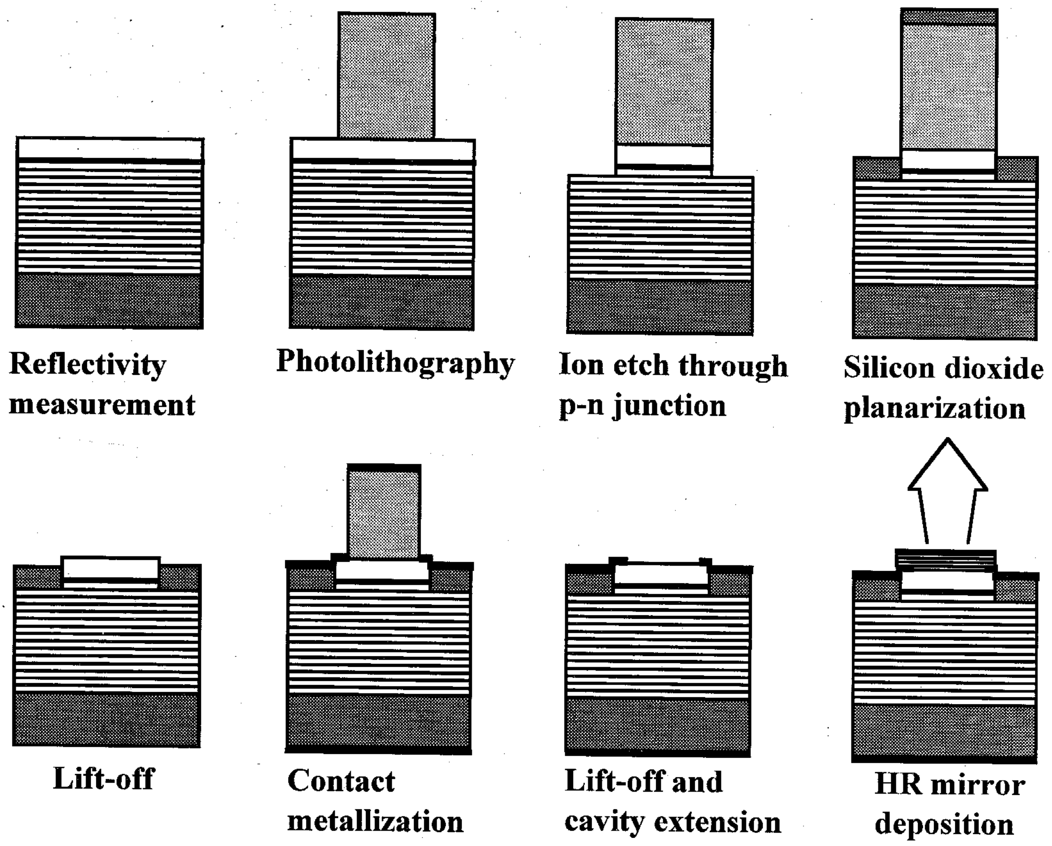

Figure 5.2. An illustration of the fabrication procedure for the hybrid VCSELs.

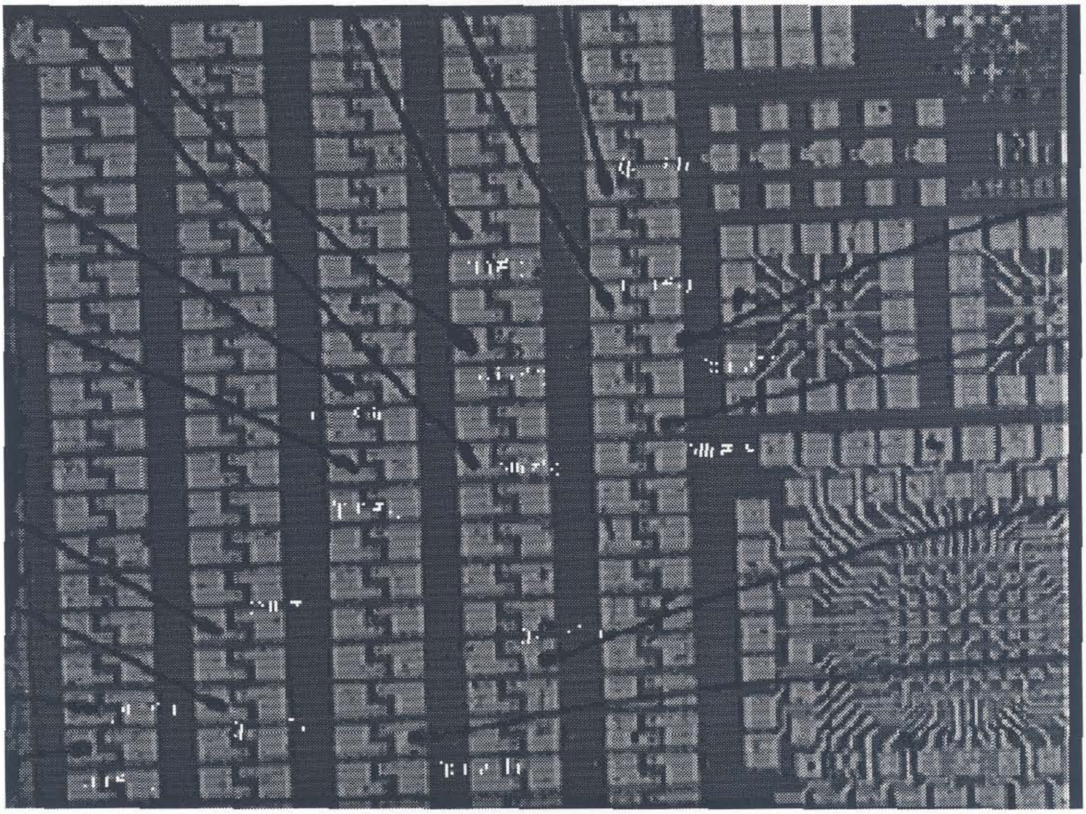

Figure 5.3. A CCD image taken through a microscope to illustrate the mask used to fabricate these lasers.

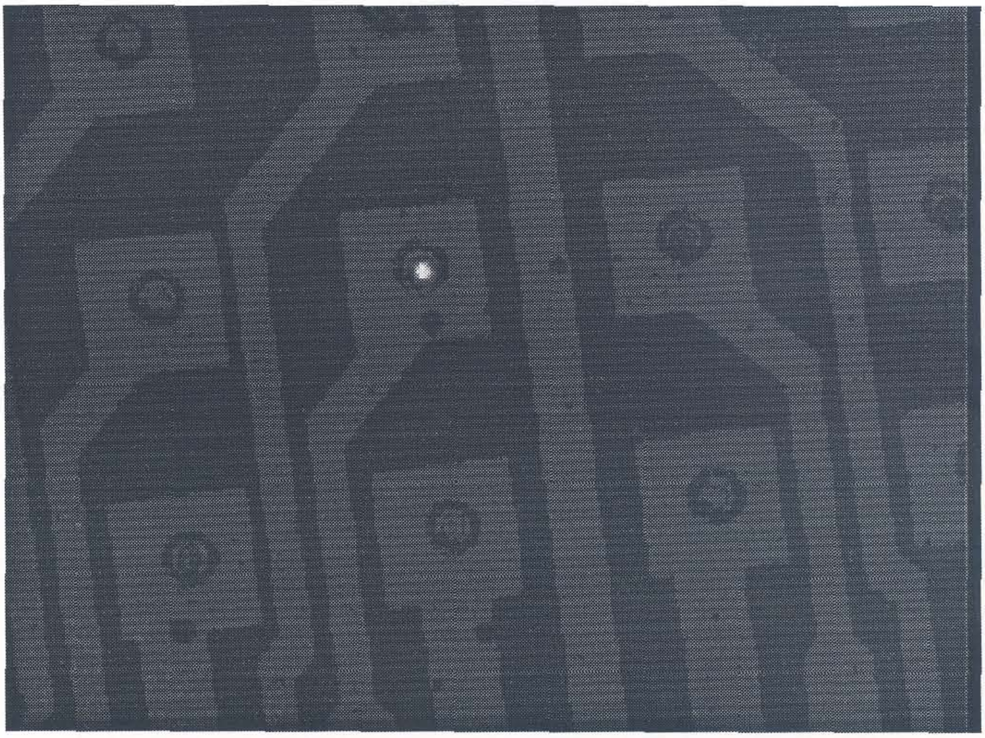

Figure 5.4. A higher magnification view of the 8x8 array with one laser operating.

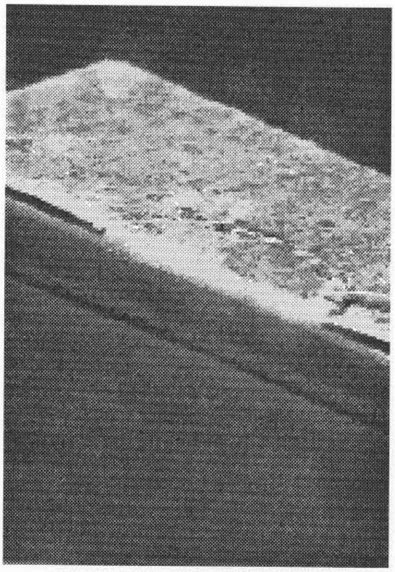

Figure 5.5. An SEM image of the cross section of the hybrid structure without the top mirror.

start by describing the typical characterization done on the diodes. In addition, the spatial distribution of the carriers can be found from the spontaneous emission distribution. Section 5.4.2 will describe the spontaneous emission distribution and a model to explain the data. Section 5.4.3 will present an experimental measurement of the temperature of the diodes while being electrically pumped.

5.4.1 Typical Characterization

The Fabry-Perot wavelength is known from the reflectivity measurement of the grown wafer. Once the emission peak of the quantum wells is known, the dielectric deposition can be adjusted to tune the cavity resonance if necessary. Typically the I-V curve and spectral emission were also measured after the initial processing was finished. Figure 5.6 shows a typical I-V characteristic of a 30 μm diode. The series resistance is low because there are no p-doped mirrors in the current path. The slope of the I-V curve in figure 5.6 corresponds to a series resistance of 50 Ω, which is mainly attributed to the n-doped Bragg reflector. Figure 5.7 shows the emission spectrum of the three InGaAs quantum wells.

5.4.2 Current Spreading

It was observed that the spontaneous emission from the diode was not spatially uniform. The emission was brightest around the outside edge of the devices. Figure 5.8 shows a photograph, taken with a CCD camera through a microscope, of the diode emission and the corresponding intensity profile. The spatial distribution of the spontaneous emission intensity reflects the carrier distribution in the quantum wells. It was also observed that the larger lasers tended to operate in a very high order mode with the intensity concentrated around the outside rim of the laser as shown in Figure 5.9. This suggests a larger spatial overlap between the gain and the high order ring modes. The

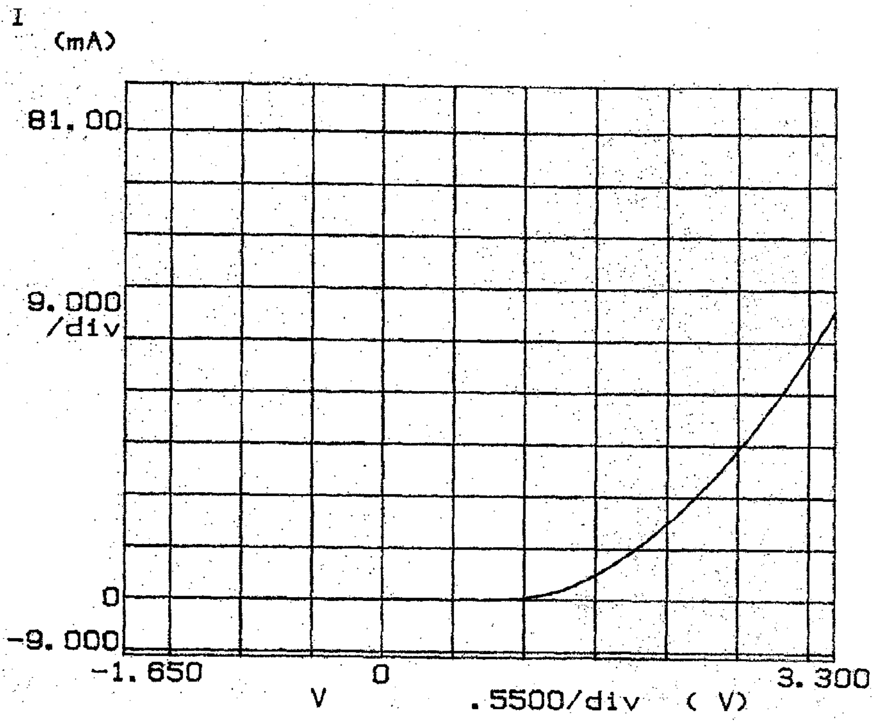

Figure 5.6. An I-V characteristic for a 30 μm diameter device

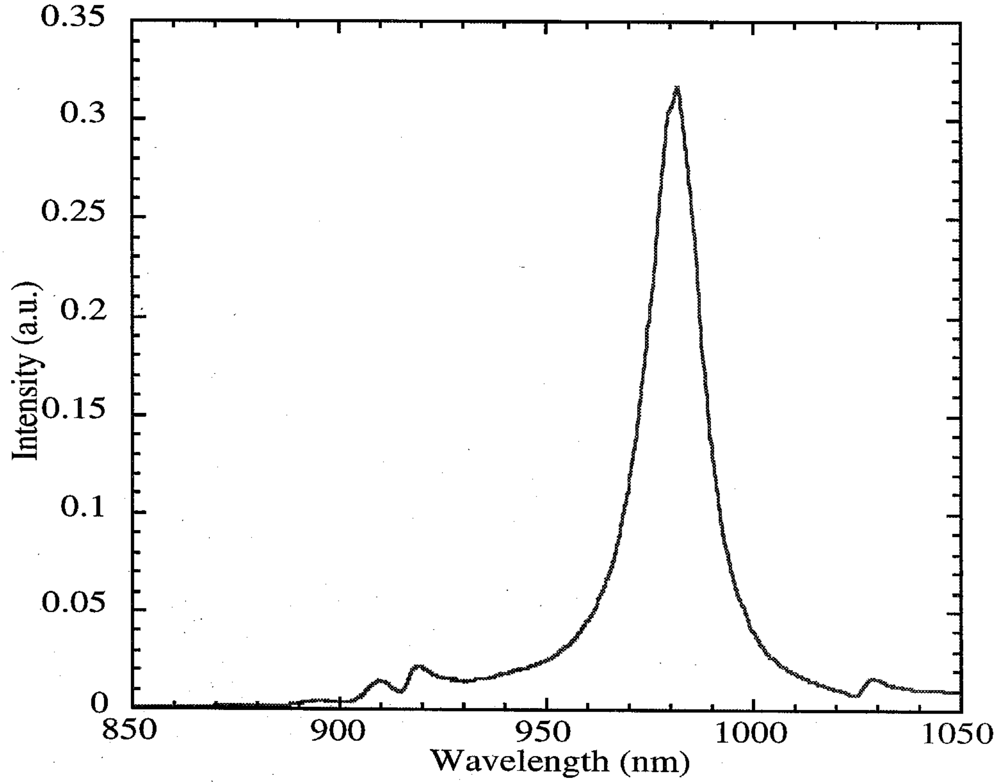

Figure 5.7. A typical emission spectra obtained from the three InGaAs quantum wells.

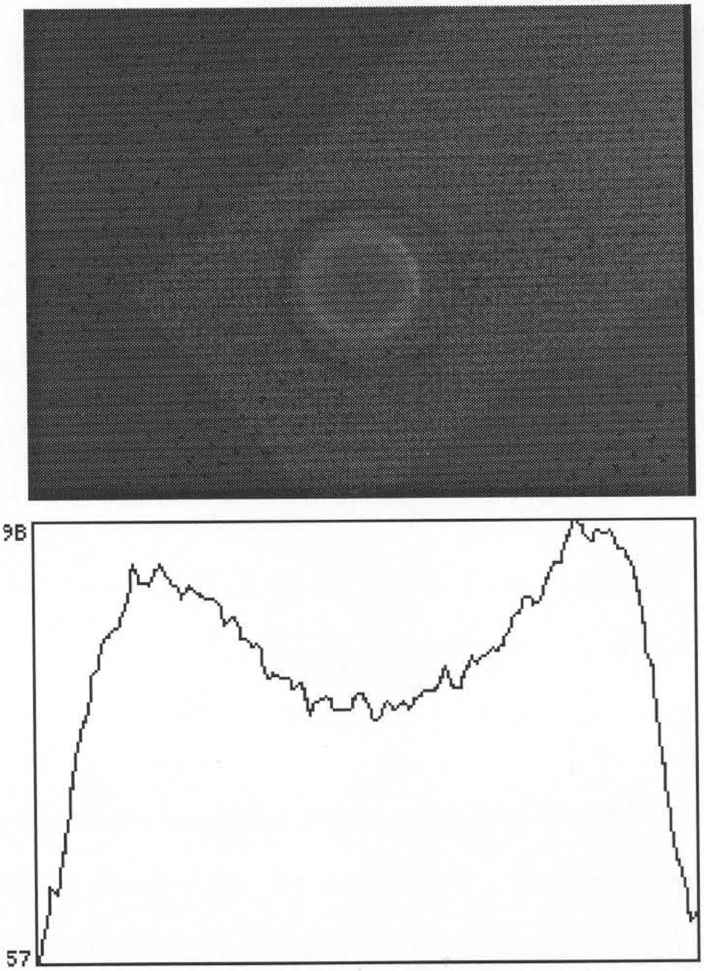

Intensity across the diode

Figure 5.8 Image of the spontaneous emission from a diode and the corresponding intensity.

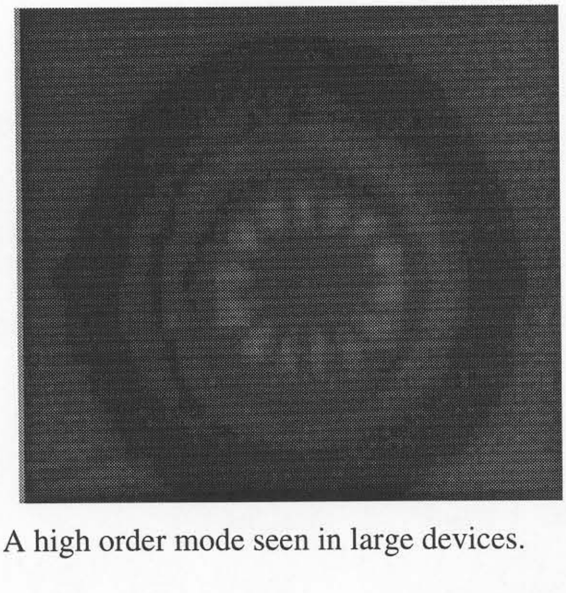

Figure 5.9. A high order mode seen in large devices.

carrier distribution was modeled with an approach following references [3] and [4]. The model is a solution of the current density in a cylindrical geometry for the p-doped contact layer using the ideal diode equation and Ohm's law for the sheet current in the layer. The solution assumes that the sheet resistivity is homogeneous and isotropic and that the voltage drop perpendicular to the junction is negligible. Once the current density is calculated, it is then used in the diffusion equation as the source term to solve for the carrier density. The numerical solution of the diffusion equation was done by Reg Lee in reference [5]. Another reported approach is to model the contact layer by a resistor network and use SPICE to calculate the current profile [6]. The method used here starts with the diode equation

$$I = I_o\left(\exp\left(\frac{qV(r)}{nkT}\right)-1\right) \tag{5.1}$$

where I_o is the reverse saturation current and n is the ideality factor. For forward bias the 1 can be dropped compared to the exponential. The sheet current, C(r), parallel to the junction plane satisfies

$$\hat{r}\frac{\partial V}{\partial r} = -\hat{r}\rho C(r) \tag{5.2}$$

Current passing out of the p region goes through the junction, so we can write

$$-\frac{1}{r}\frac{\partial}{\partial r}C(r)= J(r) \tag{5.3}$$

Taking the divergence of equation (5.2) and combining it with equation (5.1) gives

$$\frac{1}{\rho}\left(\frac{1}{r}\frac{\partial}{\partial r}\left(r\frac{\partial V}{\partial r}\right)\right) = J_o\exp\left(\frac{qV(r)}{nkT}\right) \tag{5.4}$$

The solution of this equation, subject to the condition that the sheet current is zero at r=0, can be found analytically using the change of variables given in [3] and [4]. The solution is

$$J(r) = \frac{-I_{tot}^{2} J_R \beta \rho}{8 J_o R^2 \pi^2}\left(1 - \frac{8\pi}{\beta \rho I_{tot}}\right)\left[1 - \frac{\beta \rho I_{tot}}{8\pi}\left(1 - \left(\frac{r}{R}\right)^2\right)\right]^{-2} \tag{5.5}$$

where I_{tot} is the total diode current, R is the diode radius, and β is q/nkT. This is then used as the source term in the diffusion equation that is solved numerically for the carrier density distribution in the quantum wells. Figure 5.10 shows a measured spontaneous emission profile and a curve fit solution that was calculated from the model. Figure 5.10(a) shows an image of the diode, and (b) contains the data and the result of the model (solid line). The discreteness of the CCD image is apparent in the data.

An effort was made to get a more uniform carrier distribution in the quantum wells in order for the fundamental mode to have a better overlap with the gain profile. It was found that by forming layers of high conductivity sandwiched between layers of lesser conductivity, a uniform spontaneous emission profile could be obtained. The new structure had layers in the three wavelength contact region of the optical cavity that were Be-doped to 10^{19} cm^{-3}. These layers were one-quarter of the optical wavelength thick and were centered around the zero of the standing wave in the cavity. The quarter wavelength where the optical field was at its peak was doped 1×10^{18} cm^{-3}. Figure 5.11 shows a schematic illustration of the optical field and the doping distribution in the top region of the optical cavity. Figure 5.12 shows the measured spontaneous emission profiles and images of the spontaneous emission for structures with and without the layered doping. The threshold gain calculated by the method described in Chapter 3 is nearly identical for the two doping schemes. Only one set of working lasers was fabricated from the wafers with

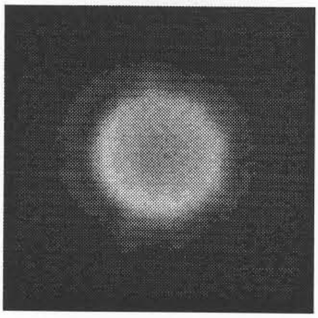

(a)

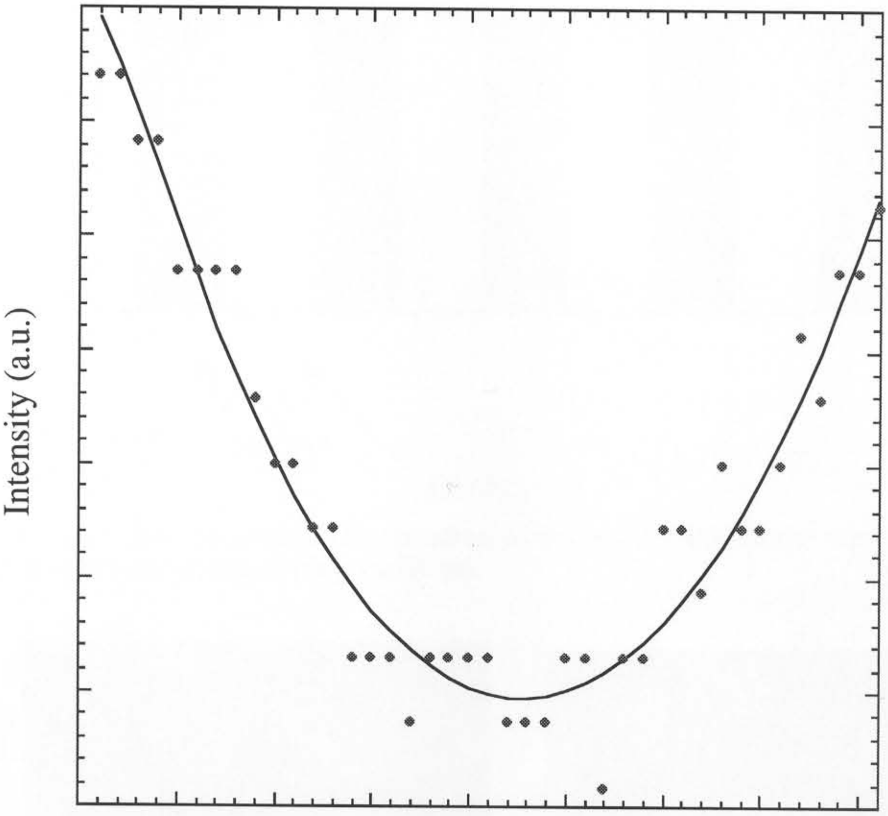

(b)

Figure 5.10. (a) shows the diode and (b) is a plot of the measured spontaneous emission intensity profile (dots) and the calculated intensity profile.

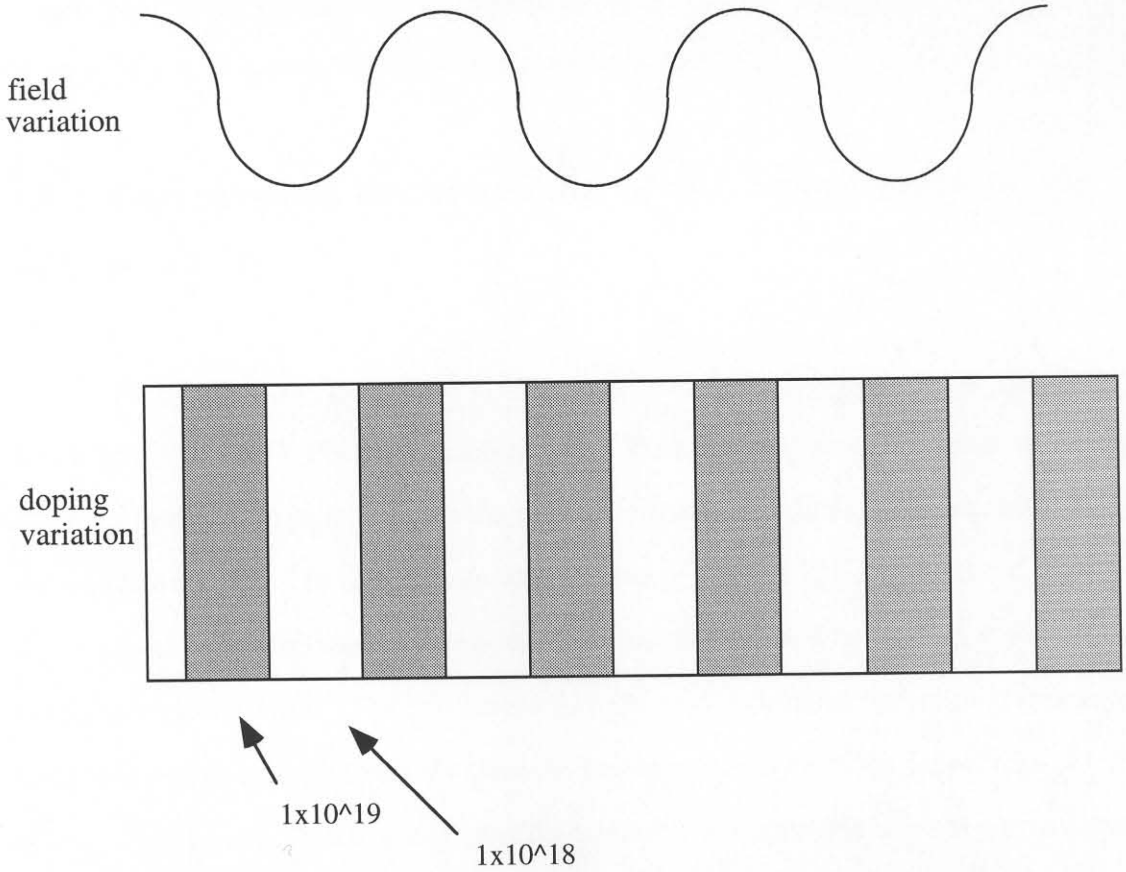

Figure 5.11. A schematic of the variation of the optical field in the top of the optical cavity and the corresponding doping variation.

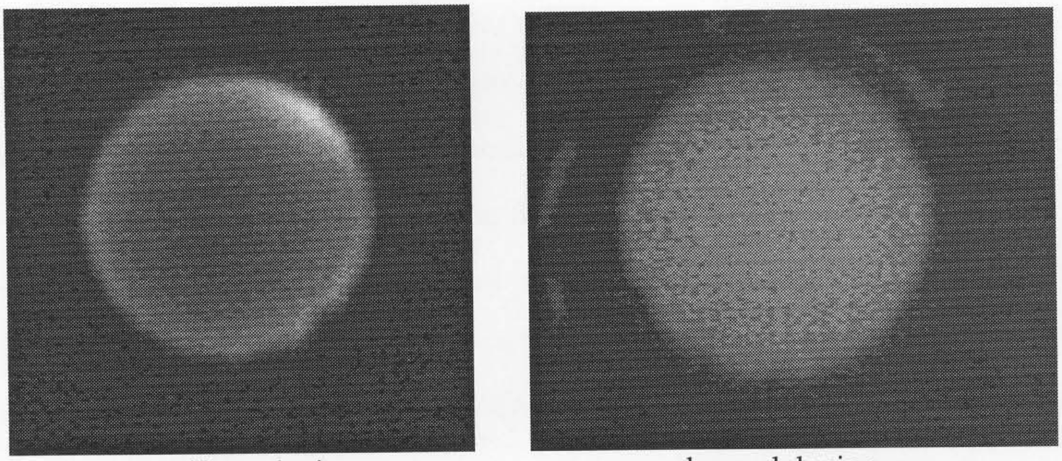

uniform doping

layered doping

Figure 5.12. Images of the spontaneous emission for a device with uniform doping showing a nonuniform carrier distribution and a device with the layered doping showing a much more uniform carrier distribution.

spike doping so it is difficult to say anything conclusive about the lasing mode when the carrier distribution was uniform. However, the 3-0 mode was only found in the large devices, 30 μm diameter, for the layered doping sample.

5.4.3 Experimental Determination of the Temperature in the Optical Cavity

There are many reports of a theoretical model for the temperature of the active region in a VCSEL [7-10]. The temperature of the active region is important is designing VCSELs because the gain peak and the resonance wavelength change at different rates with temperature changes. To compensate for this, many designs [11-13] shift the gain to the blue with respect to the resonant wavelength so that the two will be aligned at the operating temperature of the laser. The fabrication of light emitting diodes before the fabrication of lasers allowed us to experimentally characterize the temperature of the active region. If the emissivity is known, then by measuring the intensity of thermal radiation in a given spectral region, the temperature can be determined. Figures 5.13 and 5.14 show typical results of the temperature measurements. These measurements were made by the Barnes Engineering Division of EDO Corporation. The diodes were pumped electrically and imaged by InSb detectors that had a spectral response between 1.5 and 5.5 μm. The measurement has a spatial resolution of 4 μm and a temperature resolution of 0.02 °C. The responsivity of each pixel was corrected for in obtaining the temperature plot. Measurements of four devices were made from three different sizes. The bias was 25 mA for all four measurements. The maximum temperature measured was 101.6 °C for a 24 μm device. The mean temperature was 82-83 °C for all four devices. The temperature does not appear to be uniform across the diode. Each device contained small regions that were at least 5 °C hotter than other parts of the dry-etched pillar.

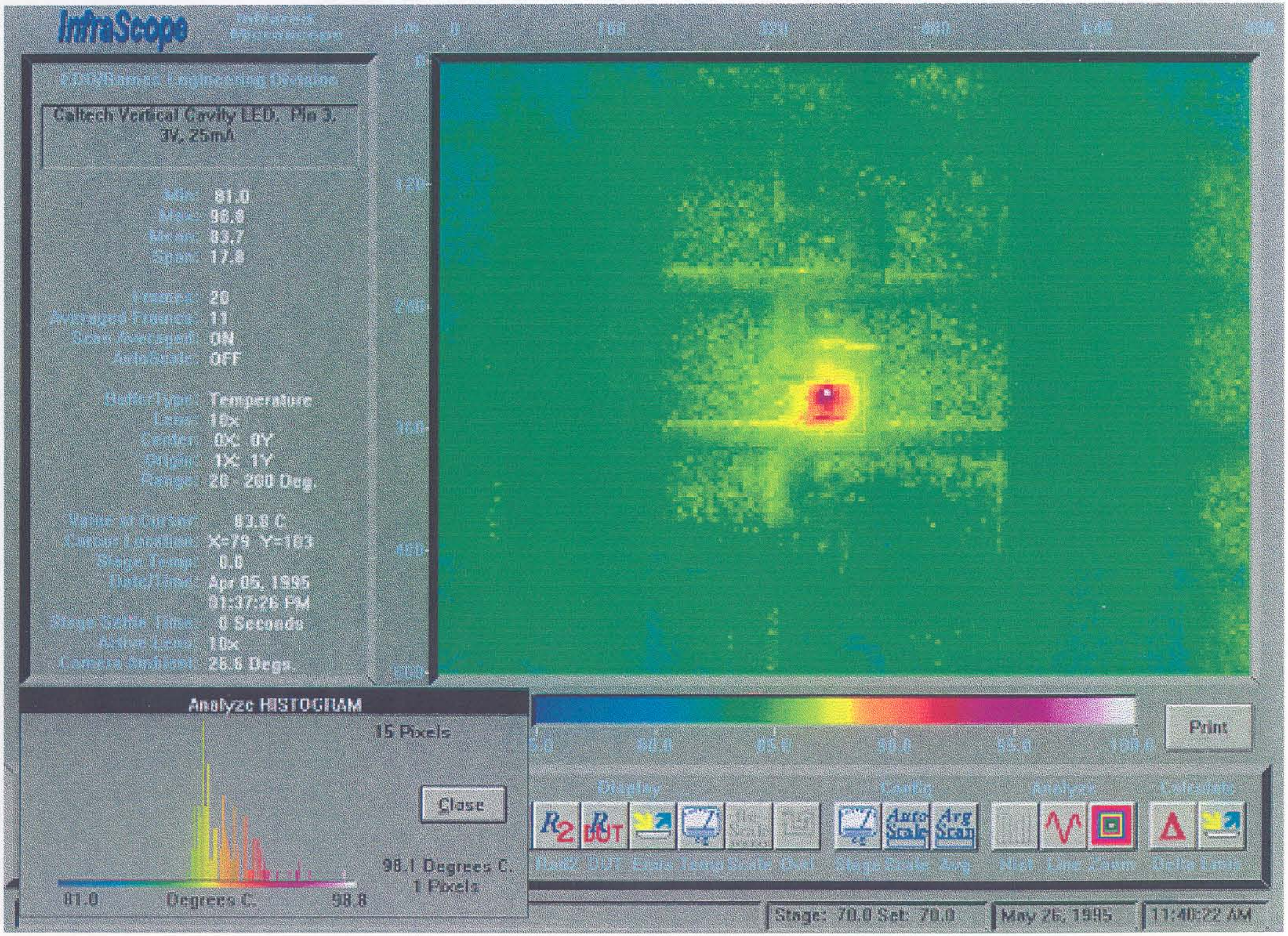

Caltech Vertical Cavity LED. Pin 3.
3V, 25mA

Min: 81.0
Max: 98.8
Mean: 83.7
Span: 17.8

Frames: 20
Averaged Frames: 11
Scan Averaged: ON
AutoScale: OFF

Buffer Type: Temperature
Lens: 10x
Center: 0X: 0Y
Origin: 1X: 1Y
Range: 20 - 200 Deg.

Value at Cursor: 83.8 C
Cursor Location: X=79 Y=183
Stage Temp: 0.0
Date/Time: Apr 05, 1995
01:37:26 PM
Stage Settle Time: 0 Seconds
Active Lens: 10x
Camera Ambient: 26.6 Degs.

Analyze HISTOGRAM

15 Pixels

98.1 Degrees C.
1 Pixels

81.0 Degrees C. 98.8

Stage: 70.0 Set: 70.0

May 26, 1995

11:40:22 AM

Figure 5.13. A thermal image of an operating vertical cavity LED.

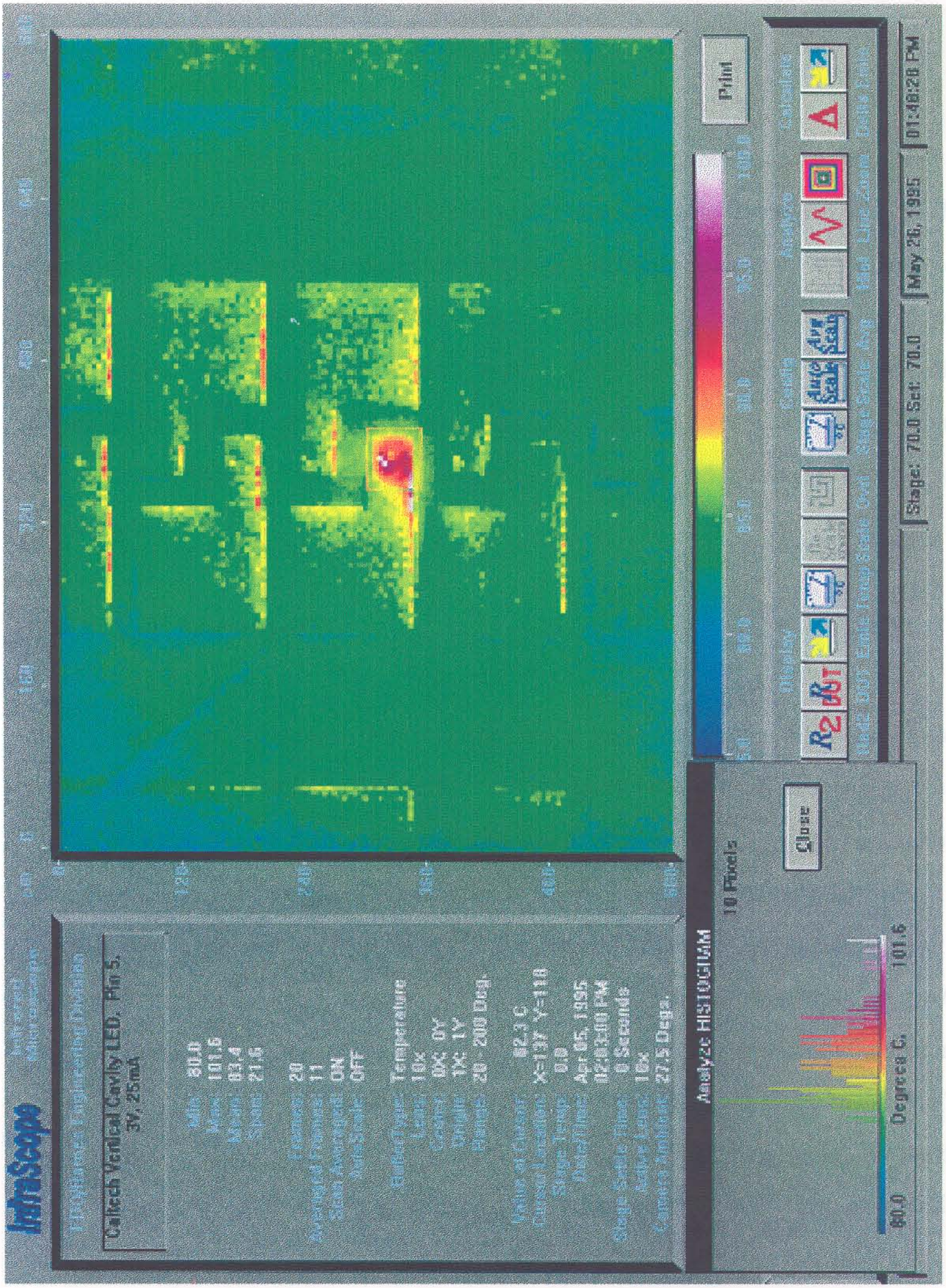

Caltech Vertical Cavity LED, Pin 5.
3V, 25mA

Min: 80.0
Max: 101.6
Mean: 83.4
Span: 21.6

Frames: 20
Averaged Frames: 11
Scan Averaged: ON
AutoScale: OFF

BufferType: Temperature
Lens: 10x
Center: 0X: 0Y
Origin: 1X: 1Y
Range: 20 - 200 Deg.

Value at Cursor: 82.3 C
Cursor Location: X=137 Y=118
Stage Temp: 0.0
Date/Time: Apr 05, 1995
02:03:00 PM
Stage Settle Time: 0 Seconds
Active Lens: 10x
Camera Ambient: 27.5 Degs.

Stage: 70.0 Set: 70.0
May 26, 1995
01:48:28 PM

Figure 5.14. Another thermal image of an active vertical cavity LED.

5.5 Laser Performance

After the diodes were characterized, a SiO_2/Si_3N_4 Bragg reflector was sputtered on the device. Most of the lasers described here had 10 dielectric pairs in the top mirror. The light output versus current was measured as well as the lasing spectrum and the near field pattern. Lasers were fabricated with 28 1/2 and 26 1/2 bottom mirror pairs as well as with uniform $3x10^{18}$ cm^{-3} doping and layered $1x10^{18}/1x10^{19}$ cm^{-3} doping in the cavity. The results discussed here are for the devices with 28 1/2 mirror pairs and uniform doping. The devices with 26 1/2 mirror pairs had near field patterns and spectra similar to those shown here.

5.5.1 L-I Behavior

The lowest threshold current measured was 2.5 mA. This value was obtained from a 6 μm diameter laser under pulsed conditions. The pulse width was 20 nsec at a repetition rate of 30 kHz. Figure 5.15 shows the spectrum of this device at threshold and above. Threshold currents increased with device size as expected and were typically 5-7 mA for 12 μm diameter lasers. Surface recombination is expected to contribute a major portion of the threshold current in these lasers. Using the rule of thumb that there is 1A/cm recombination current for every cm of exposed GaAs or InGaAs would mean that approximately 70 % or 1.8 mA of the 2.5 mA threshold current is lost at the surface. This would reduce the threshold current density from 8.8 kA/cm^2 to 2.5 kA/cm^2. In another report [14], 62% of the threshold current of a 10 μm diameter laser was attributed to surface recombination.

The largest peak power measured was 1.67 mW. This was obtained from a 12 μm diameter laser under pulsed operation. Figure 5.16 shows the L-I curve of this device.

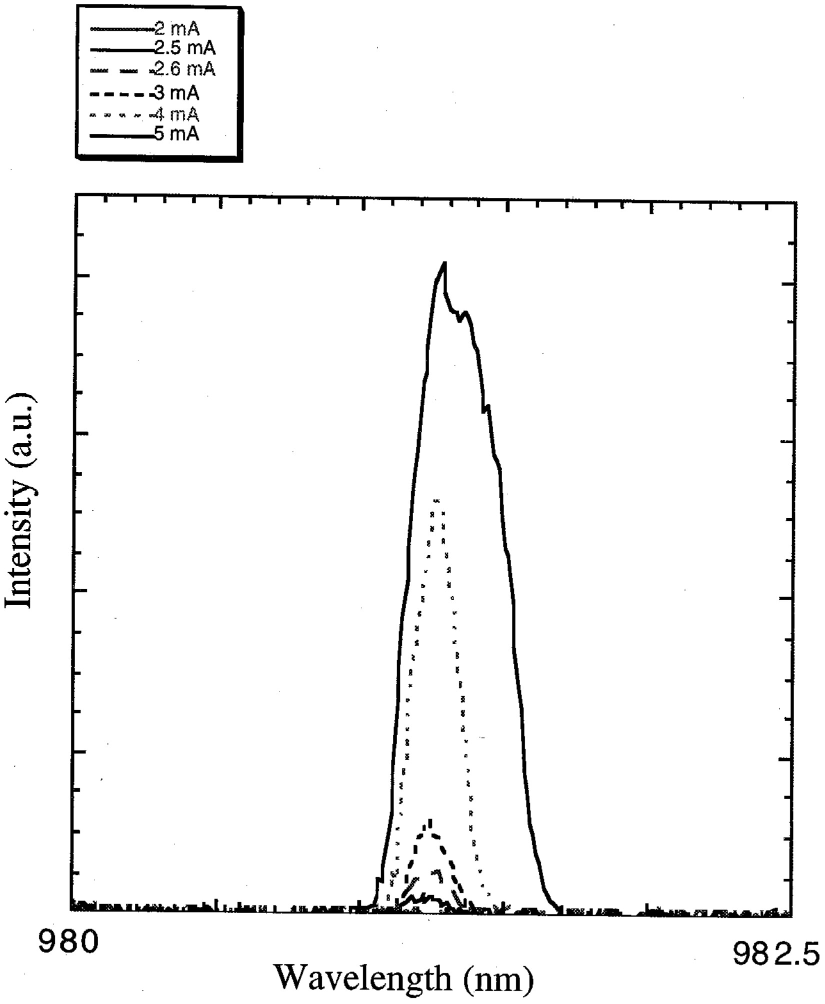

Figure 5.15 The emission spectra from a 6 μm diameter device at bias currents from 2 mA to 5 mA.

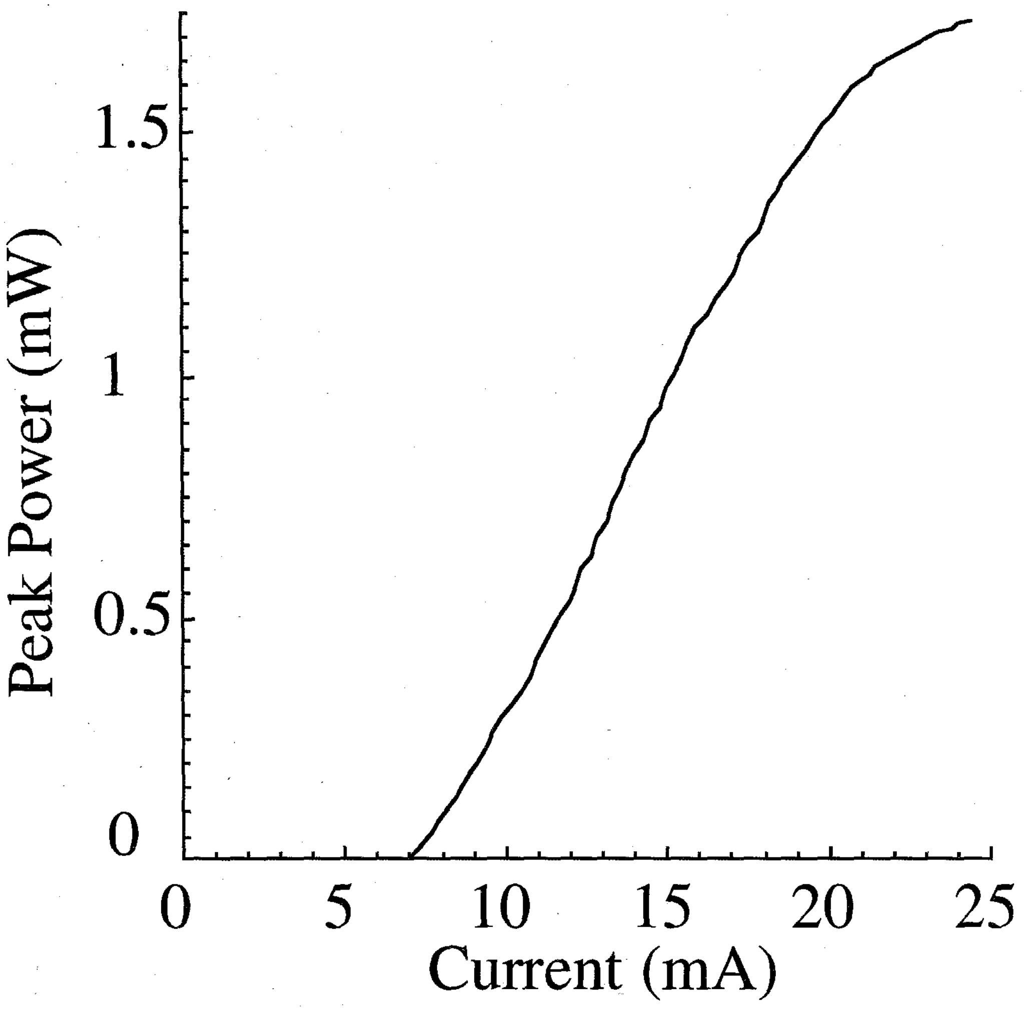

Figure 5.16 The L-I characteristic of the device which produced the highest peak power.

Smaller devices produced lower peak powers as expected; a 6 μm diameter laser produced a peak power of 1.06 mW. The larger lasers did not produce higher powers. This is attributed to their high threshold currents which may result from the very high order mode operation of these lasers.

The lowest threshold voltage measured was 1.8 V, obtained from a 12 μm diameter device. The smaller devices had slightly higher voltages at threshold due to the increased series resistance. The larger 30 μm diameter lasers had the lowest series resistance and so were expected to have even lower threshold voltages, but they did not due to their increased threshold currents.

CW threshold currents were typically higher than the pulsed threshold currents. The size and the direction of the change in threshold current with duty cycle depends, however, on the spectral alignment of the gain and the cavity resonance. The maximum output power was also lower for the lasers under CW operation. This was attributed to heating of the active region. Figure 5.17 shows a typical pulsed L-I curve. The curve bends over at 6.4 mA. This rollover is a general characteristic of VCSELs. It is due to the peak gain wavelength and the cavity resonance wavelength redshifting with temperature at different rates so that as the device is operated at higher currents, the gain and resonant wavelength move out of alignment. This rollover can also be thought of as an effective increase in the threshold current, so as the operating current is increased it is effectively operating closer to threshold and the output power decreases. This thermal rollover is repeatable and is not catastrophic. The change in emission wavelength with increasing current was measured to be about 0.34 nm/mA for cw operation for the hybrid devices. This effect is larger for cw operation where the operating temperature is higher. It is expected that these thermal effects are more severe in structures incorporating dielectric mirrors instead of semiconductor mirrors because the dielectrics have a lower thermal conductivity.

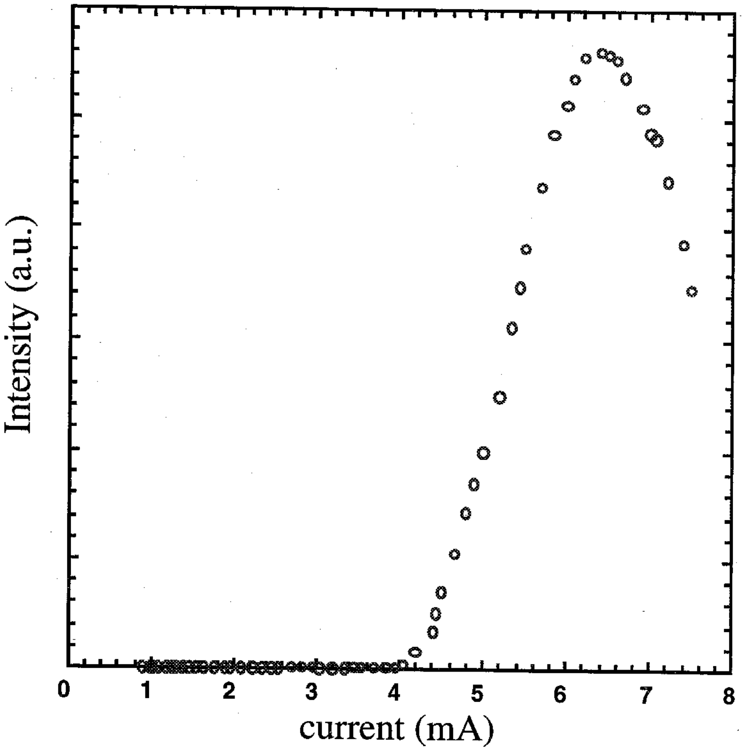

Figure 5.17 A typical L-I pulsed L-I characteristic obtained from an 18 µm diameter laser showing the rollover in output power due to the operating temperature decreasing the spectral overlap between the resonance and the gain peak.

5.5.2 Laser Spectra and Transverse Modes

Control over lasing modes of VCSELs will be important if they are to be used in high speed long distance communications. A single stable fundamental mode is desirable in most applications. Typically the VCSELs produced so far are multimode and change modes depending on the bias point [2,15]. Figure 5.18 shows the same laser with two different electrical pump pulse widths. Single mode devices can be obtained by fabricating very small lasers in which the guiding structure only supports the fundamental mode, but these devices are small and have low output powers. There are also reports of the use of impurity induced disordering to control the transverse mode [16], designing the opening in the top metal contact to spatially filter out a preferred mode [17], and the use of antiguiding to select a preferred mode [18].

Another problem is that since the transverse modes have orthogonal polarizations that are spectrally degenerate, the operating polarization is not stable. This polarization can be controlled by fabricating structures that are not symmetric so that the degeneracy is broken [19,20]. In addition, polarization control has been obtained by anisotropic thermal stress [21] and by depositing a high index of refraction material on one side of the dielectric mirror walls [22]. In these devices the two polarizations then have slightly different threshold gains, and the polarization is stable because only one of the modes reaches threshold. The hybrid VCSELs fabricated for this thesis are generally multimoded above threshold. One sample displayed single mode linearly polarized behavior up to $5xI_{th}$ but this was not seen on other samples.

The typical full width at half-maximum (FWHM) of the lasing peak is about 1 Å. The spectra were taken by fiber-coupling the laser to a scanning monochromator. The output was detected by a photomultiplier tube cooled to about -20 °C. The data was read into a computer from a lock-in amplifier using LabView. The LabView program was

(a)

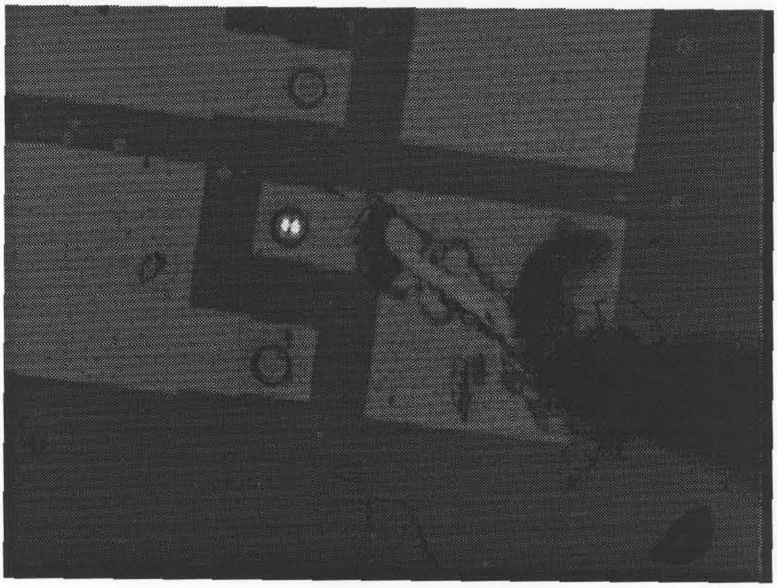

(b)

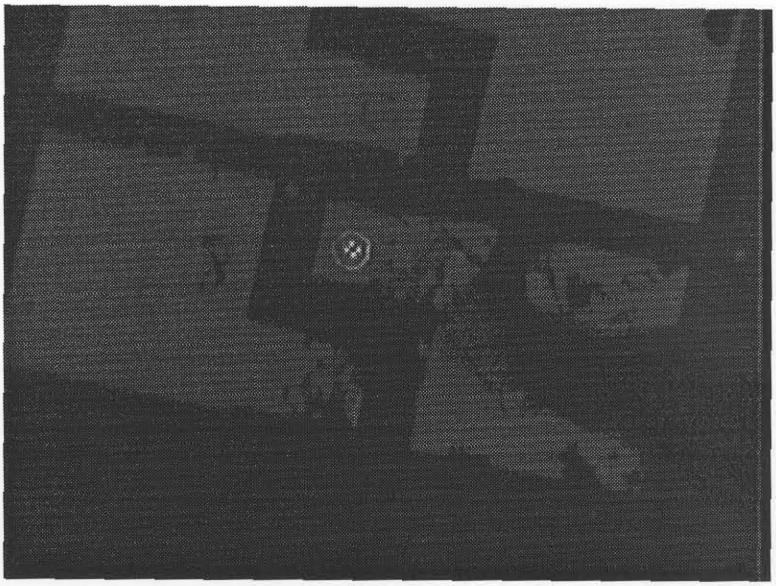

Figure 5.18. Images illustrating mode changes with duty cycle. The pulse width in (a) is 20 nsec, and in (b) it is 100 nsec. The repetition rate is 29 kHz in both cases.

written by Andrew Tong as part of a SURF project. Figure 5.19 displays the spectra of a multimode device showing the transition from single mode to multimode operation. This was taken from a 12 μm diameter laser.

The near-field images of the modes show transverse modes closely resembling the Hermite-Gaussian modes. The resonant cavity for these structures has step-index guiding for about 0.9 μm of the four wavelength optical cavity. The cladding material, SiO_2, results in a step in the index of refraction from about 3.6 in the core of the laser to about 1.5 in the SiO_2. Figure 5.20 shows the collection of modes found in these hybrid VCSELs. These images were taken with a Si CCD camera through a microscope. The smallest lasers, 6 μm diameter, always lased in the fundamental mode. The next two larger sizes, 12 μm and 18 μm diameter, tended to operate in a double-lobed mode. The largest devices operated in the higher order modes shown in figure 5.20. Figure 5.21 shows three spectra taken below threshold from three different size devices. The mode that reached threshold is marked with an arrow and a near field image above threshold of the mode is also shown. As expected, the mode spacing is smaller in the larger devices.

The lasing wavelength varied across the samples. This was a result of both variations in the epitaxially grown layers as well as thickness variations in the sputtered top mirrors. One wafer produced lasers with wavelengths varying between 978 and 1005 nm. A piece of this wafer had lasing wavelengths that varied from 995 nm to 1005 nm within 3 mm of each other. The lasing spectra for three adjacent devices is shown in figure 5.22.

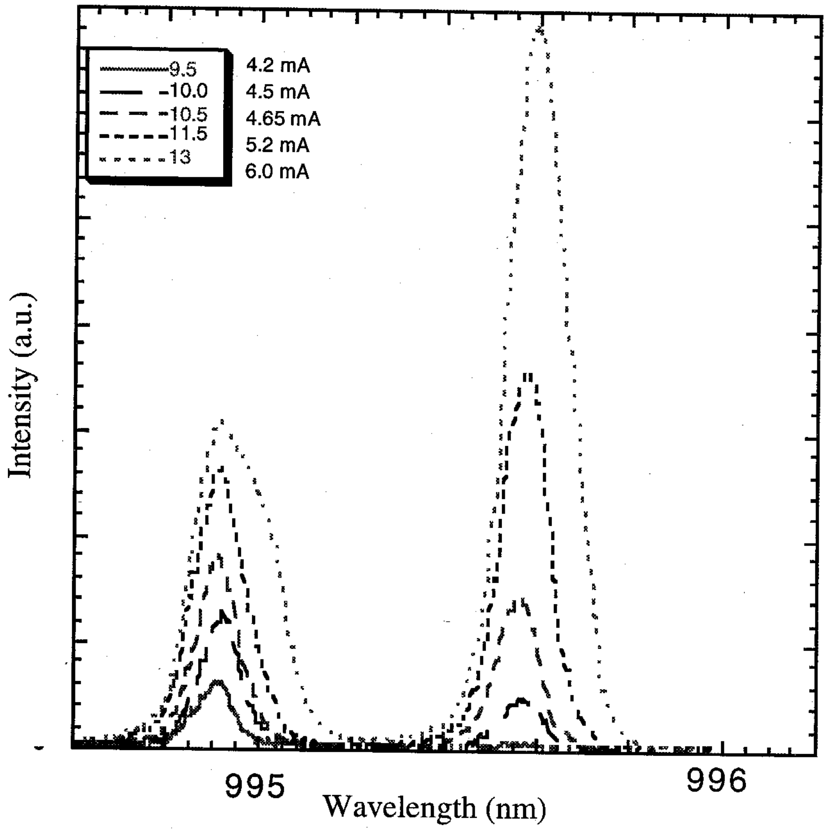

Figure 5.19 Lasing spectrum showing the transition from single transverse mode operation to two transverse lasing modes.

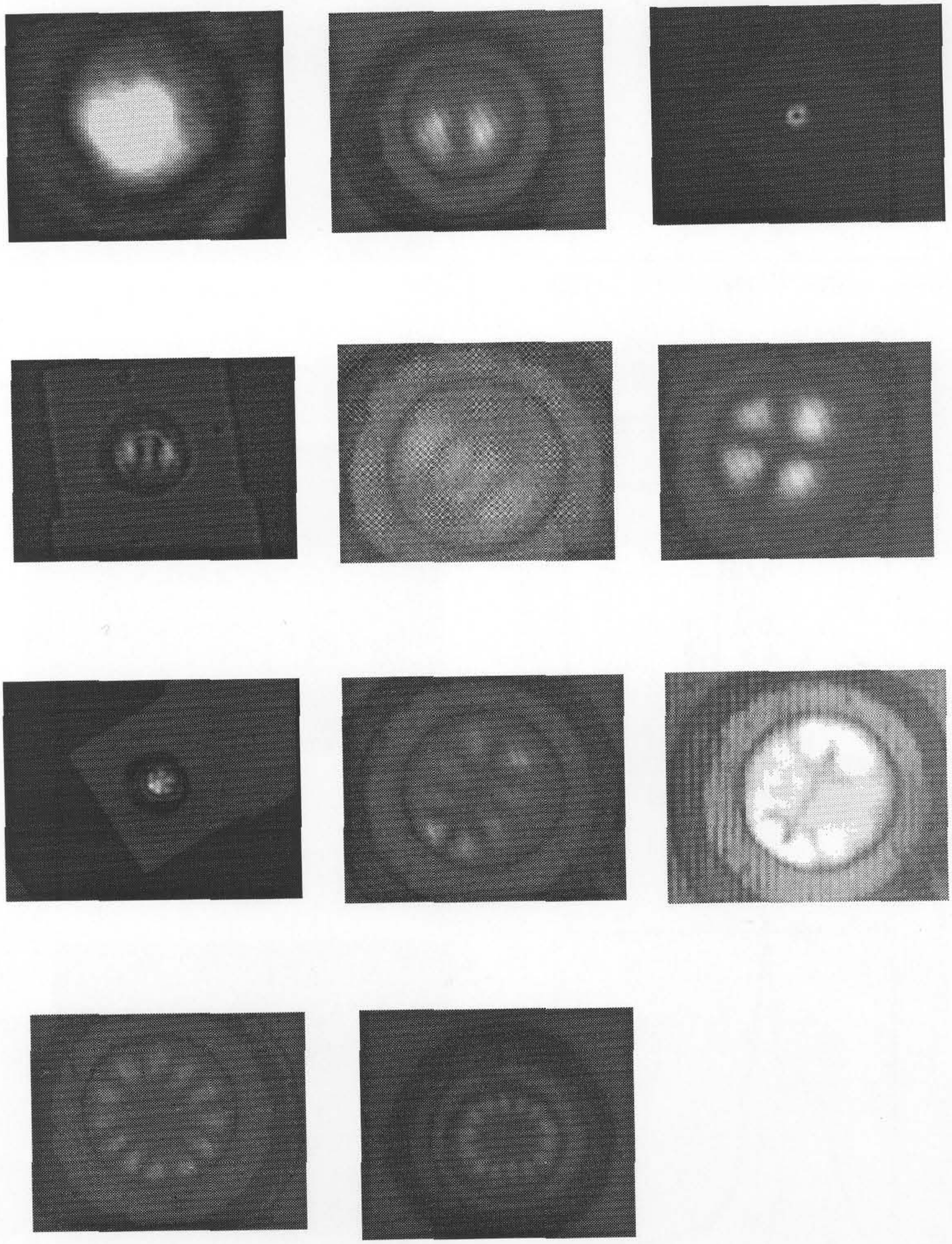

Figure 5.20. Near field images showing the variety of modes observed in the hybrid VCSEL structure.

6 µm diameter

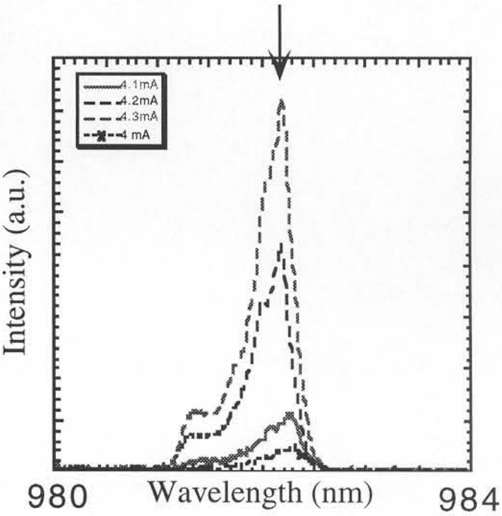

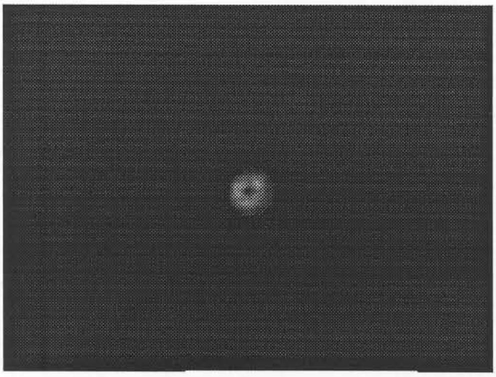

12 µm diameter

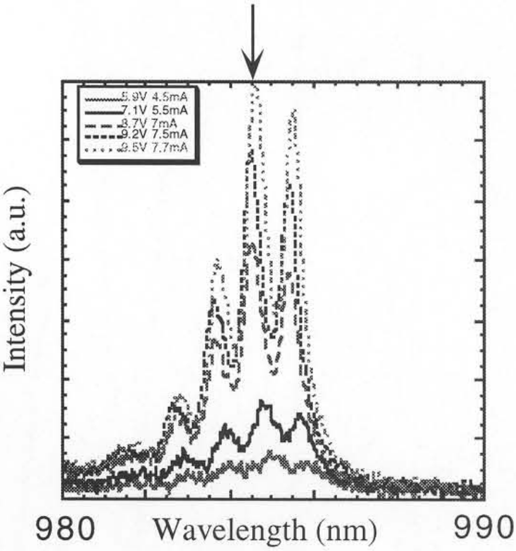

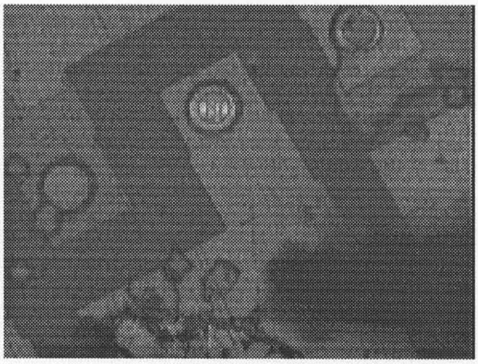

30 µm diameter

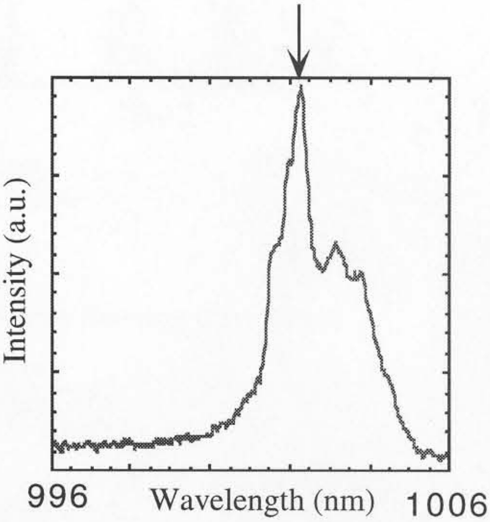

Figure 5.21. On the right side are shown optical spectra of three different size lasers below threshold. On the left the near field image above threshold. This mode is marked on the right with an arrow.

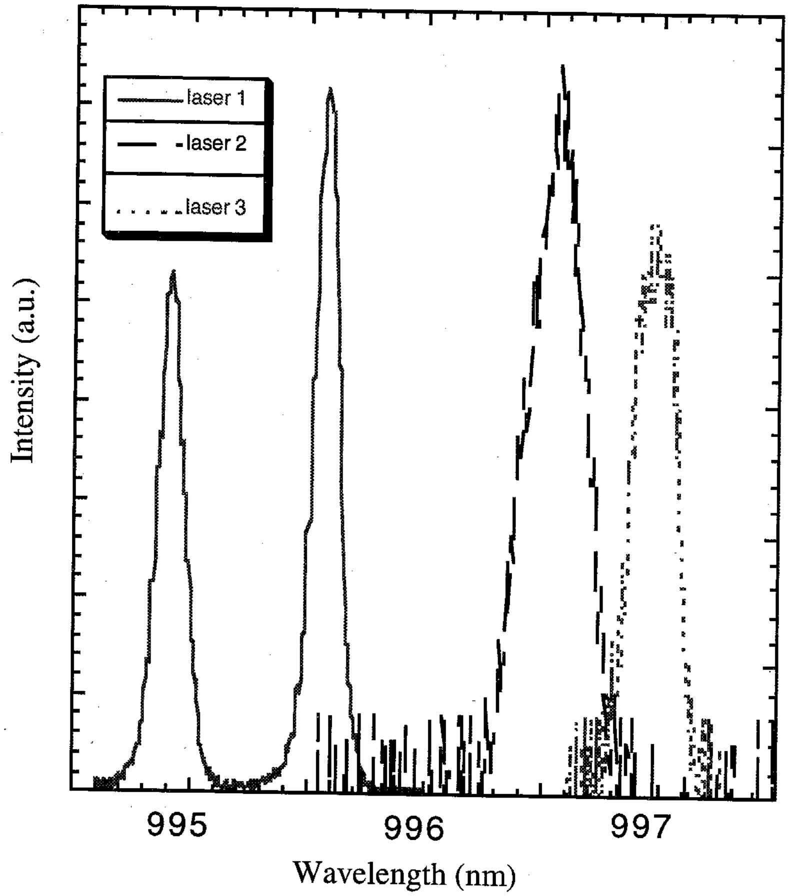

Figure 5.22. Lasing spectra from three adjacent devices showing wavelength variations.

5.6 Conclusions

Hybrid semiconductor/dielectric VCSELs with InGaAs quantum wells have been demonstrated. These lasers had a minimum threshold current in a 6 μm diameter device of 2.5 mA and a slightly larger device had a threshold voltage of 1.8 V. The peak output power measured from these lasers was 1.67 mW. The lasers exhibited strongly index-guided multi-mode spectra. Also, the hybrid structure was used to characterize the carrier distribution in the active region as well as the temperature of the active devices.

References

[1] A. Scherer, M. Walther, J. P. Harbison, L. T. Florez, *Elect. Lett*, **28**, 1224 (1992)

[2] D. L. Huffaker, D. G. Deppe, T. J. Rogers, *Appl. Phys. Lett.*, **65**, 1611 (1995)

[3] W. B. Joyce, S. H. Wemple, *J. Appl. Phys.*, **41**, 3818 (1970)

[4] N. K. Dutta, *J. Appl. Phys.,* **68**, 1961 (1990)

[5] J. O'Brien, R. Lee, G. Almogy, W. H. Xu, A. Scherer, A. Yariv, in preparation

[6] R. Michalzik, K. J. Ebeling, *IEEE J. Quant. Elect.*, **29**, 1963 (1993)

[7] W. Nakwaski, M. Osinski, *IEEE J. Quant. Elect.*, **27**, 1391 (1991)

[8] W. Nakwaski, M. Osinski, *IEEE J. Quant. Elect.*, **29**, 1981 (1993)

[9] D. Vakhshoori, J. D. Wynn, G. J. Zydzik, R. E. Leibenguth, M. T. Asom, K. Kojima, R. A. Morgan, *Appl. Phys. Lett.*, **62**, 1448 (1993)

[10] J. W. Scott, R. S. Geels, S. W. Corzine, L. A. Coldren, *IEEE J. Quant. Elect.*, **29**, 1295 (1993)

[11] R. A. Morgan, L. M. F. Chirovsky, M. W. Focht, G. Guth, M. T. Asom, R. E. Leibenguth, K. C. Robinson, Y. H. Lee, J. L. Jewell, *Proc. SPIE,* **1562**, 149 (1991)

[12] B. Tell, K. Brown-Goebeler, R. E. Leibenguth, F. M. Baez, Y. H. Lee, *Appl. Phys. Lett.*, **60,** 683 (1992)

[13] D. B. Young, J. W. Scott, F. H. Peters, M. G. Peters, M. L. Majewski, B. J. Thibeault, S. W. Corzine, L. A. Coldren, *IEEE J. Quant. Elect.*, **29**, 2977 (1993)

[14] R. S. Geels, B. J. Thibeault, S. W. Corzine, J. W. Scott, L. A. Coldren, *IEEE J. Quant. Elect.*, **29**, 2977 (1993)

[15] C. J. Chang-Hasnain, J. P. Harbison, G. Hasnain, A. C. Von Lehmen, L. T. Florez, N. G. Stoffel, *IEEE J. Quant. Elect.*, **27**, 1402 (1991)

[16] T. G. Dziura, Y. J. Young, R. Fernandez, S. C. Wang, *Elect. Lett.*, **29**, 1236 (1993)

[17] R. A. Morgan, G. D. Guth, M. W. Focht, M. T. Asom, K. Kojima, L. E. Rogers, S. E. Callis, *IEEE Photon. Tech. Lett.*, **4**, 374 (1993)

[18] Y. A. Wu, C. J. Chang-Hasnain, R. Nabiev, *Elect. Lett.*, **29**, 1861 (1993)

[19] K. D. Choquette, R. E. Leibenguth, *IEEE Photon. Tech. Lett.*, **6**, 40 (1994)

[20] T. Yoshikawa, H. Kosaka, K. Kurihara, M. Kajito, Y. Sugimoto, K. Kasahara, *Appl. Phys. Lett.*, **66**, 908 (1995)

[21] T. Mukaihara, F. Koyama, K. Iga, *IEEE Photon. Tech. Lett.*, **5**, 133 (1993)

[22] M. Shimuzi, T. Mukaihara, F. Koyama, K. Iga, *Elect. Lett.*, **27**, 1067 (1991)

Chapter 6

Vertical Cavity Lasers Emitting at 850 nm

6.1 Introduction

This chapter will discuss the work done on monolithic semiconductor VCSELs with GaAs quantum wells in the active region. These lasers are gain-guided with a proton implantation to define the current path and designed to be top-emitting at 850 nm. They exhibit much higher series resistance than the hybrid structure lasers because of the inclusion of the p-doped mirror in the current path. The entire structure was epitaxially grown by MBE. The large amount of AlGaAs in the design compared to the hybrid structure means that the growth temperatures required to achieve precise layer thicknesses resulted in a more serious compromise in the optical quality of the material. The chapter will begin with sections describing the laser structure and the fabrication procedure. This will be followed by a section describing the electrical and optical characteristics of these lasers.

6.2 The VCSEL Structure

This structure is similar to that published in references [1] and [2]. It consists of Bragg mirrors of AlAs and $Al_{0.13}Ga_{0.87}As$ layers for the n-doped mirror and $AlAs/Al_{0.37}Ga_{0.63}/Al_{0.13}Ga_{0.87}As/Al_{0.37}Ga_{0.63}As$ layers for the p-doped mirror. The extra layers of the p-doped mirror were added to reduce the series resistance. These alloy concentrations were obtained using two aluminum cells. The cell temperatures were not changed during the growth of the distributed Bragg mirrors. This scheme had been shown to reduce the resistance of these mirrors compared to simple two-layer Bragg reflectors [3].

Two different structures were grown. One had 26 1/2 bottom mirror pairs and 20 top mirror pairs. The other structure had 28 1/2 and 22 mirror pairs. The structure with 26 1/2 and 20 mirror pairs had a two wavelength long optical cavity. The active region had four 100 Å GaAs quantum wells centered around the peak of the standing wave optical field. The quantum wells were separated by 75 Å of $Al_{0.37}Ga_{0.63}As$ which also formed the spacer layers between the mirrors and the quantum wells. The optical cavity was doped $1x10^{18}$ cm^{-3} for 1/3 of the carrier confinement layer next to the mirrors on each side of the junction. The region around the quantum wells was undoped in order to reduce free carrier absorption losses. The doping in the mirrors was $3x10^{18}$ cm^{-3} for the n-doped mirror and the five p-doped mirror pairs nearest to the optical cavity. The next 13 mirror pairs of the p-mirror were doped $5x10^{18}$ cm^{-3} and the top two pairs were doped $1x10^{19}$ cm^{-3}. The doping levels were increased in the top mirror in an effort to reduce the series resistance and the contact resistance. The Fabry-Perot resonance for this structure was measured to be at 830 nm instead of the designed 850 nm. An SEM cross section of this wafer is shown in figure 6.1.

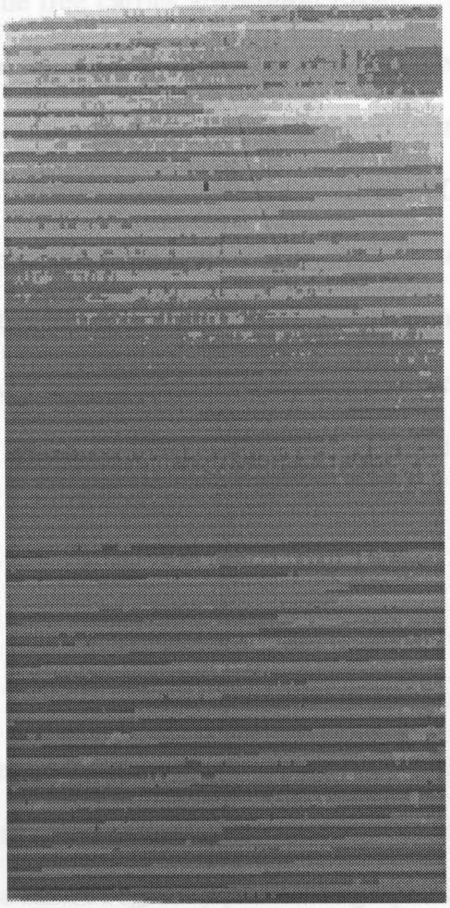

Figure 6.1. An SEM micrograph of a VCSEL wafer showing the optical cavity and part of the mirror layers.

The structure that was grown with 28 1/2 and 22 mirror pairs had a one wavelength long optical cavity. The doping in the cavity was lowered to $5x10^{17}$ cm^{-3} for the n and p sides to further reduce the free carrier absorption losses. The doping levels in the mirrors were the same as for the previous sample. The optical cavity of this structure was grown at a substrate temperature of around 700 °C in an effort to improve the optical quality of the material, while the rest of the structure was grown at 600 °C. This resulted in an even larger difference between the measured Fabry-Perot resonance and the designed value because the amount of Ga incorporation is very sensitive to the substrate temperature in this range and exact reproducibility of the substrate temperature is difficult. The VCSEL wafers with the optical cavity grown at 700 °C did, however, have lower thresholds than those grown at 600 °C.

6.3 Fabrication

These lasers are top-emitting gain-guided structures with the current path defined through proton implantation. Figure 6.2 shows a schematic cross section of the device. The fabrication of these lasers began by photolithographically defining 10 and 30 μm photoresist dots on the sample. These dots serve to mask the ion implantation and are used to lift-off the metal contact for top emission. Then a AuZn/Au top contact was evaporated on the entire sample and a AuGe/Au bottom contact was deposited. Next, 100 μm square photoresist pads were put down over the region where there were photoresist dots. Then the exposed metal contact was chemically etched away. Following this, an isolation etch was done using an 8:1:40 solution of H_2SO_4, H_2O_2, and water, and then the sample was proton implanted to define the current path. Finally, the metal dots were lifted off the sample and the sample was annealed. The annealing was done at 450 °C for 30 seconds to reduce the series resistance. The fabrication procedure is shown in figure 6.3.

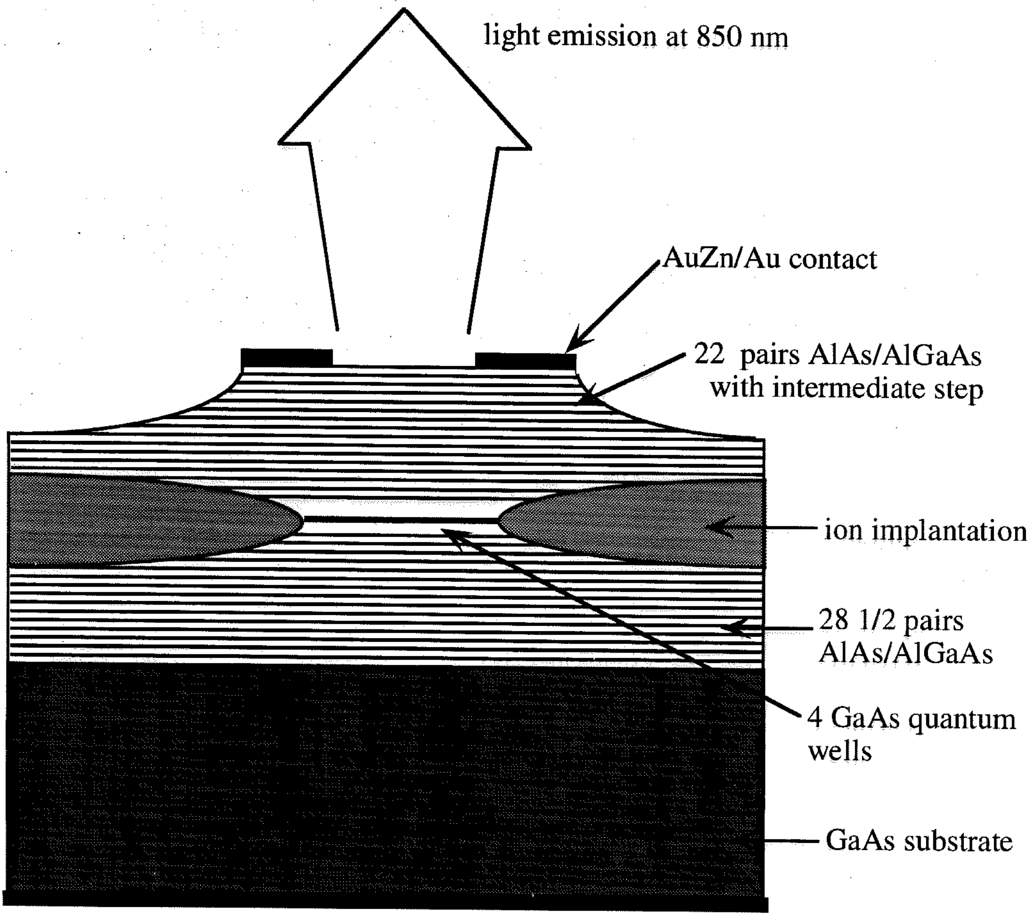

Figure 6.2. A schematic cross section of the top-emitting gain guided VCSEL with GaAs quantum wells in the active region.

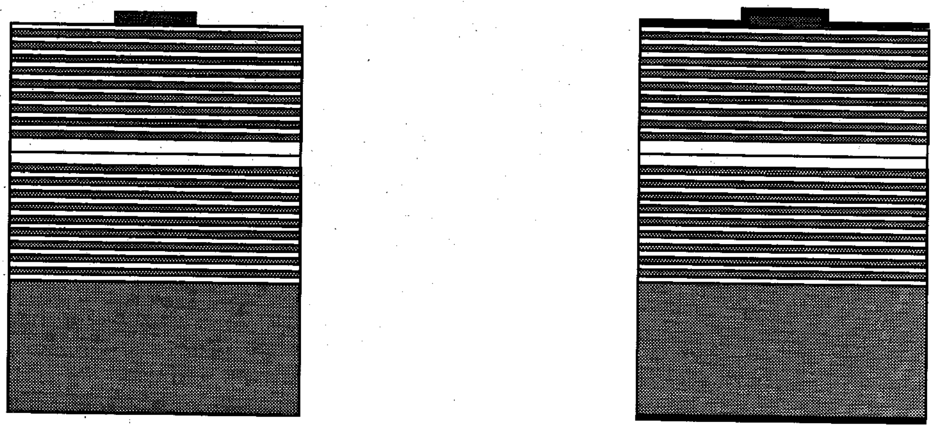

deposit photoresist dots

evaporate metal contacts

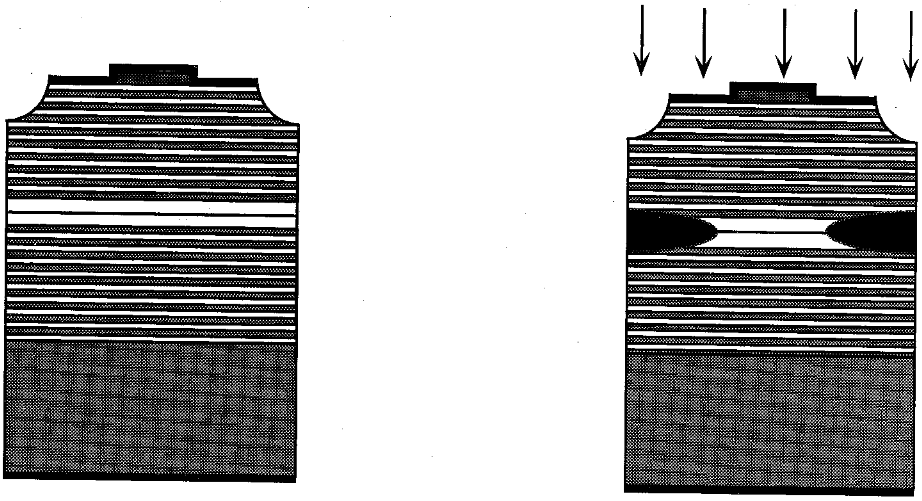

etch Au and isolate devices

proton implantation

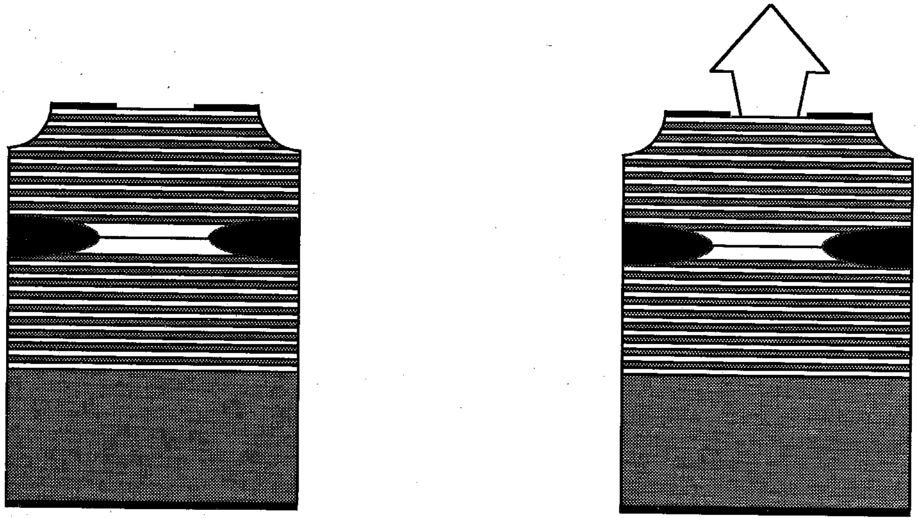

lift-off photoresist

Figure 6.3 A schematic representation of the fabrication sequence for the gain guided VCSELs.

6.4 Device Performance

These structures have a very large series resistance, as can be seen from the I-V curve in figure 6.4. The threshold voltage for a 30 µm diameter laser with an 11 mA threshold current was 39V. This was the lowest threshold current measured. As a result of this, the devices only operated in a pulsed mode with very short, ≤ 50 nsec, pulses. Figure 6.5 shows an image of a 30 µm diameter device lasing. The smaller lasers did not have lower threshold currents. This is attributed to the mismatch between the operating wavelength and the designed wavelength. The lasers with the lowest threshold current operated around 815 nm. Edge-emitting lasers grown around the same time under similar growth conditions operated near 850 nm, so the gain peak of the VCSELs was probably at a wavelength which was 35 nm to the red of the Fabry-Perot mode. This spectral misalignment becomes worse as the temperature increases because the gain shifts to longer wavelengths faster than the Fabry-Perot mode. The small, 10 µm diameter, lasers have the largest series resistance and so are expected to operate at the highest temperatures. This will produce a large spectral difference between the gain peak and the resonant wavelength resulting in high threshold currents.

These devices did produce a higher peak output power than the hybrid structures, however. The highest peak output power measured was 2 mW at a bias of 16 mA. This was obtained from a 30 µm diameter laser operating with 50 nsec pulses at a repetition rate of 30 kHz. Figure 6.6 shows the L-I characteristic of this laser.

These lasers did not exhibit the clear transverse mode structure that the hybrid cavity lasers did. This was expected because the lasers are gain guided. Studies have been done showing clear transverse modes of gain guided VCSELs [4-7], but these devices were relatively small. The smaller, 10 µm diameter, devices fabricated for this work operated in a fundamental mode. A few of the 30 µm diameter lasers operated in the next higher order double-lobed mode, but most of the larger devices showed filamentary lasing.

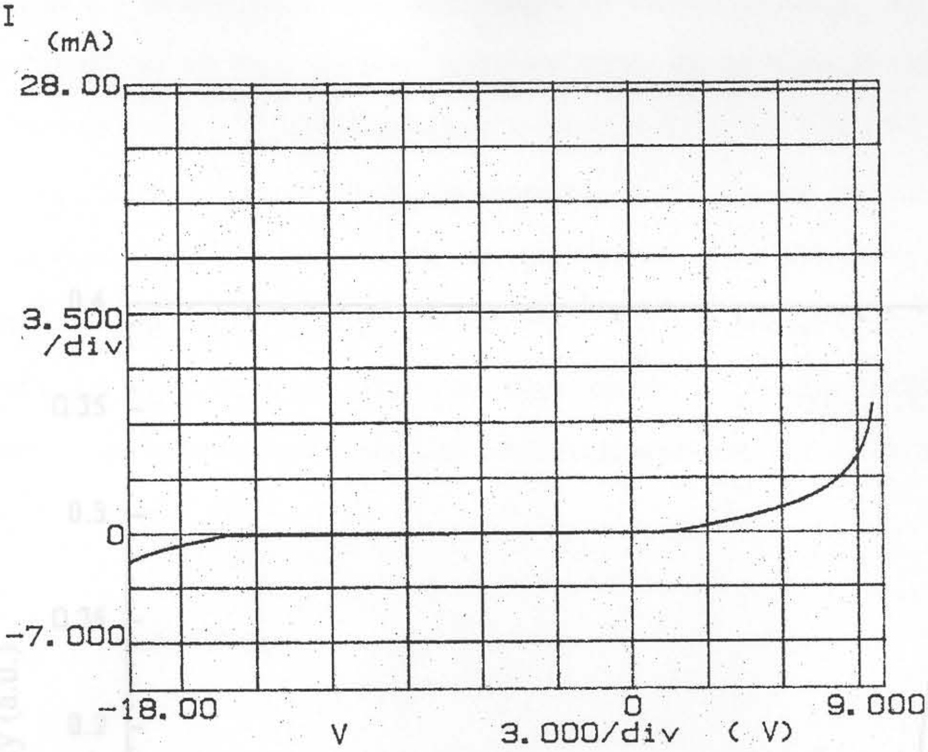

Figure 6.4. An I-V characteristic of a 30 μm diameter device.

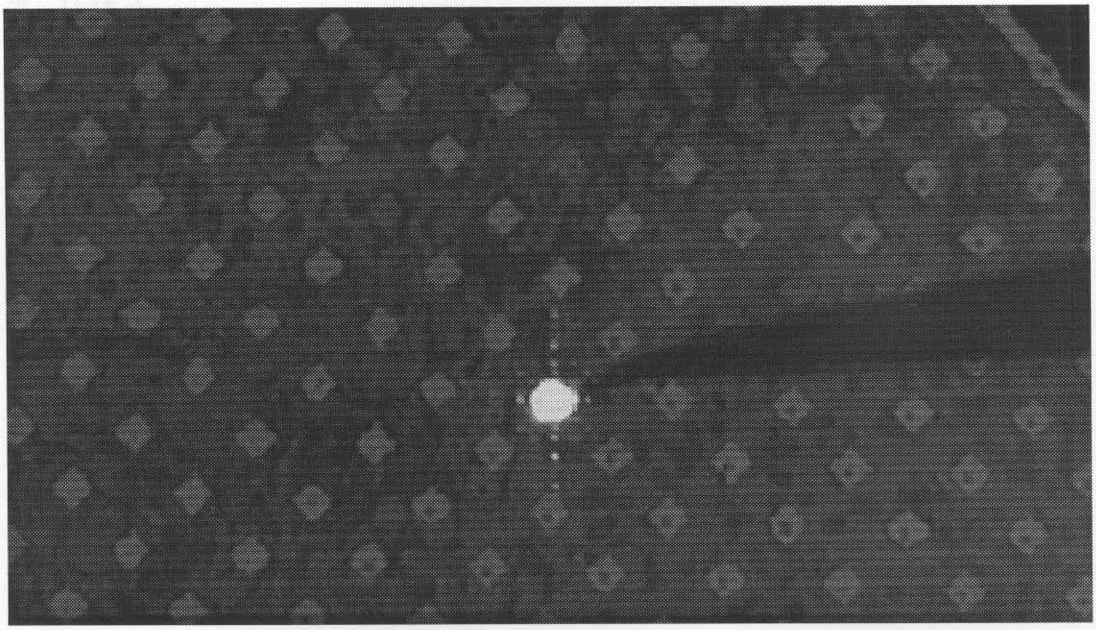

Figure 6.5. A CCD picture taken through a microscope showing a 30 μm diameter laser operating. The 10 μm diameter devices are in the top left region of the photograph, and the bottom right portion contains 30 μm diameter devices.

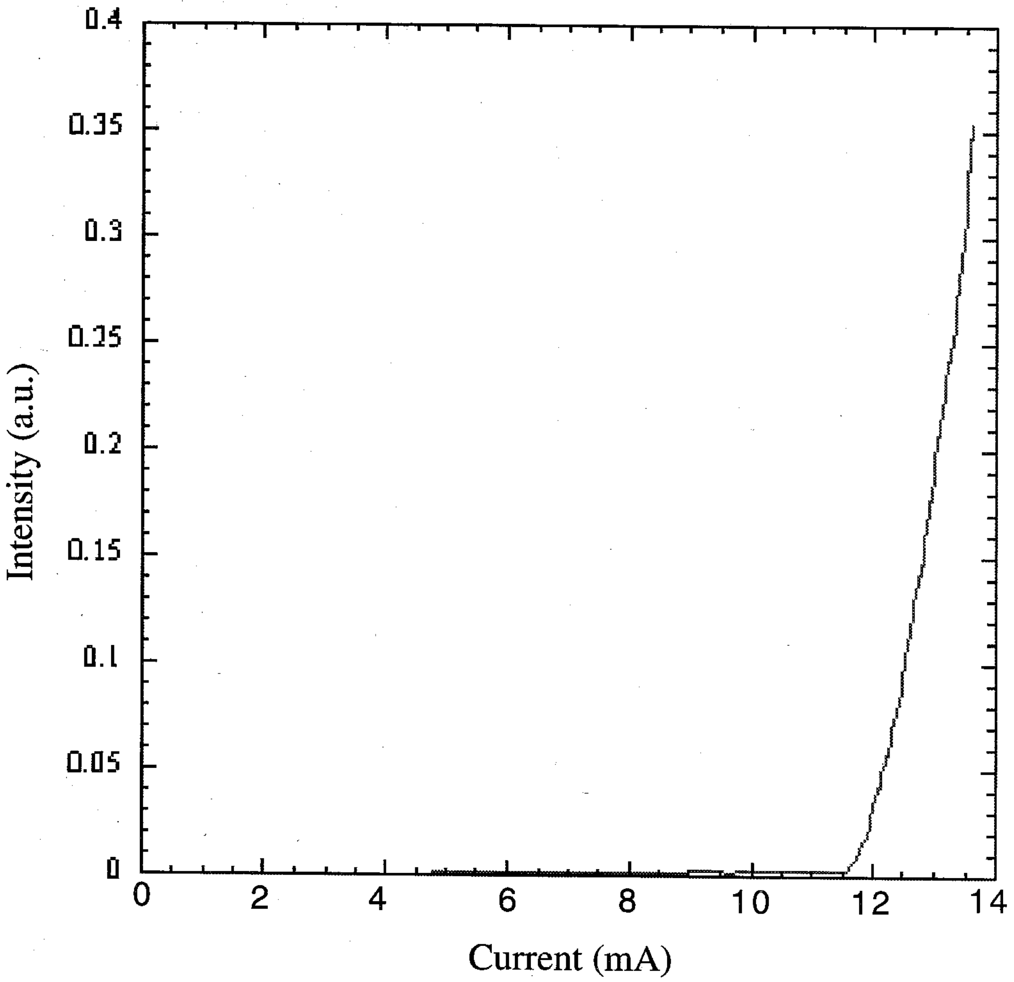

Figure 6.6. A pulsed L-I characteristic of a 30 μm diameter laser. The peak laser power was 2 mW obtained at 16 mA.

Figure 6.7 shows several near field images for various VCSELs. All of these devices except the one shown in the lower right-hand corner are the larger 30 μm diameter lasers. The spectrum of a 30 μm diameter laser is shown in figure 6.8. The FWHM of the spectra of these lasers was about 1.5 Å, just above threshold. The top spectrum in figure 6.8 is just above threshold and the bottom spectrum shows higher currents as well. The lasing peak shifts to longer wavelengths as the current increased and the operating temperature of the active region increases. As was mentioned earlier, this sample was far off the designed wavelength value because of the high substrate temperature used during the growth of the active region.

6.5 Conclusions

VCSELs with GaAs quantum wells were demonstrated. These lasers had a very high series resistance compared to the hybrid structures discussed in chapter 5. As a result only pulsed operation was possible for these lasers. The GaAs quantum wells also required the use of ternary AlGaAs layers in the Bragg reflectors, and the AlGaAs material quality was compromised in order to obtain the necessary control over the growth rates. These lasers produced 2 mW peak output power and threshold currents of around 11 mA for 30 μm diameter devices. Also, no clear transverse mode structure was observed for the large devices.

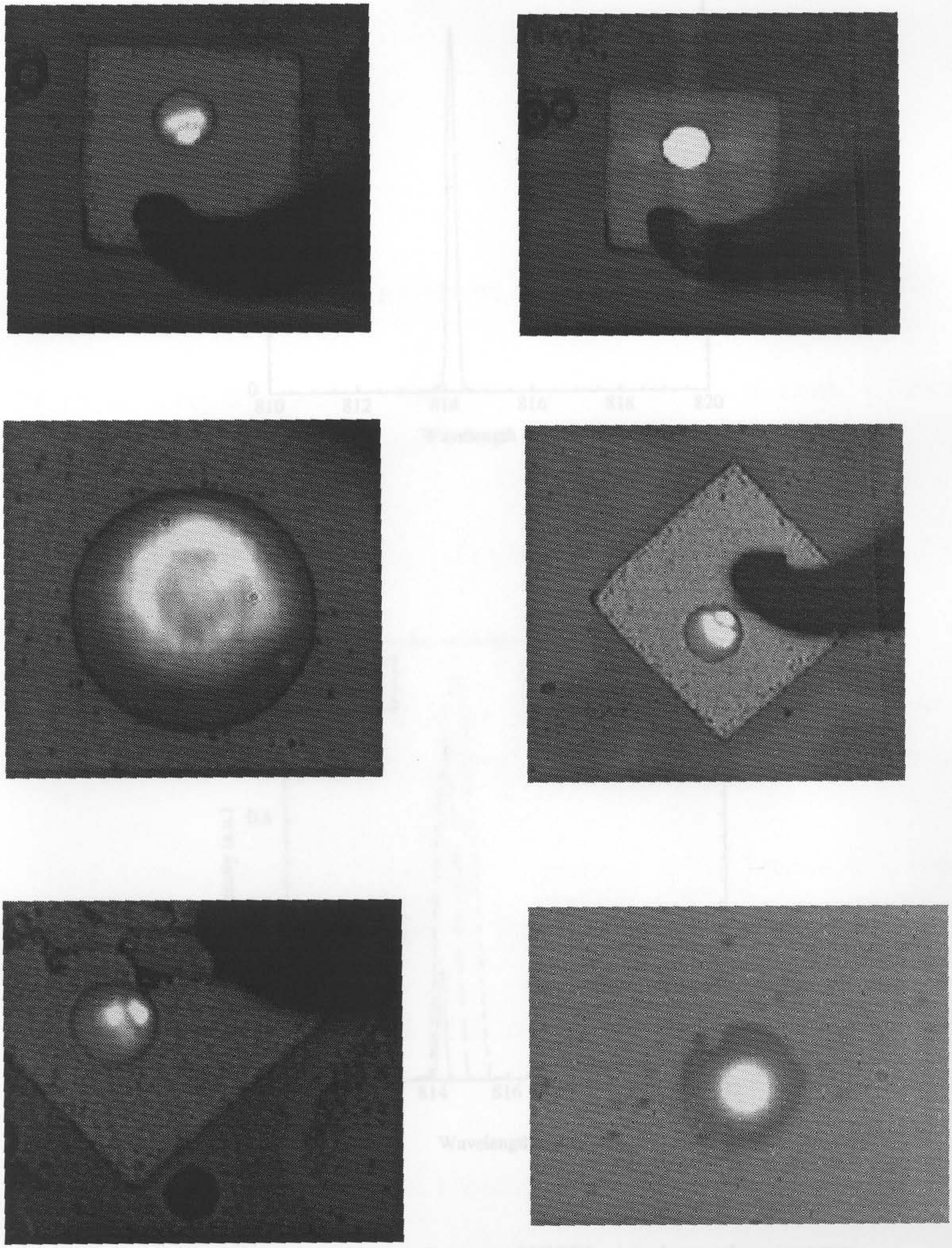

Figure 6.7. Near field images of the gain-guided VCSELs. The device in the bottom right is 10 μm in diameter, the rest are 30 μm in diameter.

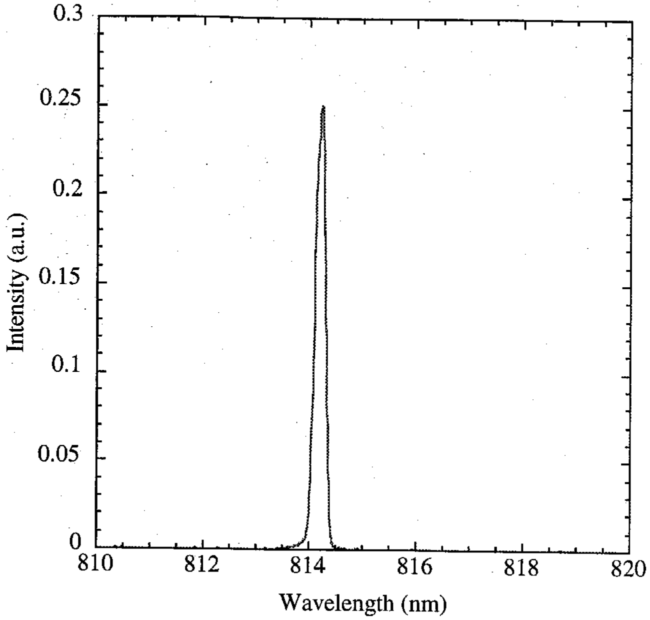

(a)

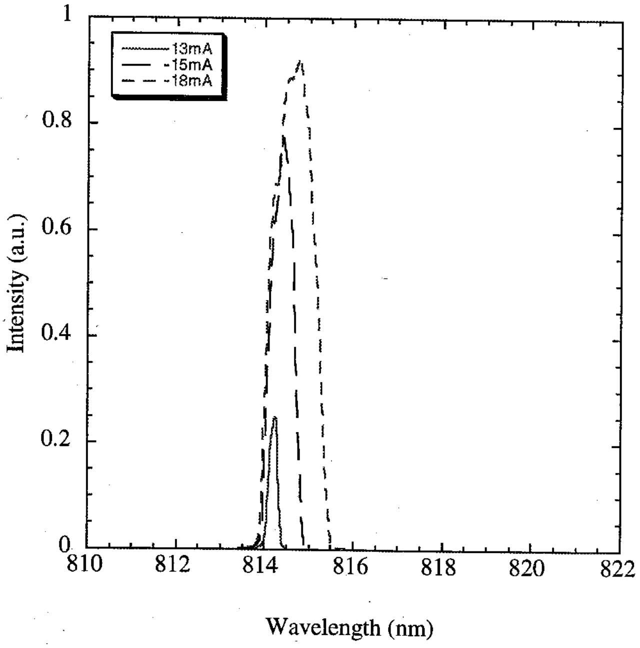

(b)

Figure 6.8. Spectra from a 30 μm diameter VCSEL. (a) shows the spectrum just above threshold, and (b) shows several other currents as well.

References

[1] Y. H. Lee, B. Tell, K. Brown-Goebeler, J. L. Jewell, *Elect. Lett.*, **26**, 711 (1990)

[2] Y. H. Wang, G. Hasnain, K. Tai, J. D. Wynn, B. E. Weir, N. K. Dutta, A. Cho, *J. Vac. Sci. Technol.*, **B10**, 1002 (1992)

[3] K. Tai, L. Yang, Y. H. Wang, J. D. Wynn, A. Y. Cho, *Appl. Phys. Lett.*, **56**, 2496 (1990)

[4] C. J. Chang-Hasnain, M. Orenstein, A. Von Lehmen, L. T. Florez, J. P. Harbison, N. G. Stoffel, *Appl. Phys. Lett.*, **57**, 218 (1990)

[5] C. J. Chang-Hasnain, J. P. Harbison, G. Hasnain, A. C. Von Lehmen, L. T. Florez, N. G. Stoffel, *IEEE J. Quant. Elect.*, **27**, 1402 (1991)

[6] R. A. Morgan, G. D. Guth, M. W. Focht, M. T. Asom, K. Kojima, L. E. Roberts, S. E. Callis, *IEEE Photon. Tech. Lett.*, **4**, 374 (1993)

[7] D. Vakhshoori, J. D. Wynn, G. J. Zydzik, R. E. Leibenguth, M. T. Asom, K. Kojima, R. A. Morgan, *Appl. Phys. Lett.*, **62**, 1448 (1993)